The Synthesis and Characterization of Thin Film Copper Zinc Tin Sulfide for Solar Cell Applications

A Dissertation
SUBMITTED TO THE FACULTY OF
UNIVERSITY OF MINNESOTA
BY

Melissa C. Johnson

IN PARTIAL FULFILLMENT OF THE REQUIREMENTS
FOR THE DEGREE OF
DOCTOR OF PHILOSOPHY

Prof. Eray S. Aydil, Advisor

November, 2014

Acknowledgements

I am deeply indebted to a large number of people, all of whom in their own way made the completion of this possible. First and foremost, I am very grateful for the advisement I've received, not only from Eray Aydil, but from Chris Leighton, Steve Campbell, and Michael Manno as well. The weekly meetings and hands on guidance in the lab were an invaluable source of learning. I started graduate school strictly as a chemical engineer, and due to a tremendous amount of patience and teaching from the aforementioned people, I have emerged much more of a material scientist.

I am also extremely thankful for the Aydil and Leighton group members, both present and past, who have helped me with my work. In particular, I would like to acknowledge, Boris Chernomordik, Elijah Thimsen, Xin Zhang, and Selin Tosun, all of whom were invaluable to me both working in the lab and in discussions outside the lab. I would also be remiss to leave out Neema Rastgar, Brian Merritt, Jonathan (Cloud) Hubbard, Nancy Trejo, Elliot Combs, Bryce Williams and Ankur Khare, all of whom have made the last five years in the office and lab immensely enjoyable. I also owe a great deal to the undergraduates who aided my work, no matter how menial or repetitive, including Cody Wrasman, Matthew Quan, and Dana Dement.

Finally, words simply cannot express how thankful I am to my friends and family that have been with me for the last five years (and more). I would not have been able to achieve this without the constant support and guidance from my parents; this belongs as much to them as it does to me. And to my husband Phil, who for better or worse went through nearly every high and low in graduate school by my side, you are the light in my life. Words cannot express how much you have meant through all of this; all I can say is thank you for absolutely everything.

Dedication

To my friends and family.

Abstract

Copper zinc tin sulfide (Cu_2ZnSnS_4 or CZTS) is a promising candidate as a sunlight absorbing layer in thin film solar cells. This emerging material has a band gap of 1.45 eV, ideal for the solar spectrum, and absorbs sunlight efficiently, making it a potentially viable replacement for CdTe and $CuIn_{1-x}GaxSe_2$ in thin film solar cells. Unlike the commercially available thin film solar cells, comprised of CdTe or $CuIn_{1-x}Ga_xSe_2$, CZTS is comprised of earth abundant and non-toxic elements. Power conversion efficiencies in CZTS based solar cells have risen quickly. However, there is still a need to develop low-cost and scalable synthesis methods. Furthermore, the rapid rise in CZTS solar cell efficiencies is largely due to a trial-and-error approach to assembling devices, which has relied heavily on utilizing existing geometries for $CuIn_{1-x}Ga_xSe_2$ solar cell devices. This has led to a knowledge gap in the fundamental material properties of CZTS, which this thesis aimed to help close.

We first worked to address the need for a low cost synthesis method by adapting a process already used to make $CuIn_{1-x}Ga_xSe_2$ on an industrial scale, *ex situ* sulfidation of Cu-Zn-Sn thin metal alloy films. In this approach the metal alloy films are exposed to sulfur vapor at elevated temperatures to form CZTS. Specifically, Cu-Zn-Sn thin films were co-sputtered onto suitable substrates and then loaded into an evacuated quartz ampoule with a known weight of sulfur (1-100 mg). This ampoule was subsequently heated to a desired predetermined sulfidation temperature, typically for 8 hours, and then cooled back to room temperature. We investigated the effects of both sulfidation temperature and the substrate. We found that at 600 ^oC, regardless of the substrate, phase-pure CZTS films were obtained from precursor films with compositions close to the stoichiometric ratio of Cu, Zn and Sn. Interestingly, we found that if a substrate contains group I metals, such as Na and K, common impurities in soda lime glass (SLG) substrates, phase-purity was achieved at temperatures below 600 ^oC. Furthermore, films grown on SLG exhibited much larger grain sizes than films grown on any other substrate.

We investigated strategies to tune the stoichiometry of CZTS films through *ex situ* sulfidation, an important consideration as films that are nominally Cu poor and Zn rich perform better in solar cell devices. We found that within a closed system, like our quartz ampoule, the Sn content was self regulating such that the Cu-to-Sn ratio always approached two. The mechanism to achieve this end composition was facilitated by volatile SnS. In Sn rich films SnS evaporation reduced the Sn content while in Sn poor films SnS from the vapor phase could react and incorporate into the film through reaction with $Cu_{2-x}S$, an intermediate phase. Thus, Sn deficiency in precursor films can be corrected by including ~ 1 mg of elemental Sn in the sulfidation ampoule, which generates SnS vapor above the film. This facile removal and addition of Sn from the film allows significant tolerance for Sn concentration in the precursor films. The Cu-to-Zn ratio was controlled by changing the sputtering rates of Cu and Zn containing targets used in the co-sputtering.

We found that impurities, such as Na and K, from the SLG substrates are volatilized under the aggressive sulfidation process and can be incorporated into the CZTS films through the vapor phase. The presence of these impurities leads to a significant increase in the grain size in CZTS films. TOF-SIMS depth profiling of CZTS films demonstrated that Na, K, and Ca from SLG can be incorporated into the CZTS films either by diffusion from the substrate or by vapor transport of volatile species. Based on this finding, we developed a method to introduce Na, K and Ca into the CZTS films through the vapor phase by coating the sulfidation ampoule with NaOH, KOH or $Ca(OH)_2$. These coatings volatilize during sulfidation and incorporate Na, K or Ca into the CZTS. We found that Na and K were responsible for the enhanced grain growth realized with SLG, and that this hydroxide coating method allowed us to tune the grain size in the films by varying the amount of NaOH or KOH coated onto the ampoule wall. We also found that grain sizes in CZTS films increased with increasing S pressure.

Finally, we investigated the effect of the Cu-to-Zn ratio, grain size and Na incorporation on the electronic properties of CZTS films. We found that all CZTS films were *p*-type and that decreasing the Cu-to-Zn ratio decreases the hole concentrations.

Films that were Cu-rich and Zn-poor exhibited very high hole concentrations (10^{20} cm^{-3}), but the hole concentrations decreased dramatically as the Cu-to-Zn ratio was reduced. We found that increasing the grain size, without the addition of an impurity such as Na or K, leads to higher hole mobilities and lower hole concentrations in Cu-poor and Zn-rich films. The addition of Na dramatically increases hole concentrations particularly in films that were were stoichiometric or Cu-poor and Zn-rich to. in contrast, the resistivities and carrier concentrations in Cu-rich films remain essentially unchanged regardless of the grain size or whether Na was present in the films. Temperature dependent resistivity measurements show that all films exhibit semiconducting behavior, even when they are Cu-rich and Zn-poor and the carrier concentrations exceed the critical carrier concentration for a metal-insulator transition. We found that all films exhibit various forms of variable range hopping. Based on these observations and findings, we propose that high degrees of compensation and fluctuating band gaps and band edges are responsible for suppressing the metal-insulator transition in Cu-rich films.

Table of Contents

Table of Contents

List of Tables

List of Figures

Chapter 1

Introduction

1.1 Future Potential & Current Status of Solar Cell Market

A sustainable and economical method of electricity production is vital to quality of life. The global demand for electricity is 2 terrawatts and is increasing at a rate of 2.3% per year.[1] Two thirds of this power comes from burning fossil fuels, a practice that is altering our planet's climate and ecosystem. Direct conversion of sunlight to electricity using solar cells offers a sustainable path to meet the global electricity demand. In fact, covering just 0.1 % of the earth's surface with 20% efficient solar cells would provide the entire global electric energy demand: this is approximately one sixth of the area covered by paved roads in the U.S. Despite its tremendous potential for large-scale energy production, solar cells currently supply less than 1% of the global electricity demand. One of the limiting factors to wide scale photovoltaic deployment (PV) has been its high up front production costs; however this is quickly changing.

Figure 1.1, adapted from a market report performed by Deutsche Bank[2] shows just how rapidly the cost of providing electricity from PV is decreasing within the United States. This figure shows how the cost per kW hr for three of the leading PV technologies, crystalline silicon (C-Si), copper indium gallium diselenide (CIGS) and cadmium telluride (CdTe), has been decaying nearly exponentially. At the same time, the cost of traditional fossil fuel based electricity is anticipated to gradual increase at between 4 to 6% a year, represented by the dashed red line. This figure clearly shows that we are currently on the cusp of "grid parity," or the point at which the cost of electricity over the lifetime of a solar cell is the same as that from traditional, fossil fuel based sources. In some locations in the Southern portion of the United States grid parity has already been reached.

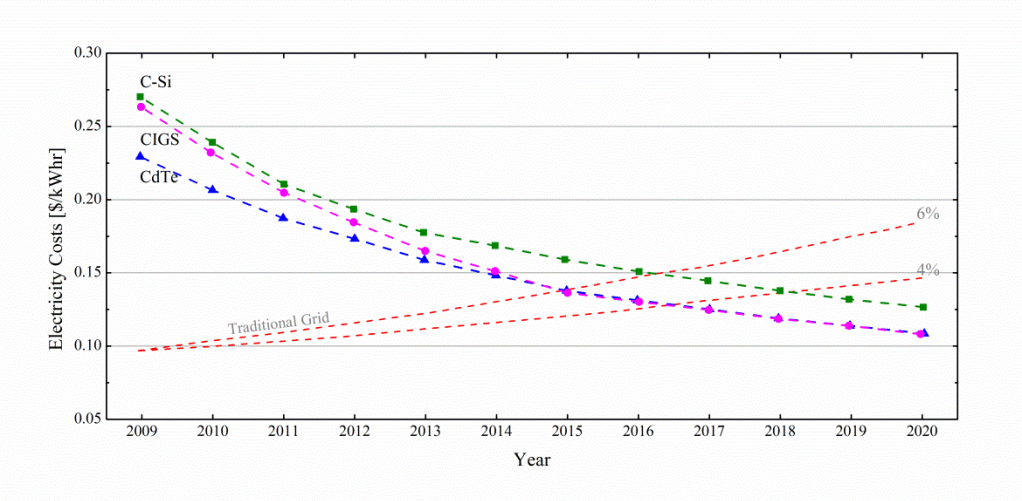

Figure 1.1 The projected costs of traditional fossil fuel electricity production (dotted red line), and projected costs of three existing solar cell technologies, crystalline Si (green), copper indium gallium diselenide (pink) and cadmium telluride (blue). Data adapted from Ref. (2)

As the cost of solar cell production continues to drop, the level of PV deployment is increasing at an equally impressive rate. The global capacity of PV has been doubling every 2.5 years since 1975.[3] In fact, the International Energy Agency estimates that PV may provide up to 11% of the globes electricity needs by the year 2050.[4] To continue bending the solar energy cost curve downwards and to meet GW and TW levels of production, however, places certain demands on the types of solar cells we use and manufacture. Specifically, the materials used within solar cell devices must be inexpensive to process and be abundant within the earth's crust.

The current solar cell market is dominated by crystalline silicon (c-Si) based devices, such that 82% of the solar cell market is comprised of single crystalline or polycrystalline silicon solar cells.[6] This is not without good reason; c-Si based solar cells are a thoroughly studied and mature technology. The highest reported *module* power conversion efficiency for a single crystalline Si solar cell stands at an astonishing 22.9%.[7] This technology is not without its problems though. Electronics grade Si requires extremely energy intensive processing, and hence it is expensive to produce. Furthermore, Si is not an overly effective light absorber, so rigid and thick (100's μm)

layers are necessary. Figure 1.2 shows the cost of just the raw materials per Watt of several different solar cell technologies. Even before the expensive and energy intensive manufacturing of Si wafers, the cost of purified Si puts these devices at a cost disadvantage. Due to this, the market share of c-Si based devices has been decreasing. In fact the title for fastest growing solar cell technology belongs to a class of devices known as thin film solar cells.

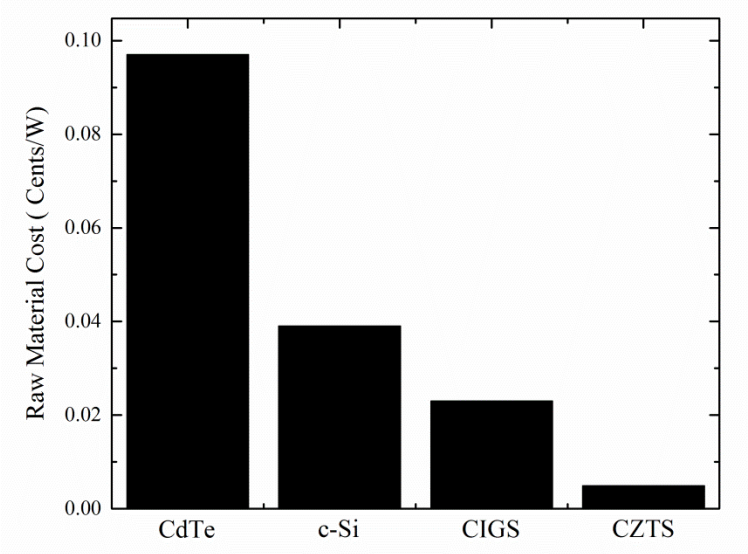

Figure 1.2 The raw material cost per Watt of several different solar absorbers. This data was adapted from Ref. (5)

This class of PV devices utilizes an absorbing layer that can absorb sunlight much more efficiently than Si, so devices may be as thin as a few micrometers, which in turn greatly reduces material demands. Two commercially available thin film solar cells utilize CdTe or CIGS ($CuIn_{1-x}Ga_xSe_2$) as sunlight absorbing layers. In fact CdTe is one of the least expensive options on the solar cell market with a module cost of just \$0.57/W.[8] These solar cell devices have also achieved very high efficiencies in the lab, with CdTe reaching 21.0% [9] and CIGS at 20.8% [10], though their performance in full modules tends towards 10-14%. While the amount of material necessary for constructing these solar cell devices is greatly reduced due to their high absorbtivity, the materials used in CdTe and CIGS devices present issues.

While CdTe is by far the least inexpensive solar cell, the cost of the raw materials needed to make CdTe remains very high, as shown in Figure 1.2. This is largely due to the environmental impact of processing Cd and the scarcity of Te within the earth's crust. The raw material costs for CIGS also remain high and volatile primarily due to In. While In is not nearly as scarce as Te, the demand for In in other electronic industries drives up the cost. In short, while these materials are highly performing, materials availability limits their potential deployment.

A promising material that readily absorbs sunlight and is comprised of inexpensive and earth-abundant elements is copper zinc tin sulfide (Cu_2ZnSnS_4 or CZTS). This p-type semiconductor has a band gap of 1.45 eV making it ideally suited for the solar spectrum. Sulfur atoms on the CZTS lattice may also be replaced with selenium (CZTSSe). Solar cells based on CZTSSe have recently reached 12.6 % power conversion efficiencies,[11] up from a record of 6.7% from as recently as 2008.[12] While efficiencies have risen quickly, finding low-cost, safe, and scalable CZTS synthesis methods has proven challenging. The CZTSSe layer in the record efficiency solar cell is synthesized using hydrazine,[11] an unsafe solvent for large-scale production. A low-cost, scalable method for making CZTS is needed. Moreover, most studies to date have focused on increasing solar cell efficiencies through trial-and-error optimization. This empirical approach has left significant knowledge gaps in our understanding of the relationships between material synthesis, structure and properties. Systematic studies aimed at closing these knowledge gaps are vital for further rational improvements in CZTS based solar cells.

1.2 Challenges in Synthesizing High Performing CZTS Layers

Despite the rapid increases in solar cell efficiencies, there are significant challenges in synthesizing phase pure CZTS layers. Furthermore, relating processing conditions to the electronic properties of the CZTS remains a very active area of investigation.

1.2.1 Synthesizing Phase Pure CZTS

Throughout the literature, many thin CZTS and CZTSe synthesis and deposition methods have been developed, including deposition from nanocrystal dispersions followed by annealing,[13–15] deposition from hydrazine solutions,[16] microwave synthesis,[20] reactive co-evaporation from elemental sources in vacuum,[17,18] reactive co-sputtering with H_2S,[19] and high-temperature sulfidation or selenization of stacked or alloyed Cu-Zn-Sn metallic precursor films deposited by evaporation,[20,21] sputtering,[22,23] or electroplating.[24,25] Each of these methods aims to make CZTS or CZTSe layers that are devoid of any secondary phases, which given the propensity of Cu, Zn, and Sn to react with S individually, is no easy task. The formation of $Cu_{2-x}S$, ZnS, and Sn_xS_y are all thermodynamically favorable under a sufficient S over pressure,[26] all of which act as intermediate phases in CZTS formation.[25,27–29] Even though these phases act as intermediates en route to CZTS formation, the phase stability region for Cu_2ZnSnS_4 is very small, such that slight deviations in atomic compositions make these phases difficult to avoid.[30,31] The challenge of achieving phase pure CZTS is further exacerbated by the fact that off-stoichiometric CZTS films, particularly Cu poor (Cu/(Sn+Zn) ~0.8)and Zn rich (Zn/Sn ~1.1) films, lead to the highest efficiency solar cell devices. [32–34] This is partially alleviated by CZTS's ability to compensate for stoichiometry deviations through the formation of various defect complexes and clusters, but the formation of these clusters has a dramatic effect on the electronic properties, which will be discussed in a later section.[34]

Another difficulty in CZTS synthesis centers around the volatility of SnS. While this binary sulfide nearly inevitably forms as an intermediate phase, it is prone to evaporation at high temperatures or low S pressures.[29,35,36] If CZTS is annealed in an open system or pseudo-open system, this volatilization of SnS can result in Sn deficiencies in the final film. This emphasizes the importance of controlling the vapor phase when reacting or annealing CZTS films. It is clear that whatever synthesis method is pursued, it must afford precise control over the phase and atomic composition in the

final CZTS film. The control over phase composition and relative atomic compositions is further discussed in Chapters two and three.

It must also be noted that the highest performing solar cell devices have a CZTS layer that was synthesized on Mo coated soda-lime glass (SLG).[11,17,18] In order to industrially process glass at lower temperatures than pure SiO_2 significant amounts of impurities including Na_2O (soda) and CaO (lime) are added to the glass. The choice of a SLG substrate is largely a holdover from fabricating CIGS devices where it has been definitively shown that Na within the SLG diffuses through the Mo layer and into the CIGS layer where it helps to increase power conversion efficiencies.[37–42] The effects of Na incorporation into CZTS and CZTSe films and crystals have come under some investigation as of late. It has been shown that the grain size in CZTS films is highly dependent upon Na or even K incorporation, a subject studied and discussed in more detail in Chapter four.[43–46] If the use of SLG, and thus Na and K, has such a dramatic effect on CZTS grain growth, it follows that the final phase composition in CZTS is also a function of impurity content, a topic also discussed in Chapter two.

1.2.2 Linking Synthesis Conditions to Electronic Properties

As mentioned above, there are several factors to consider when synthesizing CZTS layers, including atomic and phase composition, grain size, and impurity content. These parameters undoubtedly have an effect on the electronic properties of CZTS films as well, though this is a topic still undergoing intense investigation.

How the atomic composition influences the properties of CZTS is especially interesting as it has a dramatic effect on solar cell performance. It has been observed both in the thin film case and in single crystals that Cu poor films tend to have lower hole concentrations.[47–49] Computational simulations suggest that the defect Cu_{Zn}^{-} is the dominate contributor to the hole concentration in CZTS films. When this the amount of Cu is decreased, the formation energy of this decrease increases and fewer Cu_{Zn}^{-} defects are formed.[34] However, a shallower acceptor defect V_{Cu}^{-} may also exist in Cu poor conditions, so the change in carrier concentration is not necessarily a linear function of

Cu content.[49] Changes in stoichiometry also affect the types of levels present within the band gap of CZTS, and some of these local fluctuations are widely believed to cause potential fluctuations that are damaging to CZTS performance.[34,50] In particular, CZTS that is Zn poor is more likely to form ($2Cu_{Zn} + Sn_{Zn}$) clusters that can cause significant shrinkage in the effective bandgap. Conversely, films that are Zn rich are more inclined to have ($V_{Cu} + Zn_{Cu}$) clusters form, which effectively widen the bandgap.[34]

Another topic of study is how the presence of Na influences the electronic properties of the CZTS layer. While it has been demonstrated that Na improves CZTS solar cell performance,[44,51] the mechanism behind this improvement is unclear. Studies on single crystals have shown that Na improves mobility and increases carrier concentrations.[52] *Gershon et. al.* have demonstrated that the inclusion of Na may remove deep levels within the gap and passivate grain boundaries.[53] Further study, however is needed, especially in effort to separate the effects of grain growth and Na addition. In Chapter five, the individual affects of stoichiometry, Na concentration, and grain size on carrier concentrations, mobilities, and transport mechanisms are further examined.

1.3 Thesis Overview

In chapter two, we further developed the so called *ex situ* sulfidation method for CZTS synthesis. This method begins by co-sputtering a Cu-Zn-Sn alloyed film from Cu, Cu/Zn, and Cu/Sn targets onto a variety of substrates. This metallic precursor film is then loaded into a quartz ampoule with ~ 1 mg of S, evacuated to a base pressure of ~ 10^{-6} Torr and flame sealed. The evacuated quartz ampoule is then loaded into a furnace where we heated it to a desired sulfidation temperature (T_S) between 100 ^{o}C and 600 ^{o}C for 8 hrs, after which it is cooled to room temperature naturally. This method is advantageous in studying CZTS formation as it is a closed isothermal system such that the temperature, pressure, and species present are always known. After sulfidation, the phase composition was thoroughly examined by X-ray diffraction (XRD) and Raman spectroscopy. The film morphology and atomic compositions were observed by scanning electron microscopy (SEM) and energy dispersive X-ray spectroscopy (EDS). We

examined CZTS formation as a function of T_S on a total of five different substrates including the impurity laden SLG and Pyrex, as well as impurity free fused quartz, crystalline quartz, and crystalline sapphire. We found that regardless of substrate, phase pure CZTS is achieved at T_S = 600 ^oC. CZTS films deposited on SLG, however, approach phase purity at much lower temperatures (nearly phase pure at T_S = 400 ^oC) than all over substrates. There are significant differences in the grain structure of films grown on SLG versus all other substrates as well. After sulfidation at 600 ^oC, the CZTS grown on SLG has an average grain size of 0.97 µm, while films grown on fused quartz had an average grain size of just 0.17 µm. This suggested that the some impurity within SLG, likely Na or K, was readily released into the CZTS film during sulfidation where it not only enhanced grain growth, but allowed the film to reach phase purity at lower temperatures. This chapter is currently under review as Melissa Johnson, Michael Manno, Xin Zhang, C. Leighton, and Eray S. Aydil, "Substrate and Temperature Dependence of the formation of the Earth Abundant Solar Absorber Cu_2ZnSnS_4 by *ex situ* Sulfidation of Co-sputtered Cu-Zn-Sn Films"

In chapter three, we explore methods to control the stoichiometry of CZTS synthesized by the *ex situ* sulfidation method and find that the Sn content is remarkably self regulating. Precursors films that were initially Sn rich, up to 45% Sn initially, underwent copious amounts of Sn loss via the volatilization of SnS, until Cu/Sn ~ 2. Similarly, precursor films that were initially Sn deficient could correct the Sn deficiency such that Cu/Sn ~2 with the inclusion of ~ 1 mg of elemental Sn in the sulfidation ampoule. The relative compositions of Cu and Zn within the final CZTS film were simply controlled by the content in the precursor film by varying the sputtering conditions. To study the mechanism behind the self regulating nature of Sn, we performed a set of time dependent experiments at T_S = 300 ^oC. This temperature was chosen as it is at the onset of sulfide formation. We found that early on in the sulfidation process, the $Cu_{6.26}Sn_5$ alloy that formed prior to S vaporization dissociated and sulfidized to form CuS and SnS, as well as some Cu_2SnS_3. There was not enough CuS to completely convert all of the SnS to Cu_2SnS_3, so the majority of Sn left the film as SnS vapor.

Eventually Cu and Zn were released from the Cu_5Zn_8 alloy that had also formed earlier on and formed CuS and ZnS. The SnS vapor within the ampoule then reacted with the newly generated CuS to form more Cu_2SnS_3, and eventually CZTS which increased the overall Sn content within the film. This demonstrated that during sulfidation, the majority of Sn leaves the film as SnS vapor, and is only reincorporated back into the film as Cu_2SnS_3, which like CZTS, has a Cu to Sn ratio of 2. This chapter has been prepared for submission as "Melissa Johnson, Cody Wrasman, Xin Zhang, Michael Manno, C. Leighton, and Eray S. Aydil, "Tuning the composition of Cu_2ZnSnS_4 synthesized via *ex situ* sulfidation of co-sputtered Cu-Zn-Sn films."

In the fourth chapter we revisit the results found in chapter 1, namely the enhancement in CZTS grain size that accompanies the use of SLG substrates. We found that including a clean, uncoated piece of SLG within the sulfidation ampoule next to a film deposited on low impurity Pyrex or impurity free crystalline quartz results in a dramatic enhancement in the CZTS grain size. This demonstrated conclusively that the beneficial impurities found within SLG are also volatile in a S containing atmosphere at 600 ^oC. We then turned to TOF-SIMS to find out exactly which impurities diffuse into a CZTS layer deposited on SLG, and which were volatilized from SLG and incorporated into neighboring films on other substrates. We found nearly all alkali and alkaline metals, specifically Na, K, Ca, and Mg, will readily diffuse into the CZTS layer from the SLG especially in the absence of a diffusion barrier like Mo. We then found that Na, K, and Ca were all readily volatilized from the SLG and incorporated into neighboring CZTS films on quartz and Pyrex. Curiously, we found that the small grained films grown on Pyrex in the absence of SLG had high levels of Na, as much the large grained films grown on quartz. This first suggests that Na may be sitting at the grain boundaries of the CZTS film, such that a film with a greater grain boundary density (*i.e.* small grained) contains more Na. This also suggests that there is an impurity concentration threshold that must be passed *during* growth in order to enhance the grain size. To elucidate whether Na, K, or Ca was responsible for the grain growth, we developed a new method to introduce these impurities individually through the vapor phase. Prior to loading the precursor film and

S into the quartz tube, the tube was coated with an aqueous solution of either NaOH, KOH, or $CaOH_2$ and then dried such that only the hydroxide coating remained. Sulfidation then proceeded normally. It was found that Na and K can greatly enhance the grain size in CZTS films while the presence of Ca had little to no effect. This chapter was published as Melissa Johnson, Sergey Baryshev, Elijah Thimsen, Michael Manno, Xin Zhang, Igor V. Veryovkin, C. Leighton, and Eray S. Aydil, "Alkali-metal-enhanced grain growth in Cu_2ZnSnS_4 thin films," *Energy Envrion. Sci.* **2014**, *7*, 1931.

In the fifth chapter, study the influences of stoichiometry, grain size, impurity content, and phase purity on the electronic properties of CZTS films. Specifically, we studied how each of these parameters affected the carrier concentration, mobility, and transport mechanisms of the CZTS films through the use of Hall effect and temperature dependent resistivity measurements. We examined three different stoichiometries, such that Cu/Zn was 2.4 (Cu rich), 2.0 (stoichiometric), and 1.9 (Cu poor), while in all films Cu/Sn ~ 2. The grain size was varied in the absence of Na addition by varying the S pressure during growth, such that higher S pressure resulted in a larger grain size. One set of Na loading in the CZTS films was also examined. Finally, we examined a film Cu poor film (Cu/Zn = 1.8) that also had CuS impurity phases present. All films were found to be p-type insulators, however, there were some stark differences depending on treatment. We observed a very strong correlation between carrier concentration and stoichiometry, with all Cu rich and CuS containing films having hole concentrations in excess of 10^{20} cm^{-3}, while Cu poor samples had carrier concentrations as low as 2.7 x 10^{17} cm^{-3}. While increasing the grain size of the films without the addition of Na led to an expected increase in mobility, it also led to a drop in carrier concentrations. We hypothesize this may be due to an increase in order such that defect states within the grains are eliminated, or that the grain boundaries themselves may have high defect densities. The addition of Na to the Cu poor and stoichiometric films resulted in a large increase in carrier concentrations and a large decrease in resistivity. However, temperature dependent resistivity measurements suggested that the addition of Na led to a large increase in disorder within the gap. These results indicate that large grained Cu poor

or stoichiometric samples with very moderate levels of Na may make the best candidates for solar cell devices. This chapter has been prepared for submission as "Melissa Johnson, Cody Wrasman, Xin Zhang, Michael Manno, C. Leighton, and Eray S. Aydil, "The influence of stoichiometry, grain size, and Na addition on the electronic properties of Cu_2ZnSnS_4 thin films."

1.4 References

(1) *International Energy Outlook 2013*; 2013.

(2) O'Rourke, S. No Title http://www.slideshare.net/gwsolar/pv-status-and-pathways-stephen-orourke .

(3) Norris, D. J.; Aydil, E. S. *Science* **2012**, *338*, 625–626.

(4) *Technology Roadmap: Solar Photovoltaic Energy*; IEA Technology Roadmaps; OECD Publishing, 2014.

(5) Wadia, C.; Alivisatos, a P.; Kammen, D. M. *Environ. Sci. Technol.* **2009**, *43*, 2072–2077.

(6) Wolden, C. A.; Kurtin, J.; Baxter, J. B.; Repins, I.; Shaheen, S. E.; Torvik, J. T.; Rockett, A. A.; Fthenakis, V. M.; Aydil, E. S. *J. Vac. Sci. Technol. A Vacuum, Surfaces, Film.* **2011**, *29*, 030801.

(7) Zhao, J.; Wang, A.; Yun, F.; Zhang, D.; Roche, D. M.; Wenham, S. R.; Green, M. A. *Prog. Photovoltaics Res. Appl.* **1997**, *5*, 269–276.

(8) No Title http://cleantechnica.com/2013/11/07/first-solar-reports-largest-quarterly-decline-cdte-module-cost-per-watt-since-2007/.

(9) No Title http://investor.firstsolar.com/releasedetail.cfm?ReleaseID=864426.

(10) Jackson, P.; Hariskos, D.; Wuerz, R.; Wischmann, W.; Powalla, M. *Phys. Status Solidi - Rapid Res. Lett.* **2014**, *8*, 219–222.

(11) Wang, W.; Winkler, M. T.; Gunawan, O.; Gokmen, T.; Todorov, T. K.; Zhu, Y.; Mitzi, D. B. *Adv. Energy Mater.* **2014**, *4*.

(12) Katagiri, H.; Jimbo, K.; Yamada, S.; Kamimura, T.; Maw, W. S.; Fukano, T.; Ito, T.; Motohiro, T. *Appl. Phys. Express* **2008**, *1*, 041201.

(13) Guo, Q.; Ford, G. M.; Yang, W.-C.; Walker, B. C.; Stach, E. a; Hillhouse, H. W.; Agrawal, R. *J. Am. Chem. Soc.* **2010**, *132*, 17384–17386.

(14) Guo, Q.; Hillhouse, H.; Agrawal, R. *J. Am. Chem. Soc.* **2009**, 11672–11673.

(15) Khare, A.; Wills, A. W.; Ammerman, L. M.; Norris, D. J.; Aydil, E. S. *Chem. Commun.* **2011**, *47*, 11721–11723.

(16) Todorov, T. K.; Reuter, K. B.; Mitzi, D. B. *Adv. Mater.* **2010**, *22*, E156–9.

(17) Repins, I.; Beall, C.; Vora, N.; DeHart, C.; Kuciauskas, D.; Dippo, P.; To, B.; Mann, J.; Hsu, W.-C.; Goodrich, A.; Noufi, R. *Sol. Energy Mater. Sol. Cells* **2012**, *101*, 154–159.

(18) Shin, B.; Gunawan, O.; Zhu, Y.; Bojarczuk, N. A.; Chey, S. J.; Supratik, G. *Prog. Photovoltaics Res. Appl.* **2013**, 72–76.

(19) Ericson, T.; Kubart, T.; Scragg, J. J.; Platzer-Björkman, C. *Thin Solid Films* **2012**, *520*, 7093–7099.

(20) Katagiri, H.; Ishigaki, N.; Ishida, T.; Saito, K. *Jpn. J. Appl. Phys.* **2001**, *40*, 500–504.

(21) Cheng, A.-J.; Manno, M.; Khare, A.; Leighton, C.; Campbell, S. A.; Aydil, E. S. *J. Vac. Sci. Technol. A Vacuum, Surfaces, Film.* **2011**, *29*, 051203.

(22) Katagiri, H.; Jimbo, K.; Maw, W. S.; Oishi, K.; Yamazaki, M.; Araki, H.; Takeuchi, A. *Thin Solid Films* **2009**, *517*, 2455–2460.

(23) Fernandes, P. A.; Salomé, P. M. P.; da Cunha, A. F.; Schubert, B.-A. *Thin Solid Films* **2011**, *519*, 7382–7385.

(24) Scragg, J.; Berg, D.; Dale, P. *J. Electroanal. Chem.* **2010**, *646*, 52–59.

(25) Schurr, R.; Hölzing, A.; Jost, S.; Hock, R.; Voβ, T.; Schulze, J.; Kirbs, A.; Ennaoui, A.; Lux-Steiner, M.; Weber, A.; Kötschau, I.; Schock, H.-W. *Thin Solid Films* **2009**, *517*, 2465–2468.

(26) Vaughan, D.; Craig, J. *Mineral chemistry of metal sulfides*; Cambridge University Press: London, UK, 1978.

(27) Fairbrother, A.; Fontané, X.; Izquierdo-Roca, V.; Espíndola-Rodríguez, M.; López-Marino, S.; Placidi, M.; Calvo-Barrio, L.; Pérez-Rodríguez, A.; Saucedo, E. *Sol. Energy Mater. Sol. Cells* **2013**, *112*, 97–105.

(28) Han, J.; Shin, S. W.; Gang, M. G.; Kim, J. H.; Lee, J. Y. *Nanotechnology* **2013**, *24*, 095706.

(29) Weber, A.; Mainz, R.; Schock, H. W. *J. Appl. Phys.* **2010**, *107*, 013516.

(30) Olekseyuk, I. D.; Dudchak, I. V.; Piskach, L. V. *J. Alloys Compd.* **2004**, *368*, 135–143.

(31) Chen, S.; Gong, X. G.; Walsh, A.; Wei, S.-H. *Appl. Phys. Lett.* **2010**, *96*, 021902.

(32) Mitzi, D. B.; Gunawan, O.; Todorov, T. K.; Wang, K.; Guha, S. *Sol. Energy Mater. Sol. Cells* **2011**, *95*, 1421–1436.

(33) Katagiri, H.; Jimbo, K.; Tahara, M. *MRS Proc.* **2009**, *1165*.

(34) Chen, S.; Walsh, A.; Gong, X.-G.; Wei, S. *Adv. Mater.* **2013**, *25*, 1522–1539.

(35) Scragg, J. J.; Ericson, T.; Kubart, T.; Edo, M.; Platzer-Björkman, C. *Chem. Mater.* **2011**, 4625–4633.

(36) Redinger, A.; Berg, D. M.; Dale, P. J.; Siebentritt, S. *J. Am. Chem. Soc.* **2011**, *133*, 3320–3323.

(37) Ruckh, M.; Schmid, D.; Kaiser, M.; Schaffler, T.; Walter, T.; Schock, H. W. *Sol. Energy Mater. Sol. Cells* **1996**, *41/42*, 335–343.

(38) Nakada, T.; Iga, D.; Ohbo, H.; Kunioka, A. *Jpn. J. Appl. Phys.* **1997**, *73236*, 732–737.

(39) Kronik, L.; Cahen, D.; Schock, H. *Adv. Mater.* **1998**, *10*, 31–36.

(40) Rockett, A. *Thin Solid Films* **2005**, *480-481*, 2–7.

(41) Cho, D.-H.; Lee, K.-S.; Chung, Y.-D.; Kim, J.-H.; Park, S.-J.; Kim, J. *Appl. Phys. Lett.* **2012**, *101*, 023901.

(42) Ishizuka, S.; Yamada, A.; Islam, M. M.; Shibata, H.; Fons, P.; Sakurai, T.; Akimoto, K.; Niki, S. *J. Appl. Phys.* **2009**, *106*.

(43) HLAING Oo, W. M.; Johnson, J. L.; Bhatia, A.; Lund, E. A.; Nowell, M. M.; Scarpulla, M. A. *J. Electron. Mater.* **2011**, *40*, 2214–2221.

(44) Sutter-Fella, C. M.; Stukelberger, J. A.; Hagendorfer, H.; Mattina, F. La; Kranz, L.; Nishiwaki, S.; Uhl, A. R.; Romanyuk, Y. E.; Tiwari, A. N. *Chem. Mater.* **2014**, *26*, 1420–1425.

(45) Chernomordik, B. D.; Béland, A. E.; Deng, D. D.; Francis, L. F.; Aydil, E. S. *Chem. Mater.* **2014**, *26*, 3191–3201.

(46) Johnson, M.; Baryshev, S. V.; Thimsen, E.; Manno, M.; Zhang, X.; Veryovkin, I. V.; Leighton, C.; Aydil, E. S. *Energy Environ. Sci.* **2014**, *7*, 1931.

(47) Nagaoka, A.; Miyake, H.; Taniyama, T.; Kakimoto, K.; Yoshino, K. *Appl. Phys. Lett.* **2013**, *103*, 112107.

(48) Tanaka, T.; Sueishi, T.; Saito, K.; Guo, Q.; Nishio, M.; Yu, K. M.; Walukiewicz, W. *J. Appl. Phys.* **2012**, *111*, 053522.

(49) Ruan, C.-H.; Huang, C.-C.; Lin, Y.-J.; He, G.-R.; Chang, H.-C.; Chen, Y.-H. *Thin Solid Films* **2014**, *550*, 525–529.

(50) Romero, M. J.; Du, H.; Teeter, G.; Yan, Y.; Al-Jassim, M. M. *Phys. Rev. B* **2011**, *84*, 165324.

(51) Li, J. V.; Kuciauskas, D.; Young, M. R.; Repins, I. L. *Appl. Phys. Lett.* **2013**, *102*, 163905.

(52) Nagaoka, A.; Miyake, H.; Taniyama, T.; Kakimoto, K.; Nose, Y.; Scarpulla, M. A.; Yoshino, K. *Appl. Phys. Lett.* **2014**, *104*, 152101.

(53) Gershon, T.; Shin, B.; Bojarczuk, N.; Hopstaken, M.; Mitzi, D. B.; Guha, S. *Adv. Energy Mater.* **2014**, 1400849.

Chapter 2

Substrate and Temperature Dependence of the formation of the Earth Abundant Solar Absorber Cu_2ZnSnS_4 by *ex situ* Sulfidation of Co-sputtered Cu-Zn-Sn Films

This was previously published as: Johnson, M.; Manno, M.; Zhang, X.; Leighton, C.; Aydil, E. S. (2014). Substrate and temperature dependence of the formation of the Earth abundant solar absorber Cu_2ZnSnS_4 by *ex situ* sulfidation of cosputtered Cu-Zn-Sn films. *Journal of Vacuum Science & Technology A: Vacuum, Surfaces, and Films, 32*(6), 061203. doi:10.1116/1.4901091 Reproduced by permission Journal of Vacuum Science and Technology A

2.1 Introduction

The recent rapid increase in power conversion efficiencies of thin-film solar cells based on the *p*-type semiconductors Cu_2ZnSnS_4 (CZTS) and $Cu_2ZnSnSe_4$ (CZTSe) attests to their potential as low-cost, earth-abundant alternatives to CdTe and $CuIn_{1-x}Ga_xSe_2$ (CIGS), the two leading commercial thin film solar absorber materials.[1] Many articles have identified the attractive attributes of CZTS and CZTSe for thin-film solar cells.[2-6] These include their high absorption coefficient in the visible region of the solar spectrum ($>10^4$ cm^{-1} for $\lambda<1000$ nm),[7] a tunable band gap from 1 eV for CZTSe to 1.45 eV for CZTS,[8] and a high relative abundance of their constituent elements. While record efficiencies have now reached 12.04% for $Cu_2ZnSn(S_{1-x}Se_x)_4$[9] and 8.4% for CZTS,[10] these values still fall significantly short of the 20.4% achieved in CIGS solar cells.[11] Closing this performance gap requires a deep understanding of the relations among synthesis, structure and properties of CZTS and CZTSe films.

To date, many thin CZTS and CZTSe film formation methods have been developed, including deposition from nanocrystal dispersions followed by annealing,[12-18] deposition from hydrazine solutions,[19] microwave synthesis,[20] reactive co-evaporation

from elemental sources in vacuum,[5,10,21] reactive co-sputtering with H_2S,[22] and high-temperature sulfidation or selenization of stacked or alloyed Cu-Zn-Sn metallic precursor films deposited by evaporation,[23,24] sputtering[25,26] or electroplating.[27,28] Sulfidation of Cu-Zn-Sn thin films is a particularly attractive approach because it can be easily scaled up and adopted for manufacturing. Indeed, this is one of the approaches used for producing commercial CIGS solar cells. However, this seemingly straightforward method is actually quite complicated because evaporation and diffusion of multiple elements compete with numerous solid and vapor phase reactions to determine the microstructure and phase composition of the thin films. These processes must be balanced and controlled to synthesize films with suitable microstructure, composition, and electronic properties for solar cells. Recent studies have already revealed that sulfidation of Cu-Zn-Sn films begins with sulfur diffusion into the film followed by reactions that form the binary metal sulfides, $Cu_{2-x}S$, Sn_xS_y, and ZnS.[28-30] Sulfur diffusion likely begins through the grain boundaries in the precursor film followed by diffusion into the grains. A variety of ternary copper tin sulfides form next; precisely which phases form appears to depend on the initial composition of the Cu-Zn-Sn precursor film.[28] These ternary phases and ZnS are eventually converted to CZTS at temperatures exceeding 480 ^oC. However, under some conditions it has been shown that CZTS is unstable and may decompose back to the binary sulfides.[31-33] This is particularly problematic because SnS has high vapor pressure and can evaporate from the film, leaving the film Sn poor and possibly also filled with impurity binary sulfide phases. Using solid SnS in addition to S during sulfidation mitigates this problem,[32,33] but most sulfidation processes are carried out in open or in quasi-closed systems (*e.g.*, graphite boxes with unsealed lids) such that S and SnS vapor pressures are uncontrolled and unknown. In contrast, isothermal *ex situ* sulfidation of Cu-Zn-Sn films in an evacuated and sealed quartz ampoule with precisely metered S and Sn allows accurate control and knowledge of the S and SnS vapor pressures as well as the sulfidation temperature. Platzer-Björkman *et al.* employed this approach to explore the effects of changing precursor film composition,[34] but they were unable to achieve phase-pure CZTS and detected the persistent presence of an unidentifiable impurity phase

through X-ray diffraction. Despite the presence of impurity phases, working solar cell devices were fabricated from these films.

To date, the highest efficiency solar cells have all been grown on Mo-coated soda-lime glass (SLG).[9,10] The use of SLG as a substrate is a carryover from CIGS solar cells, where it has been shown that Na diffusion from the SLG drastically increases the power conversion efficiencies. Indeed, SLG hosts many impurities such as Na, Mg, Ca, and K that may diffuse out of the glass and into the CZTS films. A few studies of CZTS synthesis with Na and K addition have shown enhanced grain growth[35-37] but achieving CIGS like performance will require a better understanding of the effects of impurity diffusion from the substrate into the CZTS films.

Herein we present a comprehensive study of the effects of substrate and sulfidation temperature on the microstructure and phase composition of CZTS films formed through isothermal sulfidation of co-sputtered Cu-Zn-Sn alloy thin films. We found that regardless of the substrate, nominally phase-pure CZTS is obtained after 8 hours of sulfidation at 600 ^{o}C and with >30 Torr of S pressure. However, the substrate strongly affects the film's morphology: films synthesized on SLG exhibited µm sized grains while sulfidation on other substrates resulted in much smaller (100's of nm) grains. Films grown on SLG also reached higher phase purity at lower sulfidation temperatures.

2.2 Experimental

CZTS films were synthesized by *ex situ* sulfidation of Cu-Zn-Sn metal alloy precursor films co-sputtered from Cu, Cu-Zn and Cu-Sn targets onto five different substrates including single crystal quartz (Q), fused quartz (FQ), sapphire (SP, Al_2O_3), Pyrex (P), and SLG. These substrates were chosen to elucidate the effects of substrate crystallinity and substrate impurities on the formation of CZTS. The elemental compositions of the SLG and Pyrex substrates were measured using inductively coupled plasma mass spectrometry (ICP-MS) and were reported in reference 36. The precursor films were DC magnetron sputtered at room temperature and sulfidized isothermally at temperatures between 100 and 600 ^{o}C. The base pressure of the sputtering chamber was $2x10^{-7}$ Torr. Alloy targets were used in lieu of pure metal targets because Zn has very high vapor

pressure (0.1 Torr at 400 ^{o}C) and Sn melts at a very low temperature (232 ^{o}C). The precursor films deposited on SLG, FQ, and Q were sputtered from a Cu-Zn (40:60) target and a Cu-Sn (35:65) target at 10 mTorr Ar pressure. The precursor films deposited on P and SP were sputtered from a pure Cu target, a Cu-Zn (20:80) target and a Cu-Sn (35:65) target at 6 mTorr Ar pressure. The sputtering rate from each target was varied using the sputtering power to achieve the desired precursor film composition. During deposition on SP and P, the sputtering powers were 40, 115, and 34 W for Cu, Cu-Sn, and Cu-Zn targets, respectively. At these powers the deposition rates were 0.091, 0.18 and 0.16 nm/s for the Cu, Cu-Sn, and Cu-Zn targets, respectively. During deposition on SLG, FQ, and XQ, the sputtering powers were 75 W and 25 W for the Cu-Sn and Cu-Zn targets, respectively. At these powers the deposition rates were 0.12 and 0.027 nm/s for the Cu-Sn, and Cu-Zn targets, respectively. Each set of targets was carefully calibrated by depositing films at various sputtering powers for several different durations and measuring their thicknesses using cross sectional SEM. Calibration ensured that the precursor films were of equal thickness and approximately the same composition. The thicknesses of the as-deposited precursor films were all within 10% of 270 nm. The elemental composition of the films was nominally 50% Cu, 20% Zn and 30% Sn (Table 2.1) as determined by energy-dispersive x-ray spectroscopy (EDS). Sulfidized film thicknesses were ~ 1 µm. The precursor films were chosen to be Sn rich to compensate for anticipated and well-documented Sn loss during annealing and sulfidation experiments.[31-33] The metallic alloy precursor films were sealed in an evacuated quartz ampoule with 1 mg of S, loaded into a box furnace, and heated at a rate of 6.5 ^{o}C/min to the desired sulfidation temperature. The base pressure of the 10 cm long 1 cm internal diameter ampoule was ~ 10^{-6} Torr. The film was sulfidized isothermally for 8 hours before cooling naturally to room temperature. The sulfidation temperature, T_s, was varied from 100 to 600 ^{o}C in 100-degree increments. As the ampoule is heated, S melts at 115 ^{o}C and the entire 1 mg charge vaporizes completely by 255 ^{o}C. Thus, the S pressure in the ampoule follows the vapor pressure curve up to 255^{o}C and thereafter increases according to the ideal gas law, varying from 17.5 Torr at 255^{o}C to 36 Torr at 600 ^{o}C.

The phase composition of the films was examined by X-ray diffraction (XRD) and Raman spectroscopy. XRD was collected using either a Bruker–AXS microdiffractometer (for SP and P films) or a Bruker D8 Discover system (for FQ, Q, and SLG films), each utilizing a Cu Kα source and equipped with a Hi-Star 2D area detector. The X-ray beam was collimated to a 0.8 mm spot size. Raman spectroscopy is essential to differentiate CZTS, Cu_2SnS_3, and ZnS because the XRD reflections from these materials overlap.[24] Raman spectra were collected at room temperature using a WiTec alpha300R confocal Raman microscope with a UHTS300 spectrometer and a DV401 CCD detector. An Omnichrome Ar ion laser with a wavelength of 514.5 nm and a beam spot size of ~300 nm was used to illuminate the films. Raman scattering was collected in the backscattering geometry using an 1800 lines/mm grating with a spectral resolution of 0.02 cm^{-1}. The morphology and atomic composition of the sulfidized films were examined with a JEOL 6500 scanning electron microscope (SEM) equipped with an energy dispersive spectrometer (EDS). The electron energy was 15 keV for both imaging and EDS measurements; at this energy, EDS samples the top ~ 2 μm of the surface, ensuring that the entire depth of the sulfidized film is included in the analysis. Average grain sizes were determined by averaging across a minimum of 100 grains per sample.

A Physical Electronics model 545 Auger electron spectrometer (AES) equipped with a differentially pumped Ar ion source for sputtering was used to measure the composition as a function of depth of the precursor film deposited on Pyrex. The film/Pyrex interface was determined from the onset of severe charging due to the insulating nature of the Pyrex. The sputtering rate was calibrated using the film thickness measured from the tilted view scanning electron micrographs. Depth profiles of sulfidized films were also attempted, though the highly insulating nature of the films resulted in significant charging effects. The elemental profiles of similar films sulfidized at 600 ^oC measured by TOF-SIMS depth profiling can be found in Reference 36.

2.3 Results and Discussion

We describe our major conclusions by focusing on the films sulfidized on SLG and FQ because the most significant differences were found between substrates that contain alkali metal impurities (SLG and P) and substrates that do not contain these impurities (FQ, Q and SP). We note that the crystallinity of the substrate did not influence the microstructure and phase composition of the sulfidized films significantly. Both SLG and FQ are amorphous. FQ is nominally impurity free whereas SLG is laden with various impurities, including Na (Table 2.1). Pyrex is also amorphous but contains lower concentrations of impurities than SLG, which makes it intermediate between FQ and SLG. Q and SP are crystalline and nominally impurity free.

2.3.1 Effect of Sulfidation Temperature on Structure and Phase Composition

The XRD from the as-deposited Cu-Zn-Sn precursor films on all films (Figure 2.1) shows that they are comprised of the hexagonal $Cu_{6.26}Sn_5$ alloy, FCC Cu, HCP Zn, and tetragonal β-Sn. The XRD from precursor films deposited on all substrates were similar.The strong diffraction lines expected from FCC Cu, HCP Zn, and Cu_5Zn_8 are all near $2\theta = 43\text{-}44^o$ and overlap with each other. However, the weaker unique reflections for Cu_5Zn_8 are absent, which suggests that Cu and Zn are present in their elemental form. The absence of a Cu-Zn alloy is surprising and suggests that mixing may be limited even in co-sputtered films due to low mobility. However, the Cu-Zn binary phase diagram shows that solubility of Zn in FCC Cu is significant (~30 at. %) at room temperature. Very little shift in the FCC Cu XRD pattern would be expected even with 30 at. % Zn. Thus, significant amounts of Zn could be dissolved in the Cu phase.

It should also be noted that the Cu and Zn phases are textured in the (111) and (101) directions, respectively. In fact, all the other reflections for Cu and Zn are absent. The Sn phase is also slightly textured in the (200) direction. This texturing is most apparent from the 2D area detector image of the XRD. Instead of a uniform intensity arc,

expected for diffraction from randomly oriented grains, the intensity is concentrated near the center of the arc at 30.65^{o}, corresponding to the Sn (200) reflection (See Figure 2.2).

Table 2.1 The thermal expansion coefficients of all substrates, the strain and softening points of the amorphous substrates, and typical *added* impurity concentrations (mol %). Sapphire (SP), single crystal quartz (Q), fused quartz (FQ), Pyrex (P), and soda lime glass (SLG).

Substrate	Thermal Expansion Coefficient (/^{o}C)	Strain Point (^{o}C)	Softening Point (^{o}C)	Added Impurities (mole%)
SP	7.5×10^{-6}			
Q	$\alpha_{11} = 13.71 \times 10^{-6}$ $\alpha_{33} = 7.48 \times 10^{-6}$			
FQ	5.5×10^{-7}	1120	1683	
P	32.5×10^{-7}	510	821	B_2O_3 (11.19 %) Na_2O (4 %) CaO(0.03 %) Al_2O_3 (1 %) K_2O (0.04 %)
SLG	8.6×10^{-6}	490	575	Na_2O (13 %) CaO (9 %), MgO (6 %), Al_2O_3 (0.08 %), Fe_2O_3 (0.04 %), K_2O (0.02 %)

Table 2.2 The elemental composition of films sulfidized on SLG and FQ as determined by EDS. The standard deviations of four separate measurements at the same location on a nominally phase pure CZTS film (within the detection limits of XRD and Raman) are ±1.9 at%

	SLG				FQ				Q			
T_s (^{o}C)	**Cu**	**Zn**	**Sn**	**S**	**Cu**	**Zn**	**Sn**	**S**	**Cu**	**Zn**	**Sn**	**S**
Precursor	50	18	32	0	49	21	30	0	50	20	30	0
100	50	19	31	0	50	23	28	0	50	20	30	0
200	45	27	24	4	42	24	26	8	47	19	29	5
300	34	6	11	49	31	11	9	49	34	10	7	49
400	24	13	13	50	27	10	14	49	26	13	13	48
500	25	12	14	49	25	11	14	50	26	11	14	49
600	25	13	13	49	27	10	14	49	27	10	14	49

	P				SP			
T_s (^{o}C)	**Cu**	**Zn**	**Sn**	**S**	**Cu**	**Zn**	**Sn**	**S**
Precursor	47	22	30	0	44	24	32	0
100	47	28	25	0	44	27	29	0
200	43	33	20	4	41	32	23	4
300	30	12	10	48	23	16	13	48
400	24	13	13	50	22	16	13	50
500	23	15	12	50	22	15	13	50
600	24	14	13	49	23	16	12	49

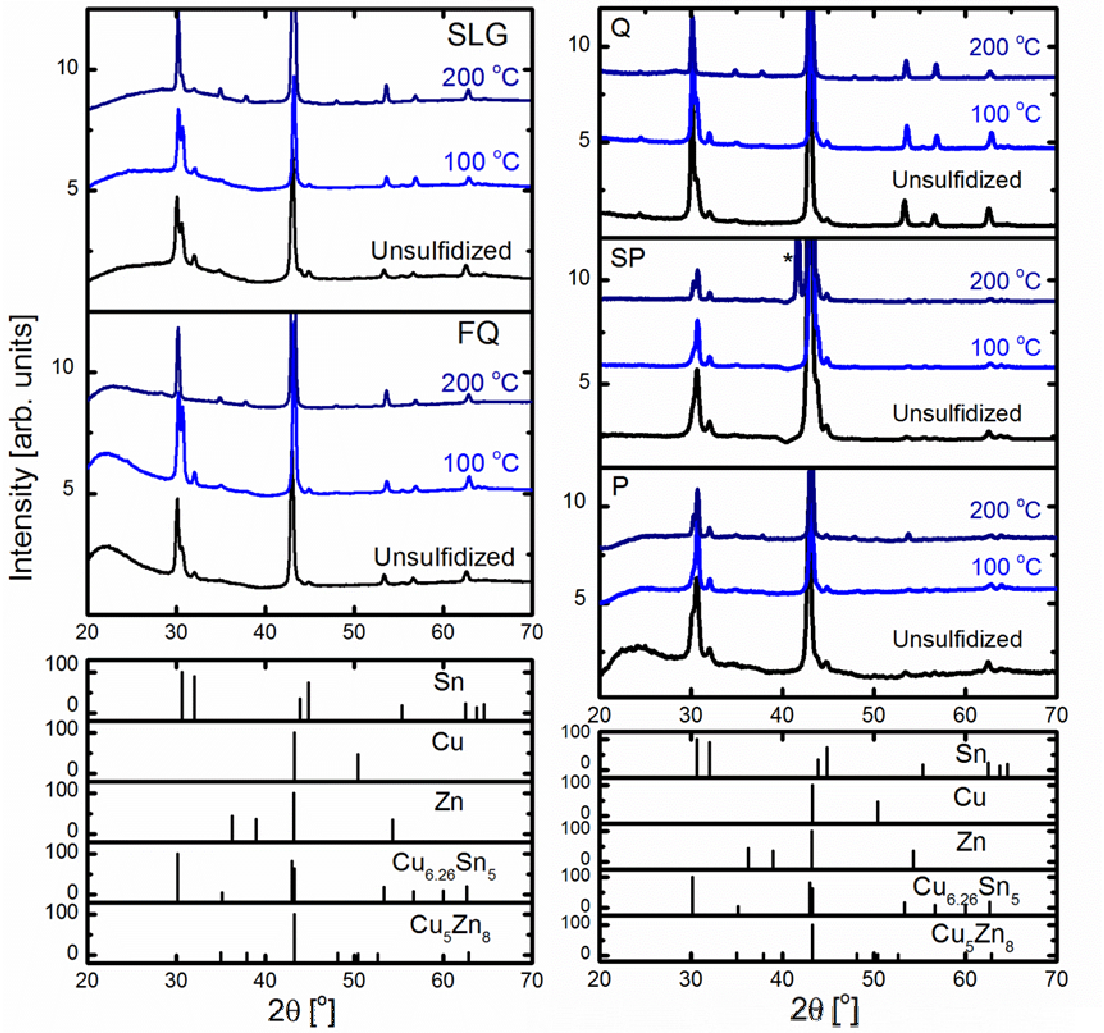

Figure 2.1 X-ray diffraction from films on all substrates before and after sulfidation at 100 °C and 200 °C. The bottom panels show the expected powder diffraction patterns from Sn, Cu, Zn, $Cu_{6.26}Sn_5$, and Cu_5Zn_8 for comparison.

Scherrer analysis of the Sn and $Cu_{6.26}Sn_5$ phases indicates that the precursor films are nanocrystalline with an average grain size of 30 nm, consistent with SEMs of the precursor films (Figure 2.3(a)). SEM images and a sampling of various areas with EDS showed that the composition and morphology of the Cu-Zn-Sn precursor films were laterally uniform. Auger electron spectroscopy sputter depth profiling (Figure 2.4)

showed that the film composition was also quite uniform through the depth of the film, though the top 30 nm of the surface was slightly Sn and Zn rich at the expense of Cu.

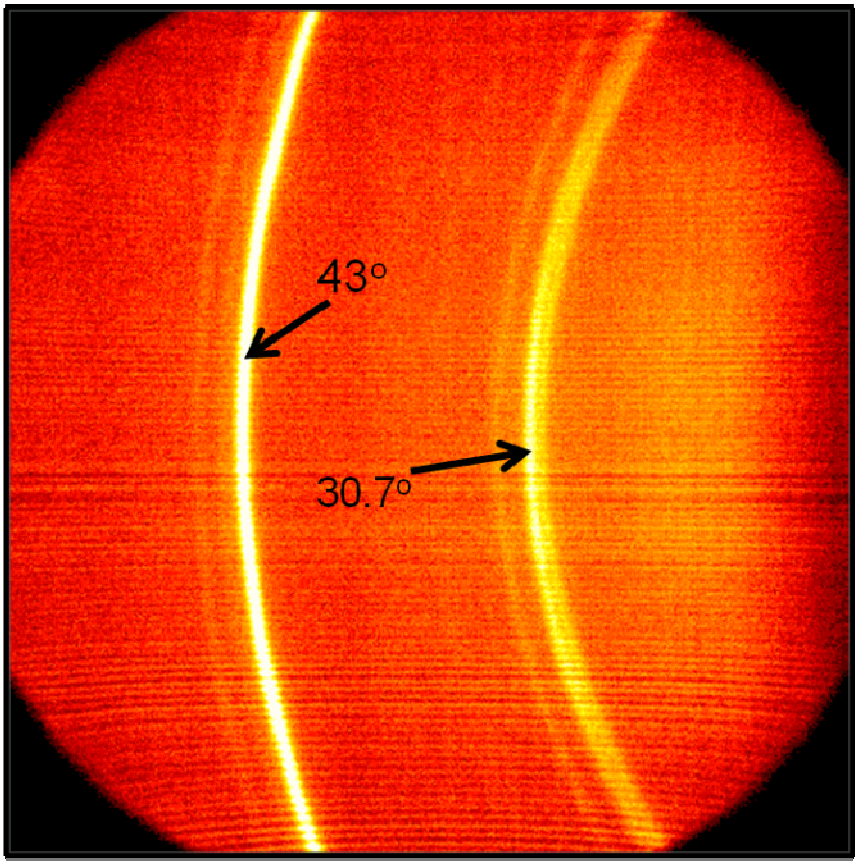

Figure 2.2 The 2D area detector image of the precursor film deposited on P. The arc at 2θ = 30.7°, corresponding to Sn, has a non-uniform intensity distribution along the entire arc, indicating slight texturing. The arc at 43° corresponds to reflections from elemental Cu and Zn phases as well as some contribution from the $Cu_{6.26}Sn_5$ phase.

Sulfidation at 100 °C

At 100 °C, sulfur incorporation into the film is below the detection limit of EDS. Thus, "sulfidation" at this temperature is no more than a mild annealing treatment of the precursor film. The morphology is still relatively uniform (Figure 2.3 (b)), though we observe small amounts of uniformly distributed insulating nanocrystals (~ 100 nm in

diameter) over the surface of the film. The appearance of these small insulating features on the surface of the film is not unique to a single substrate: all substrates yield this morphological feature in similar sizes and amounts. These nanocrystals grow larger at T_s = 200 ^{o}C and we believe that they are ZnS (*vide infra*). The formation of ZnS at such a low temperatures and S pressure is not entirely unexpected. The Gibbs free energy of ZnS is negative, even at room temperature, and ZnS formation requires much lower S pressure compared to Cu_2S or SnS.[33]

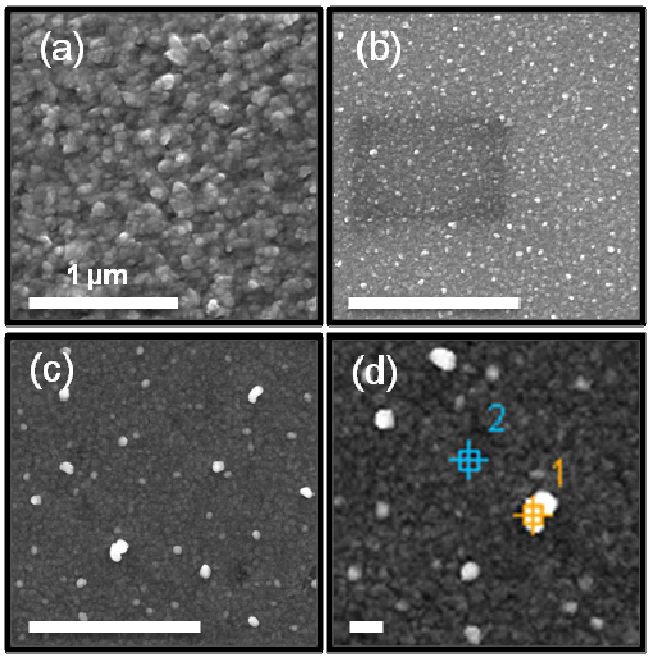

Figure 2.3 Plan view SEM images of the Cu-Zn-Sn films deposited on SLG (a) before sulfidation and after sulfidation at (b) 100 ^{o}C and (c) at 200 ^{o}C. Panel (d) shows an expanded view of the SLG film sulfidized at 200 ^{o}C. Sulfur concentrations measured by EDS at points 1 and 2 are 13 at.% and 4 at.% respectively. The SEM images of films sulfidized on FQ, Q, SP, and P are similar. All scale bars are 1 µm.

XRD after sulfidation at 100 ^{o}C shows that Cu_5Zn_8 has formed (2θ = 37.9^{o} and 48.1^{o}), and the amount of $Cu_{6.26}Sn_5$ has increased (*i.e.* the integrated area of the diffraction at 30.1^{o} has increased). However, β-Sn, and the textured FCC Cu, and HCP

Zn phases still remain. The presence of the Cu_5Zn_8 has been reported previously,[29] though the precursor film in that case was Zn rich.

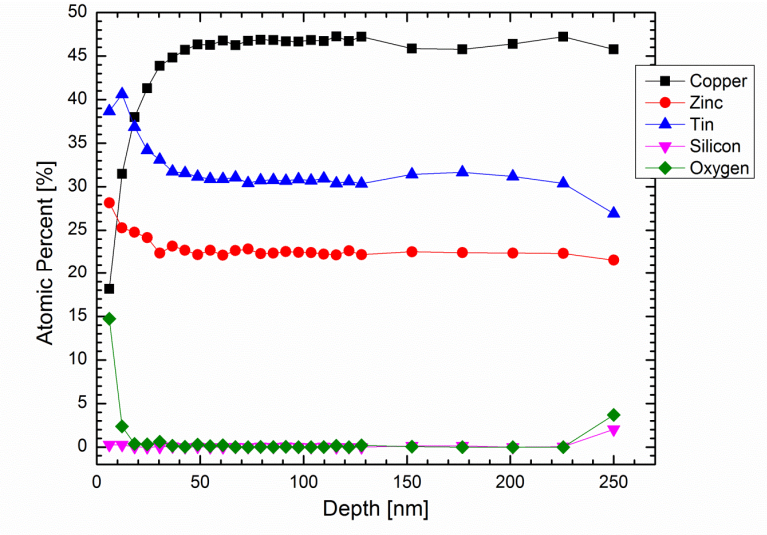

Figure 2.4 The elemental (Cu, Zn, Sn, O and Si) composition of the precursor film as a function of depth as measured by Auger electron spectroscopy. Si and O originate from the substrate. The origin (depth=0) corresponds to the surface. The film thickness was 250 nm.

Sulfidation at 200 ^{o}C

Following sulfidation at 200 ^{o}C, even more alloying of Cu with Zn and Sn is observed, on both SLG and FQ substrates; Cu_5Zn_8 and $Cu_{6.26}Sn_5$ diffraction intensities increase while the β-Sn diffraction intensity decreases. A weak diffraction line at $2\theta = 28^{o}$ may indicate ZnS formation, though Raman scattering was too weak to confirm this. EDS measurements show that only 4% and 8% S is incorporated into films on SLG and on FQ, respectively. Sulfur incorporation into films on SP, Q and P is similar. The evenly distributed insulating nanocrystals observed after sulfidation at 100 ^{o}C are larger (~250 nm) after sulfidation at 200 ^{o}C (Figure 2.3(c) and 2.3(d)). EDS measurements indicate that these nanocrystals contain more sulfur (~13%) than the rest of the film (~4%), though the EDS spot size is too wide to determine the precise cation composition of the nanocrystals. These insulating nanocrystals have the same appearance as larger,

insulating ZnS regions observed on other zinc-rich films. Their appearance and the presence of a weak XRD peak at $2\theta = 28^{o}$ suggests that these nanocrystals may indeed be ZnS. If this is the case, ZnS formation takes place at a notably lower temperature than reported by Fairbrother *et al.*[29] (400 °C) and by Schurr *et al.*,[28] (370 °C), although the S in our method has significantly more time to diffuse into the film than in these other studies.

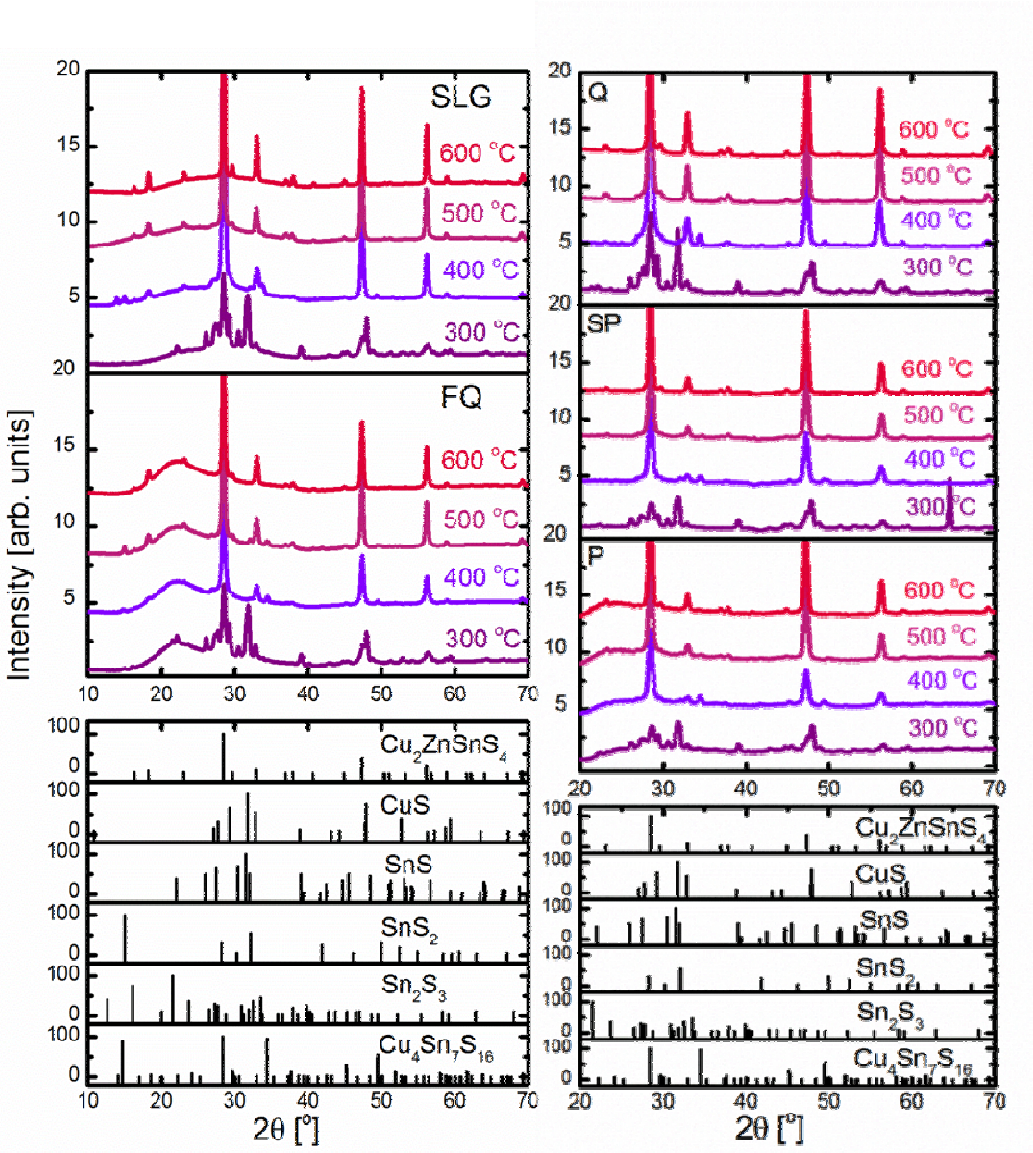

Figure 2.5 X-ray diffraction from films on all substrates after sulfidation at various temperatures between 300 °C and 600 °C. The bottom panels show the expected powder diffraction patterns from CZTS, CuS, SnS, SnS_2, and $Cu_4Sn_7S_{16}$ for comparison.

Sulfidation 300 ^{o}C

Remarkably different, at 300 ^{o}C, the films are completely sulfidized, that is 50 % of the film is now S, regardless of the substrate. All X-ray diffraction peaks from the metallic phases disappear (Figure 2.5). The cation composition of the film is different than that of the precursor film. This change is mostly due to sulfidation: as sulfur is incorporated into the film, atomic percent of the cations decrease. For films sulfidized at 400 ^{o}C-600 ^{o}C, the deviation in the cation composition from the nominal stoichiometry of CZTS (25% Cu, 12.5% Zn, 12,5% Sn) falls within the standard deviation of our measurements. (See Table 2.2 and discussion below.) For the film sulfidized at 300 ^{o}C, the deviation in the atomic percentage of Zn from the expected CZTS stoichiometry is reproducible and can be understood by considering the vapor pressures of Zn and SnS. When the precursor film is undergoing sulfidation at 300 ^{o}C, unsulfidized Zn and SnS can leave the film because their vapor pressures are high. Zinc metal can eventually sulfidize and deposit elsewhere in the ampoule and SnS vapor condenses when the ampoule is cooled. Since the area of the ampoule walls is much greater than the film, the walls act as a sink for Zn and Sn. As the sulfidation temperature increases and sulfur is incorporated into the film, the copper atomic percent decreases from 50% to 25%, the expected value for stoichiometric CZTS. At 300 ^{o}C, the copper atomic percent is higher than 25% because some Zn and SnS have been lost from the film. There is more Zn lost from films on SLG than from films on other substrates. This higher Zn loss from films on SLG, compared to other substrates, is reproducible though the reason is unknown.

XRD data confirms the formation of SnS as well as CuS. The overlapping common diffraction lines for CZTS, Cu_2SnS_3 and ZnS appear in both films, on SLG and on FQ (Figure 2.5).[24,38] Because these diffraction lines overlap, we refer to them collectively as $\sum$CZTS/Cu_2SnS_3/ZnS.[31]

The XRD from films on Q, SP, and P (Figure 2.5) likewise show the presence of SnS, CuS and the $\sum$CZTS/Cu_2SnS_3/ZnS diffractions. In addition, the film on Q also has diffractions from Sn_2S_3 and the ternary phase $Cu_4Sn_7S_{16}$.

Raman spectra of the films sulfidized on SLG and FQ at 300 ^{o}C (Figure 2.6) shows the presence of very weak scattering from CZTS (335 cm^{-1}).[39,40] The broad Raman scattering between 250 cm^{-1} and 370 cm^{-1} is consistent with contributions from Cu_2SnS_3 (291 and 354 cm^{-1}),[41] ZnS (351 cm^{-1}),[42] and SnS_2 (315 cm^{-1}).[43] In addition, very strong scattering at 474 cm^{-1} is a clear indication of the presence of $Cu_{2-x}S$ on all substrates.[44] The films on Q, SP, and P exhibit Raman spectra similar to the films on SLG and FQ. A confocal Raman microscope was used to sample multiple locations from each film and Figure 2.6 shows two spectra for each sulfidation temperature. The spectra and the locations were chosen to demonstrate the presence of all the observed phases, regardless of the frequency of observation. The Raman spectra show that CZTS begins to form at temperatures as low as 300 ^{o}C. We find that CZTS formation starts at lower temperatures than reported elsewhere and we attribute this difference to the higher S pressures and longer sulfidation times in our experiments.[28,29] The presence of CZTS together with binary sulfides suggests that CZTS formation is thermodynamically favored at 300 ^{o}C but is likely limited by solid state diffusion. In fact, pseudo-binary and ternary phase diagrams of the Cu-Zn-Sn-S system show CZTS is a stable phase at temperatures as low as ~330 ^{o}C.[45] This is also consistent with the ability to form CZTS nanocrystals using solvothermal approaches at temperatures as low as 170-220 ^{o}C.[12-18]

Sulfidation at 400 ^{o}C

After sulfidation at 400 ^{o}C, the film's elemental composition is approximately that of CZTS (Table 2.2). Two XRD peaks unique to CZTS (2θ = 36.97 and 37.90^{o}) are now detectable (Figure 2.5) and indicate increased crystallinity (*i.e.* higher intensity XRD for similar film thickness) and a larger fraction of CZTS in films on SLG and FQ. Diffraction from SnS_2 appears as a small peak at 2θ = 15.0^{o} in films on SLG, FQ, SP and P (Figure 2.5).

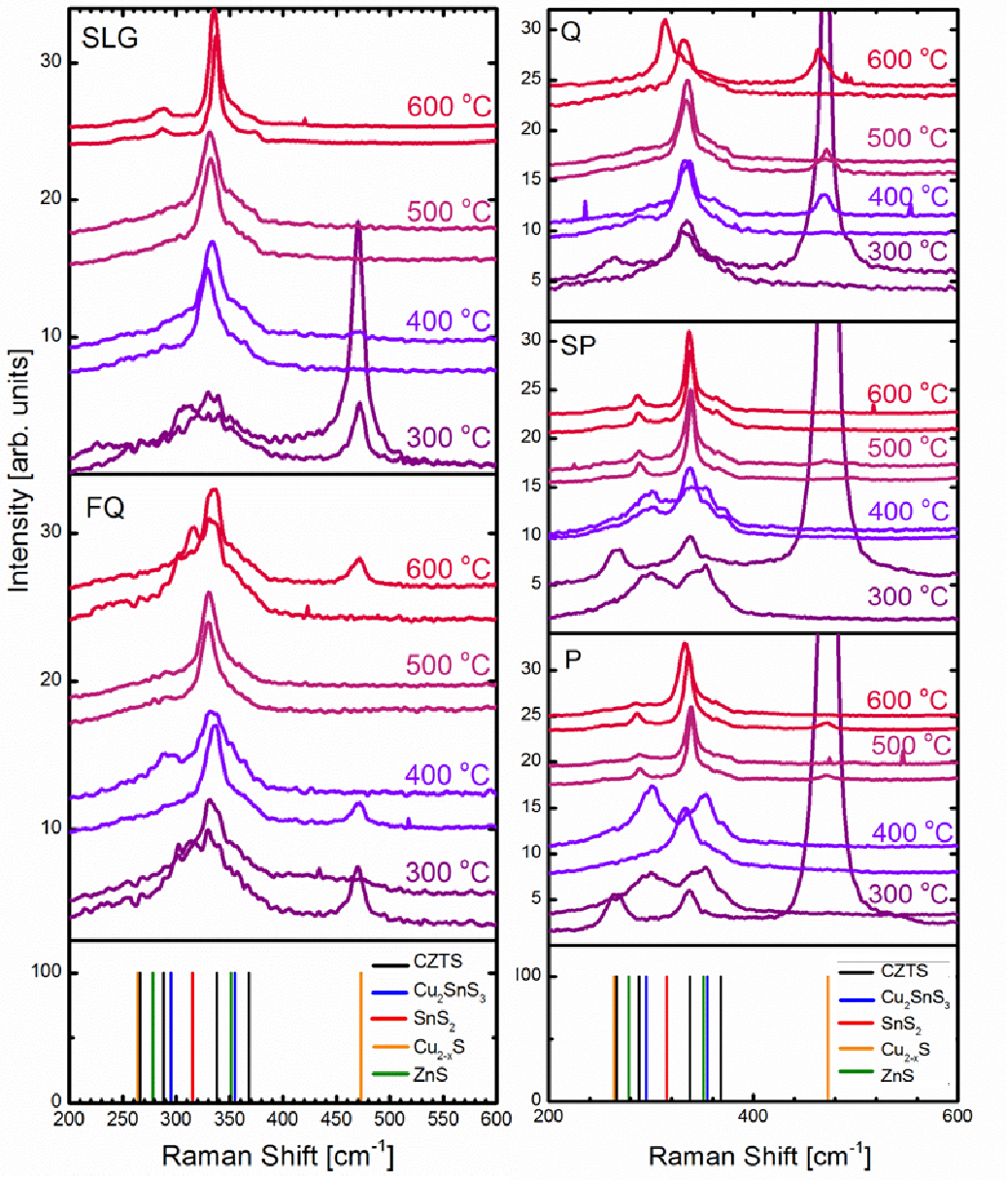

Figure 2.6 Raman spectra from films on SLG and on FQ after sulfidation at various temperatures between 300 °C and 600 °C. Individual spectra at each temperature correspond to a different area of the film. The bottom panels show the Raman scattering peaks expected from CZTS, cubic Cu_2SnS_3, SnS_2, $Cu_{2-x}S$, and ZnS for comparison.

In films on SLG, small amounts of an unidentified phase appear as weak diffractions near $2\theta = 33.8^{o}$ and 49.3^{o}, the same values reported, but also unidentified, by Platzer-

Björkman *et al.*[34] These are much weaker than the ∑CZTS/Cu_2SnS_3/ZnS and SnS_2 diffractions, suggesting that they originate from a phase present in very small amounts. In films on FQ, we also detected $Cu_4Sn_7S_{16}$ by XRD (Figure 2.5). In fact, films on all substrates other than SLG were found to contain $Cu_4Sn_7S_{16}$ by XRD.

Strong Raman scattering at 336 cm^{-1} confirms that both films, on SLG and on FQ, contain significant amounts of CZTS. A pronounced shoulder on the CZTS peak near 350 cm^{-1} indicates the presence of ZnS so that at least some fraction of the ∑CZTS/Cu_2SnS_3/ZnS diffraction is attributed to ZnS. In films sulfidized on FQ we still detect Raman scattering from $Cu_{2-x}S$ indicating that a small amount, not detectable by XRD, is present. We do not detect any other Raman peaks that can be attributed either to the unidentified impurity phase or to $Cu_4Sn_7S_{16}$. The Raman spectra collected from the film on Q are very similar to those from SLG and FQ, however the films on SP and P still show the presence of Cu_2SnS_3. (Figure 2.6).

Sulfidation at 500 ^oC

The films sulfidized at 500 ^oC, on SLG and on FQ, have nearly identical elemental composition (Table 2.2). However, there are significant differences in their phase compositions. Specifically, the films sulfidized on SLG now predominately show the ∑CZTS/Cu_2SnS_3/ZnS diffraction; the unidentified phase has nearly disappeared (Figure 2.5). In contrast, we still detect SnS_2 and $Cu_4Sn_7S_{16}$ in films on FQ (Figure 2.5). Like the film on FQ, the films on SP and P also show diffractions from $Cu_4Sn_7S_{16}$ and SnS_2, while the film on Q shows only the ∑CZTS/Cu_2SnS_3/ZnS diffraction (Figure 2.5).

On both SLG and FQ, the normalized XRD intensities from CZTS are larger and the widths of the Raman scattering peaks at ~336 cm^{-1} are narrower than those from films sulfidized at 400 ^oC, indicating a further increase in CZTS crystallinity. The full width at half maximum of the ~336 cm^{-1} Raman peak from films on SLG decreases from 20.4 cm^{-1} at 400 ^oC, to 9.4 cm^{-1} at 500 ^oC. However, Raman scattering from both the SLG and FQ films still show the presence of a shoulder at 351 cm^{-1}, adjacent to the 336 cm^{-1} CZTS peak. Deconvolution and quantitative analysis of the Raman spectra using the approach

described by Khare *et al.*[46] (Figure 2.7) shows that the shoulder at 351 cm^{-1} is stronger in films sulfidized at 500 ^{o}C than that found in phase-pure CZTS films. For the nominally phase-pure CZTS film, the ratio of the area under the peak at 351 cm^{-1} to the area under the strongest CZTS peak at 332-337 cm^{-1} is 0.045. This ratio is 0.13, significantly higher, for the film sulfidized at 500 ^{o}C on SLG. The stronger scattering at 351 cm^{-1} is indicative of the presence of ZnS. This comparison suggests the presence of some ZnS in films sulfidized at 500 ^{o}C. The films on Q, SP, and P show a similar decrease in width of the 336 cm^{-1} CZTS peak from 400^{o}C to 500^{o}C, though there is still evidence of Raman scattering from ZnS and $Cu_{2-x}S$ in some small regions of the film (Figure 2.6).

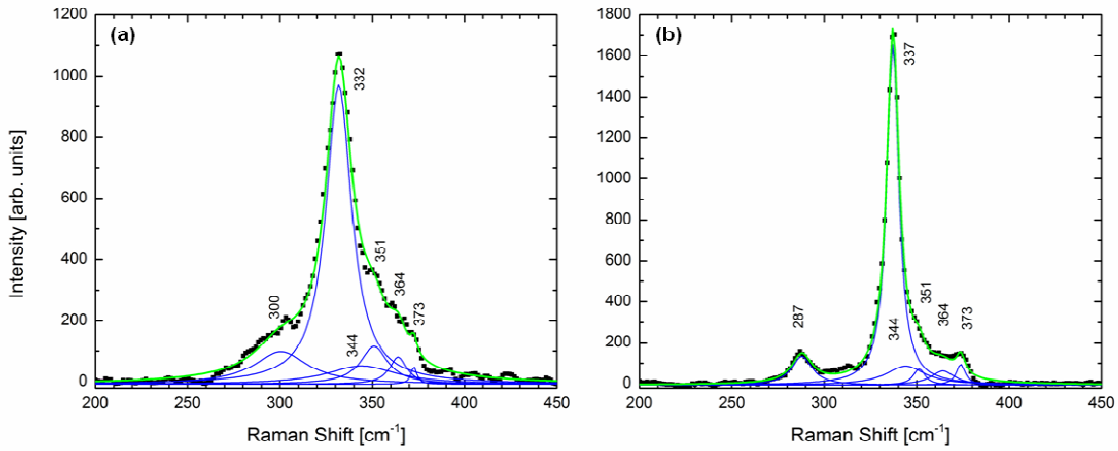

Figure 2.7 Raman spectra (a) from the film sulfidized at 500 ^{o}C on SLG and (b) from a nominally phase-pure CZTS film. Raman scattering between 250-380 cm^{-1} was deconvoluted using six peaks with Lorentzian lineshapes.

Sulfidation at 600 ^{o}C

Within the accuracy of EDS, the elemental compositions of the films sulfidized at 600 ^{o}C are essentially the same as the films sulfidized at 400 ^{o}C and 500 ^{o}C (Table 2.2). The XRD and Raman spectra from films on SLG are consistent with crystalline, phase-pure CZTS (Figs. 2.5 and 2.6). While the XRD from the film on FQ also suggests phase-pure CZTS, Raman scattering shows small regions of SnS_2, ZnS, and $Cu_{2-x}S$ (Figure 2.6).

Nevertheless, the majority of the Raman spectra collected from different areas of the film on FQ show a sharp 336 cm^{-1} peak, consistent with a film that is mostly CZTS. In contrast, despite a diligent search, we could not find any regions of impurity phases in films on SLG by Raman imaging. The film sulfidized on Q has a phase composition similar to the film on FQ in that XRD suggests phase-pure CZTS, while Raman reveals small regions of SnS_2, ZnS and $Cu_{2-x}S$ (Figure 2.6). The films on SP, like the film on SLG, are nominally phase-pure CZTS. The film on P is almost all CZTS but infrequent regions of $Cu_{2-x}S$ were encountered while imaging with Raman spectroscopy.

2.3.2 Sulfidation Temperature Dependence of the Films' Phase Composition

We quantified the films' phase composition using the following approach. For each phase, a unique X-ray diffraction peak was selected (Table 2.3) and its integrated intensity was normalized by the detector exposure time, the film thickness and the corresponding powder diffraction intensity relative to the strongest peak. The fraction of each phase is calculated by dividing this normalized intensity, I_j, with the sum of all the phases present in the film (ΣI_j). This approach should provide a reasonable representation of the films' phase composition provided that the films are not heavily textured. As discussed earlier, the Cu and Zn phases in the precursor films and the films sulfidized at 100 ^oC are heavily textured. For these films, the relative intensities of the (111) and (101) reflections of Cu and Zn near 43-44^o are significantly greater than those expected from their respective powder diffraction patterns. For this reason the elemental Cu and Zn phases have been omitted from the phase composition analysis for the precursor films and the films sulfidized at 100 ^oC, as they would make up in excess of 80% of the bar representing these films, even though (based on stoichiometry) they make up less than 80% of the film. The relative phase compositions of these films are still useful to consider, however, as they clearly show the change in alloying in these films.

Table 2.3 The unique diffraction planes used for quantifying the phase composition of the films. These diffraction peak intensities were used to construct Figure 2.8.

Phase	2θ [°]	(hkl)	Relative Intensity [arb. units]
Sn (PDF # 00-004-0673)	32.019	(101)	90
$Cu_{6.26}Sn_5$ (PDF # 00-047-1575)	30.126	(101)	100
Cu_5Zn8 (PDF # 00-025-1228)	37.967	(321)	5
CuS (PDF # 00-006-0464)	31.785	(103)	100
SnS (PDF # 00-039-0354)	26.010	(120)	50
$Cu_4Sn_7S_{16}$ (PDF # 01-089-4713)	34.414	(208)	95
SnS_2 (PDF #00-023-0677)	15.029	(001)	100
Sn_2S_3 (PDF #00-014-0619)	21.499	(130)	100
Cu_2ZnSnS_4/Cu_2SnS_3/ZnS (PDF# 04-005-0388/01-089-2877/00-005-0566)	28.441/28.447/ 28.559	(112)/(111) /(111)	100/100/100

The results of this analysis for SLG and FQ substrates are displayed as bar graphs in Figure 2.8, providing a visual summary and representation of the evolution of the films phase composition with sulfidation temperature. Only the phases present in amounts high enough to be detected by XRD are included in the bar graphs. Additional phases could be detected through confocal Raman microscopy. These minority phases are listed above the bar for each temperature. Films deposited on FQ and SLG exhibit nearly identical phase composition evolution from 100 °C to 300 °C.

We do not detect any significant sulfidation at 100 and 200 °C but both Cu_5Zn_8 and $Cu_{6.26}Sn_5$ fractions increase when the precursor films are heated to 100 and 200 °C. By 200 °C nearly all of the elemental Sn is alloyed. The incorporation of S starts between 200 and 300 °C. After Sulfidation at 300 °C, each film is comprised of binary and ternary sulfides, and CZTS. Since there is no Cu and Zn containing ternary, formation and segregation of ZnS and CuS from the Cu_5Zn_8 alloy is not surprising. Formation of Cu_2SnS_3 from sulfidation of the $Cu_{6.26}Sn_5$ alloy can also be expected.

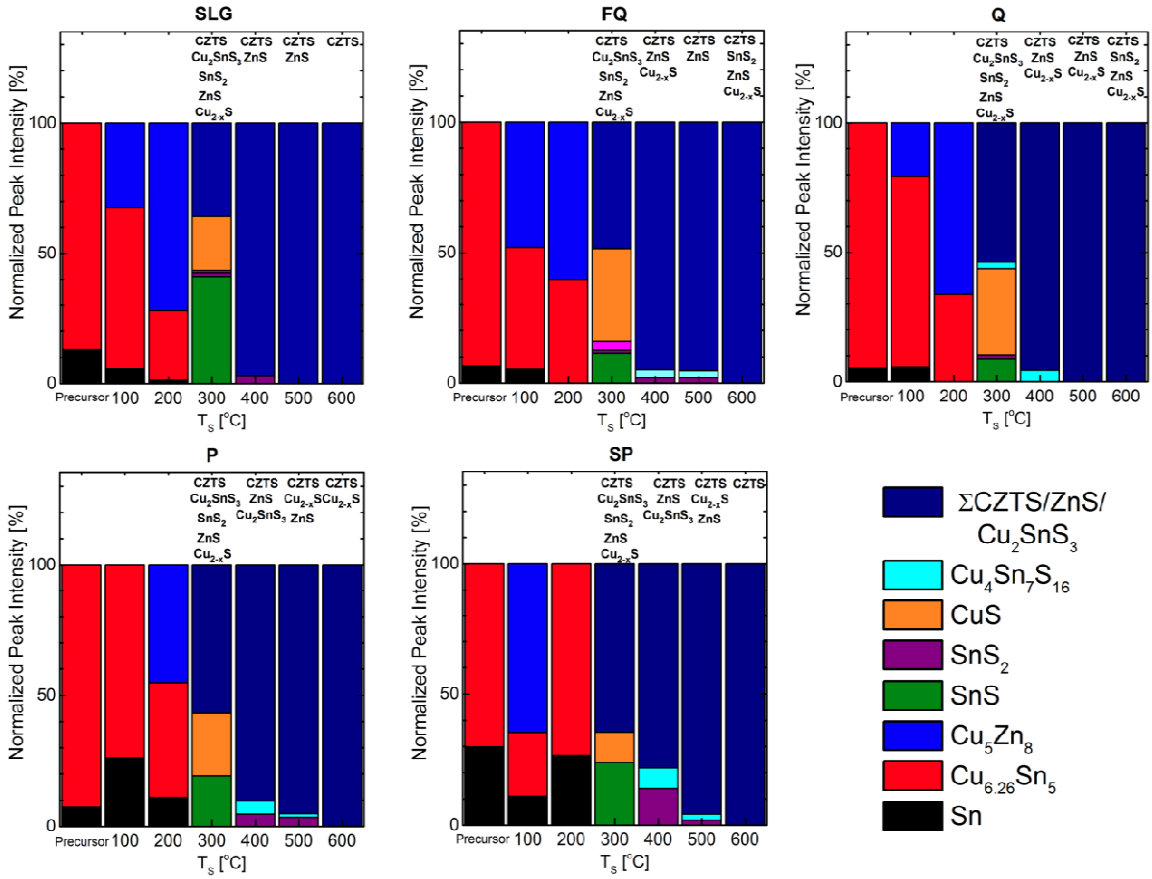

Figure 2.8 The evolution of the phase composition of films on SLG, FQ, Q, P and SP as a function of the sulfidation temperature. The heights of the colored bars represent the fraction of the phases present in the film. See text and Table 2.3 for calculation details. Textured Cu and Zn phases are omitted from the phase composition of the precursor and the film sulfidized at T_S=100 °C. Phases listed above each bar are those identified by Raman spectroscopy.

While the phase composition of the films on SLG and FQ are similar up to T_S=300°C, they start to differ when $T_S \geq$400°C. The films sulfidized on SLG are nearly phase pure by 400 °C with only very small amounts of ZnS and SnS_2 remaining, along with a small, albeit unquantifiable, amount of a currently unidentified phase. These results are similar to those by Han *et al*. who claimed to have achieved phase-pure CZTS by annealing films, sputtered from Cu, ZnS and SnS_2 targets on Mo-coated SLG, in H_2S for one hour at 400 °C.[30] In most other sulfidation studies, however, conversion to CZTS is not achieved until after T_S exceeds 480 °C.[28,29] The small amounts of ZnS and SnS_2

remaining at 400 and 500 ^{o}C appears to be consistent with Thimsen *et al.* who hypothesized that Zn diffusion into SnS_2 and Sn diffusion into ZnS are slow and are the rate limiting steps in forming CZTS from binary metal sulfides.[47] At 600 ^{o}C, CZTS formation on SLG is complete after 8 hours of sulfidation.

In contrast to films sulfidized on SLG, we find significant (*i.e.* detectable by XRD) amounts of $Cu_4Sn_7S_{16}$, and SnS_2 in films sulfidized on FQ at 400 and 500 ^{o}C. On FQ, nearly complete conversion to CZTS requires temperatures as high as 600^{o}C. Even then, impurity phases persist and we still find SnS_2, ZnS and CuS inclusions in the film with confocal Raman spectroscopy.

Films sulfidized on P and SP exhibit a nearly identical phase composition evolution to films sulfidized on FQ, though the films are nominally phase pure at T_s= 600 ^{o}C. The films on Q undergo a nearly identical phase evolution to FQ. The films on Q also contain $Cu_4Sn_7S_{16}$, and, like the film on FQ, still contain impurity phases even when sulfidized at 600 ^{o}C. Although the $Cu_4Sn_7S_{16}$ phase has been reported in films synthesized from a Sn-rich precursor,[48] we have never observed this phase when sulfidizing Sn-rich films on SLG. This suggests that the presence of this phase is not necessarily correlated with high Sn concentrations in the precursor films.

It may be surprising that, even though the films are slightly copper rich, we do not observe significant amounts of copper sulfide. The commonly hypothesized reaction pathway that forms CZTS from a Cu-Zn-Sn alloy film begins with the formation of binary sulfides, ZnS, $Cu_{2-x}S$, and Sn_xS_y, followed by a reaction to form Cu_2SnS_3 which later interdiffuses with ZnS to form CZTS. (Cu_2SnS_3 and ZnS have the same sulfur sublattice so that this interdiffusion can be thought of mixing of the cations.) If the film is Cu rich such that Cu/Sn > 2, we certainly expect copper sulfide domains to be present in the CZTS film. However, if Cu/Sn $\leq$ 2, as is the case in our precursor films, copper sulfides are converted to Cu_2SnS_3. In fact, at temperatures 400 ^{o}C and higher, the copper sulfide content falls below the detection limits of XRD, is not visible by SEM/EDS, and is found only by diligent examination with Raman microscopy in only some of the films. Based on this, it follows that a film with a Cu/Zn ratio greater than 2 does not necessarily

have to form copper sulfide if sufficient amounts of Sn are also present to form Cu_2SnS_3. The lack of large domains of copper sulfide at elevated temperatures also demonstrates that the limiting process in CZTS formation in our sulfidation scheme is in fact ZnS intermixing with Cu_2SnS_3 and not the conversion of copper and tin sulfides.

Figure 2.8 reveals that conversion of binary and ternary sulfides to CZTS is more facile on SLG than on any of the other substrates used in this study: the films on SLG are converted nearly completely to CZTS at lower sulfidation temperatures than films on other substrates. Moreover, the $Cu_4Sn_7S_{16}$ phase is not even observed when the films are sulfidized on SLG. The obvious difference between SLG and the other substrates is the impurities in SLG (Table 2.2). Amongst all the substrates used in this study, only SLG and P contain intentionally added impurities. Moreover, SLG has more than thrice the Na concentration of P. As we will now discuss, comparison of the microstructures of the films synthesized on different substrates reinforces the observation that sulfidation and CZTS crystal growth is more facile on SLG.

2.3.3 Microstructure

Figure 2.9 shows low magnification plan view SEM micrographs of films sulfidized on all substrates at temperatures between 300 ^oC and 600 ^oC. The surface morphologies of the films sulfidized on all substrates appear similar up to T_s=500 ^oC. On all substrates, the surface morphology of the films sulfidized at 300 ^oC is inhomogeneous and exhibit several distinct features, each characteristic of the phases identified through Raman spectroscopy and XRD. Indeed, the elemental compositions of these features match one of ZnS, CuS, SnS_2, or Cu_2SnS_3. Utilizing EDS point-and-shoot mode, we find that the morphological features circled in Figure 2.9 (a), (e), (i), (m), and (q), for example, correspond to CuS (red), ZnS (green), and Cu_2SnS_3 (blue). Clearly, as the metal alloys are sulfidized, binary and ternary sulfides form and segregate. The inhomogeneous morphology is consistent with the observation of multiple sulfides with XRD and Raman spectroscopy.

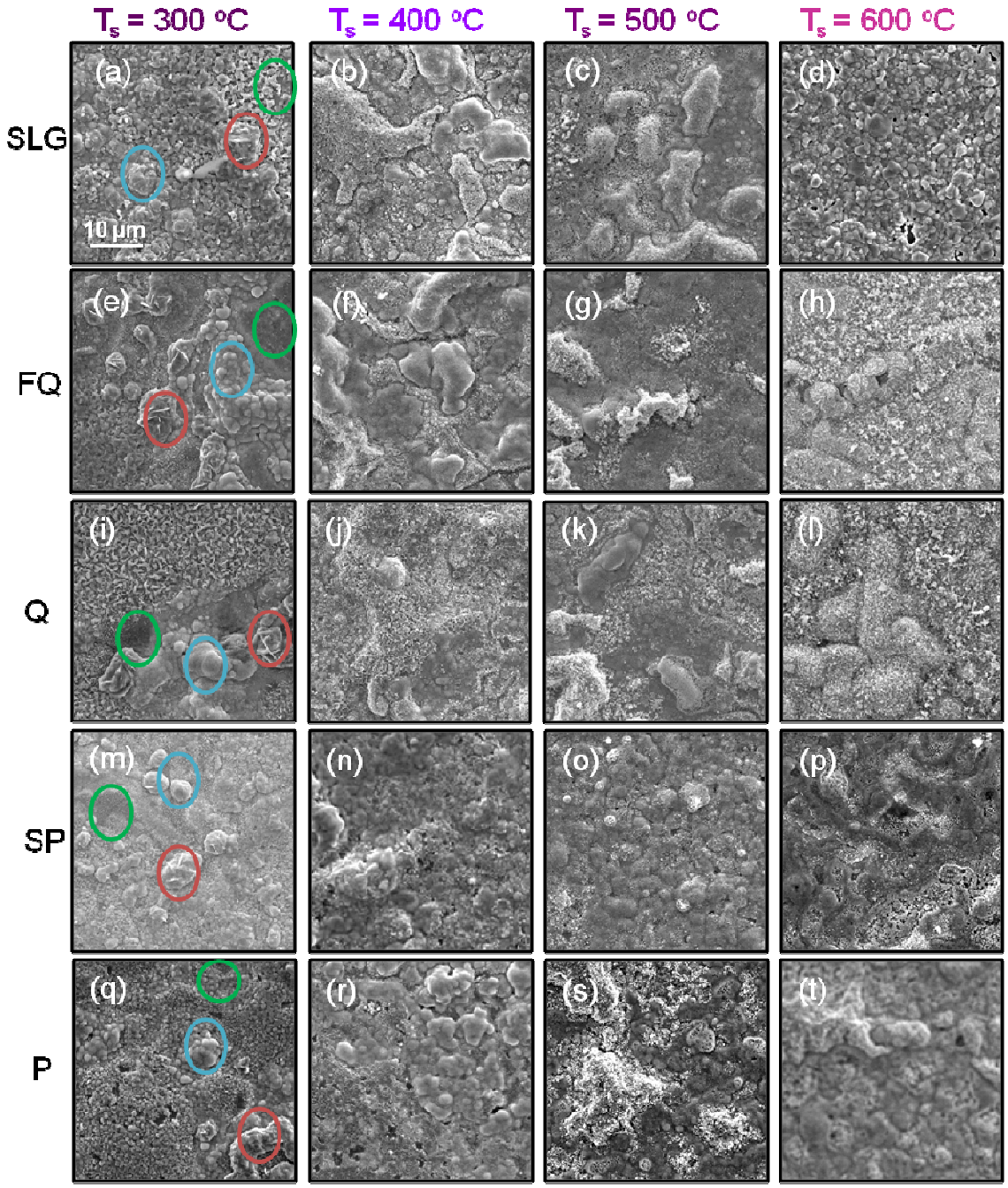

Figure 2.9 Plan view SEM images of the films deposited on SLG (a-d), FQ (e-h), Q (i-l), SP (m-p) and P (q-t) after sulfidation at various temperatures between 300 °C and 600 °C. The scale bar applies to all images. Colored circles are referred to in the text.

As the sulfidation temperature is increased to 400 and to 500 ^{o}C, CZTS grows at the expense of the binary and ternary sulfides (Figure 2.8), the elemental composition across the film surface and morphology becomes more homogeneous. On films sulfidized at 400 ^{o}C and at 500 ^{o}C there is no obvious correlation between morphological features and composition, even though small amounts of impurity phases (*e.g.*, ZnS, SnS_2 and $Cu_4Sn_7S_{16}$, see Figure 2.8) can be detected by both Raman spectroscopy and XRD. While the surface morphology appears increasingly more uniform with increasing T_s, the surface of the films on both SLG and FQ have a rather nondescript microstructure with no obvious grain structure. Cross sectional SEM images of these two films at T_s = 500 ^{o}C reveal a better-defined grain structure (Figure 2.10). The average grain sizes measured from cross sectional images were 260 ± 50 nm for the film on SLG and 160 ± 30 nm for the film on FQ. Recognizable surface grains emerge only when the sulfidation temperature is raised above 500 ^{o}C (Figs. 2.9 and 2.11). Remarkably, the microstructures and the grain sizes of the films sulfidized on FQ and the films sulfidized on SLG are significantly different when the sulfidation is at 600 ^{o}C. The morphologies and grain sizes of the films grown on FQ show little change between 500 and 600 ^{o}C (170 nm ± 40 nm at 600 ^{o}C). In contrast, the film on SLG is remarkably uniform across the surface, with clearly distinguishable grains averaging 970 ± 160 nm in size.

Figure 2.11 compares the plan and cross sectional views of films sulfidized on SLG, FQ, Q, SP, and P at 600 ^{o}C. In plan view, films synthesized on all substrates, except SLG, exhibit a similar fine-grained surface morphology. Even though grains are not apparent in the plan view of the films on Q, FQ, SP and P, the cross sectional SEM image reveals grains in addition to a bilayer structure where grains appear to be larger in the layer near the substrate than the layer at the top of the film. This bilayer structure is also present in the film on SLG sulfidized at 500 ^{o}C, but it is not observed if the sulfidation is conducted at 600 ^{o}C. This observation hints that the formation of the bilayer structure may be due to stress buildup in the film during CZTS formation and grain growth. SLG is the only substrate in this study to soften by 600 ^{o}C, so that stresses that develop in the film may relax on SLG, which becomes compliant at 600 ^{o}C.

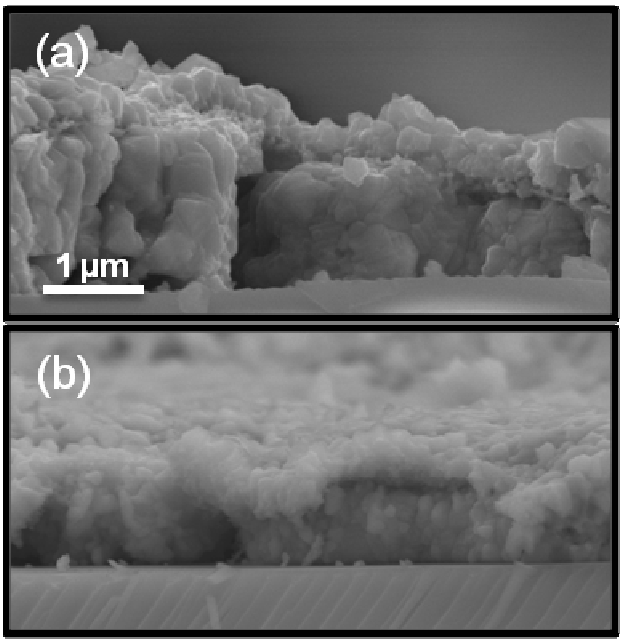

Figure 2.10 Cross-sectional SEM images of the samples sulfidized on (a) SLG and (b) FQ (b) at 500 °C.

One likely explanation for the vastly improved morphology of CZTS and larger grain sizes on SLG compared to other substrates is impurity diffusion from the SLG into the CZTS layer. Recently, Hliang Oo *et al.* showed that addition of Na_2S to the film prior to sulfidation drastically improved the grain size.[35] Recently we published a systematic study demonstrating the effects of various impurity atoms in SLG on CZTS morphology. In that study enhanced grain growth on SLG substrates was found to be due to Na and K, while others such as Ca, Mg, B and Al were ruled out.[36] It is interesting to relate our observations to those by Nagaoka *et al.* who detected a shift in the (112) x-ray diffraction peak of CZTS single crystals and suggested that Na substitutes into the cation sites, expanding the CZTS unit cell. Such an expansion may facilitate grain growth by enhancing diffusion.[49] In addition to its profound effect on the microstructure, Na also affects the electrical properties of CZTS.[49]

Curiously, Pyrex also contains significant levels of Na and K (though less than SLG), yet its grain size is significantly smaller than SLG. Using time of flight secondary

ion mass spectroscopy we find significant amounts of the aforementioned impurities in films on SLG and on P but not in Q. A detailed quantitative investigation of the subtle differences in impurity concentrations in these films is reported elsewhere.[36]

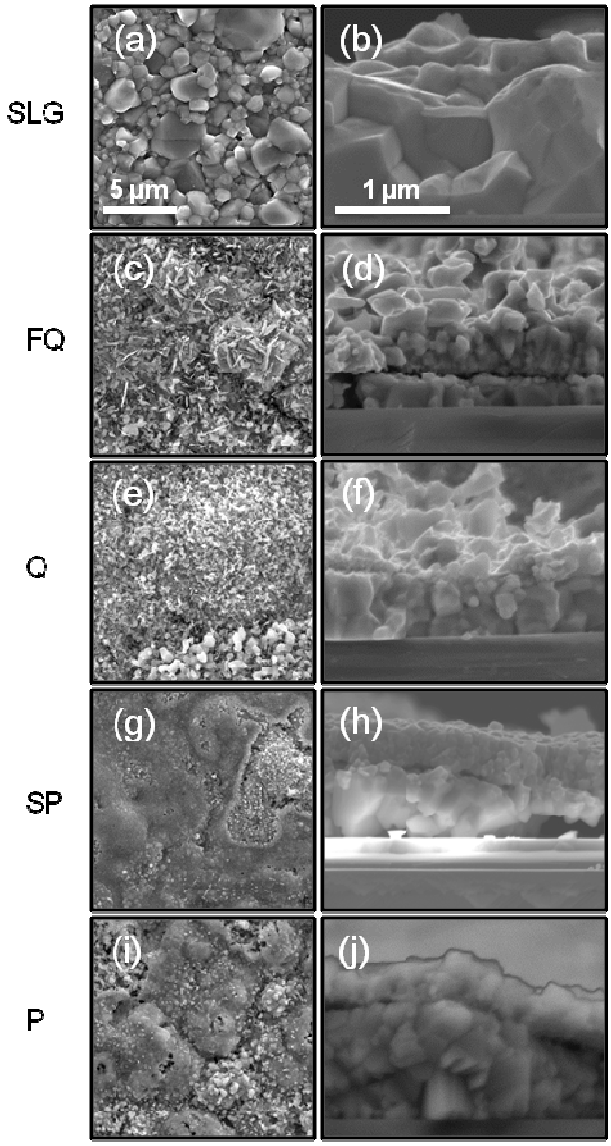

Figure 2.11 High magnification plan view (a,c,e,g,i) and cross sectional (b,d,f,h,j) SEM images of films sulfidized at 600 oC on SLG (a, b), on FQ (c, d), on Q (e, f), on SP (g, h), and on P (i, j). Same scale bar applies for all images.

2.4 Conclusions

In summary, thin CZTS films were synthesized by sulfidizing co-sputtered Cu-Zn-Sn films deposited on crystalline quartz, fused quartz, sapphire, Pyrex, and soda lime glass substrates in an isothermal closed system between 100 and 600 ^{o}C for 8 hours. On all substrates, CZTS formation proceeds through sulfidation of Cu, Zn, and Sn metals and Cu_5Zn_8 and $Cu_{6.26}Sn_5$ alloys, which form during sputtering and heating to 200 ^{o}C. Sulfidation begins between 200 ^{o}C and 300 ^{o}C on all substrates.

By 300 ^{o}C the precursor films are completely sulfidized and are composed of similar amounts of CuS, SnS, SnS_2, Sn_2S_3, ZnS, Cu_2SnS_3 and CZTS. Significant differences in phase composition begin to emerge at 400 ^{o}C. Films grown on SLG are nearly all CZTS by 400 ^{o}C, though some small amounts of ZnS, SnS_2, and an unidentified phase are detected. Films deposited on all other substrates persistently contained significant amounts of impurity phases such as $Cu_4Sn_7S_{16}$ until the sulfidation temperature is increased to 600 ^{o}C. Upon sulfidation at 600 ^{o}C the film on SLG has significantly larger grain size than the films on all other substrates. Thus, sulfidation and grain growth on SLG is accelerated compared to other substrates. This acceleration, and the large grained microstructure on SLG, are attributed to impurity diffusion from the SLG substrate into the CZTS films, though further study is needed to determine exactly which impurity atom(s) is responsible, and to better understand the mechanism behind impurity-assisted grain growth.

2.5 References

1. D. B. Mitzi, O. Gunawan, T. K. Todorov, K. Wang and S. Guha, Sol. Energ. Mat. Sol. C. **95**, 1421 (2011).
2. H. Katagiri, N. Sasaguchi, S. Hando, S. Hoshino, J. Ohashi and T. Yokota, Sol. Energ. Mat. Sol. C. **49**, 407 (1997).
3. H. Katagiri, Thin Solid Films **480-481**, 426 (2005).
4. T. Todorov, O. Gunawan, S. J. Chey, T. Goislard de Monsabert, A. Prabhakar and D. B. Mitzi, Thin Solid Films **519**, 7378 (2011).

5. N. Vora, J. Blackburn, I. repins, C. Beall, B. To, J. Pankow, G. Teeter, M. Young and R. Noufi, J. Vac. Sci. Technol. A **30**, 051201 (2012).
6. C. A. Wolden, J. Kurtin, J. B. Baxter, I. Repins, S. E. Shaheen, J. T. Torvik, A. A. Rockett, V. M. Fthenakis and E. S. Aydil, J. Vac. Sci. Technol. A **29**, 030801 (2011).
7. K. Ito and T. Nakazawa, Jpn. J. Appl. Phys. **27**, 2094 (1988).
8. N. Nakayama and K. Ito, Appl. Surf. Sci. **92**, 171 (1996).
9. M. T. Winkler, W. Wang, O. Gunawan, H. Hovel, T. Todorov and D. B. Mitzi, Energ. Environ. Sci. **7**, 1029 (2014).
10. B. Shin, O. Gunawan, Y. Zhu, N. A. Bojarczuk, S. J. Chey and S. Guha, S. Prog. Photovoltaics **21**, 72 (2013).
11. A. Chirilă, P. Reinhard, F. Pianezzi, P. Bloesch, A. R. Uhl, C. Fella, L. Kranz, D. Keller, C. Gretener, H. Hagendorfer, D. Jaeger, R. Erni, S. Nishiwaki, S. Buecheler and A. N. Tiwari, Nat. Mater. **12**, 1107 (2013).
12. Q. Guo, H. W. Hillhouse and R. Agarwal, J. Am. Chem. Soc. **131**, 11672 (2009).
13. Q. Guo, G. M. Ford, W.-C Yang, B. C. Walker, E. A. Stach, H.W. Hillhouse and R. Agrawal, J. Am. Chem. Soc. **132**, 17384 (2010).
14. C. Steinhagen, M. G. Panthani, V. Akhavan, B. Goodfellow, B. Koo and B. A. Korgel, J. Am. Chem. Soc. **131**, 12554 (2009).
15. S. C. Riha, B. A. Parkinson and A. L. Prieto, J. Am. Chem. Soc. **131**, 1254 (2009).
16. A. Khare, A. W. Wills, L. M. Ammerman, D. J. Norris and E. S. Aydil, Chem. Commun. **47**, 11721 (2011).
17. B. D. Chernomordik, A. E. Béland, D. D. Deng, L. F. Francis, and E. S. Aydil, Chem Mater. **26**, 3191 (2014).
18. B. D. Chernomordik, A. E. Béland, N. Trejo, A. Gunawan, D. D. Deng, K. A. Mkhoyan and E. S. Aydil, J. Mater. Chem. A **2,** 10389 (2014).
19. T. K. Todorov, K. B. Reuter and D. B. Mitzi, Adv. Mater. **22**, 157 (2010).

20. T. R. Knutson, P. J. Hanson, E. S. Aydil and R. L. Penn, Chem. Comm. **50**, 5902 (2014).
21. I. Repins, C. Beall, N. Vora, C. DeHart, D. Kuciauskas, P. Dippo, B. To, J. Mann, W.-C Hsu, A. Goodrich and R. Noufi, Sol. Energ. Mat. Sol. C. **101**, 154 (2012).
22. T. Ericson, J. J. Scragg, T. Kubart, T. Törndahl and C. Platzer-Björkman, Thin Solid Films **520**, 7093 (2012).
23. H. Katagiri, N. Ishigaki, T. Ishida and K. Saito, Jpn. J. Appl. Phys. **40**, 500 (2001).
24. A.-J. Cheng, M. Manno, A. Khare, C. Leighton, S. Campbell and E. S. Aydil, J. Vac. Sci. Technol. A **29**, 051203 (2011).
25. H. Katagiri, K. Jimbo, W. S. Maw, K. Oishi, M. Yamazaki, H. Araki and A. Takeuchi, Thin Solid Films **517**, 2455 (2009).
26. P. A. Fernandes, P. M. P. Salomé, A. F. da Cunha, and B.-A. Schubert, Thin Solid Films **519**, 7382 (2011).
27. J. J. Scragg, D. M. Berg and P. J. Dale, J. Electroanal. Chem. **646**, 52 (2010).
28. R. Schurr, A. Hölzing, S. Jost, R. Hock, T. Voss, J. Schulze, A. Kirbs, A. Ennaoui, M. Lux-Steiner, A. Weber, I. Kötschau and H. W. Schock, Thin Solid Films **517**, 2465 (2009).
29. A. Fairbrother, X. Fontané, V. Izquierdo-Roca, M. Espíndola-Rodríguez, S. López-Marino, M. Placidi, L. Calvo-Barrio, A. Pérez-Rodríguez and E. Saucedo, Sol. Energ. Mater. Sol. C. **112**, 97 (2013).
30. J. Han, S.W. Shin, M. G. Gang, J. H. Kim and J. Y. Lee, Nanotechnology **24**, 095706 (2013).
31. A. Weber, R. Mainz and H. W. Schock, J. Appl. Phys. **107**, 013516 (2010).
32. A. Redinger, D. M. Berg, P. J. Dale and S. Siebentritt, J. Am. Chem. Soc. **133**, 3320 (2011).
33. J. J. Scragg, T. Ericson, T. Kubart, M. Edoff and C. Platzer-Björkman, Chem. Mater. **23**, 4625 (2011).

34. C. Platzer-Björkman, J. J. Scragg, H. Flammersberger, T. Kubart and M. Edoff, Sol. Energ. Mater. Sol. C. **98**, 110 (2012).
35. W. M. Oo Hliang J. L. Johnson, A. Bhatia, E. A. Lund, M. M. Nowell and M. A. Scarpulla, J. Electron. Mater. **40**, 2214 (2011).
36. M. Johnson, S. V. Baryshev, E. Thimsen, M. Manno, I. V. Veryovkin, C. Leighton and E. S. Aydil, Energ. Environ. Sci. **7**, 1931 (2014).
37. C. M. Sutter-Fella, J. A. Stueckelberger, H. Hagendorfer, F. La Mattina, L. Kranz, S. Nishiwaki, R. Alexander, Y. E. Romanyuk and A. N. Tiwari, Chem. Mater. **26**, 1420 (2014).
38. P. A. Fernandes, P. M. P. Salomé and A. F. A. da Cunha, A. F. A. Thin Solid Films **517**, 2519 (2009).
39. H. Yoo and J. H. Kim, Thin Solid Films **518**, 6567 (2010).
40. K. Wang, O. Gunawan, T. Todorov, B. Shin, S. J. Chey, N. A. Bojarczuk, D. B. and S. Guha, Appl. Phys. Lett. **97**, 143508 (2010).
41. P. A. Fernandes, P. M. P. Salomé and A. F. A. da Cunha, J. Phys. D Appl. Phys **43**, 215403 (2010).
42. Y. C. Cheng, C. Q. Jin, F. Gao, X. L. Wu, W. Zhong, S. H. Li and P. K. Chu, J. Appl. Phys. **106**, 123505 (2009).
43. C. Wang, K. Tang, Q. Yang Y. Qian, Chem. Phys. Lett. **357**, 371 (2002).
44. C. G. Munce, G. K. Parker, S. A. Holt and G. A. Hope, G. A. Colloid Surface A. **295**, 152 (2007).
45. I. D. Olekseyuk, I. V. Dudchak, L. V. Piskach, J. Alloys Compd. **368**, 135 (2004).
46. A. Khare, B. Himmetoglu, M. Johnson, D. J. Norris, M. Cococcioni and E. S. Aydil, J. Appl. Phys. **111**, 083707 (2012).
47. E. Thimsen, S. V. Baryshev, A. B. F. Martinson, J. W. Elam, I. V. Veryovkin and M. J. Pellin, Chem. Mater. **25**, 3113 (2013).
48. J. Ge, W. Yu, H. Cao, J. Jiang, J. Ma, L. Yang, P. Yang Z. Hu and J. Chu, Phys. Status. Solidi A **209**, 1493 (2012).

49. A. Nagaoka, H. Miyake, T. Taniyama, K. Kakimoto, Y. Nose, M. A. Scarpulla and K. Yoshino, Appl. Phys. Lett. **104**, 152101 (2014).

Chapter 3

Tuning the composition of Cu2ZnSnS4 synthesized via ex situ sulfidation of co-sputtered Cu-Zn-Sn films

3.1 Introduction

The global solar-to-electric energy conversion capacity has doubled every 2.5 years between 1975 and 2013.[1] Maintaining this growth rate towards terawatt levels with current thin-film solar cells based on CdTe or $CuIn_{1-x}GaSe_2$ (CIGS) may be difficult because the abundance of indium and tellurium in earth's crust is very low.[2] Cu_2ZnSnS_4 (CZTS) and $Cu_2ZnSnSe_4$ (CZTSe) are earth abundant, low cost, and non-toxic alternatives to CdTe and CIGS and are being considered as the absorber layer in thin film solar cells.[3] These p-type semiconductors have high absorption coefficients ($>10^4$ cm^{-1} for $\lambda<1000$ nm),[4] and their bandgaps span the ideal energy range for solar cells, from 1.0 eV for CZTSe to 1.45 eV for CZTS.[5] The band gap can be tuned between these two values by forming $Cu_2ZnSnS_{4x}Se_{4(1-x)}$ alloys and solar cells based on such alloys have already achieved power conversion efficiencies as high as 12.04%[6]. Rapid rise in power conversion efficiencies over a relatively short time period (~5 years) is remarkable but these efficiencies still fall significantly short of the 20.4% achieved by CIGS based solar cells.[7] Closing this gap requires a better understanding of the factors that affect the film composition during synthesis because solar cell efficiencies depend strongly on the elemental composition of the CZTS layer.

Solar cells made from stoichiometric Cu_2ZnSnS_4 films perform significantly worse than those made from copper poor films. Specifically, the highest efficiency cells tend to be Cu poor ([Cu/(Zn+Sn)] ~ 0.8) and Zn rich ([Zn/Sn] ~ 1.1).[3,8] However, synthesizing phase-pure CZTS thin films with a specific off-stoichiometric composition is non-trivial. This is partially due to the fact that CZTS has a rather small window of phase stability before secondary phases form.[9] Tuning the composition is also complicated because Sn may leave the film at elevated temperatures if the composition of

the vapor phase above the film is not controlled carefully. For example, low S partial pressures above the film favor Sn loss.[10–12] This problem is further exacerbated when films are annealed or sulfidized in open systems, where vapor composition and pressures are not well controlled and Sn loss through the vapor phase may be irreversible.

We synthesized CZTS films *via ex situ* sulfidation of cosputtered Cu-Zn-Sn alloy films and studied the dependence of the CZTS phase purity and composition on the elemental composition of the alloy films. An important feature of our work is that the sulfidation is conducted in an isothermal closed system such that the film and the vapor phase above the film is expected to reach equilibrium: material (*e.g.,* Sn) loss from the system by flow is avoided. We found that the Cu and Zn concentrations in the CZTS film depended on the composition of the Cu-Zn-Sn precursor film. However, the Sn concentration in the film is self-regulating such the ratio of Cu to Sn ([Cu/Sn]) is always ~ 2 over a wide range of starting Sn concentrations in the precursor film provided that sufficient Sn is present in the system. Precursor films that were significantly Sn rich undergo copious amounts of Sn loss via SnS evaporation until the Cu/Sn ratio is ~ 2. The Cu/Sn ratio in films that were initially Sn deficient, could be increased to ~ 2 by including elemental Sn in the sulfidation ampoule. Time dependent experiments revealed the surprising mechanism behind this Sn regulation. Early in the sulfidation process a majority of the Sn in Sn rich precursors is lost to the vapor phase through rapid formation and subsequent evaporation of SnS. However, the SnS vapor eventually reacts with $Cu_{2-x}S$ in the film to form Cu_2SnS_3. This non-volatile ternary phase is then converted to CZTS through interdiffusion and mixing with ZnS. When the precursor film is made Sn-poor but elemental Sn is included in the system, sulfur vapor reacts to form SnS vapor to provide the missing Sn to the film.

3.2 Experimental

CZTS films were synthesized *via ex situ* sulfidation of 250 nm thick Cu-Zn-Sn metal films on soda lime glass (SLG) substrates.[13,14] The metallic precursor films were co-sputtered from Cu/Zn (35 at% Cu) and Cu/Sn (60 at% Cu) targets at 10 mTorr using Ar

as the working gas in a sputtering chamber with a base pressure of 2×10^{-7} Torr. Following deposition, the Cu-Zn-Sn precursor films were sealed in an evacuated quartz ampoule (base pressure of 10^{-6} Torr) with ~ 1 mg of solid S, and if the precursor film was Sn deficient, ~ 1 mg of solid Sn. This ampoule, containing the film, S, and, in some experiments Sn, was placed in a box furnace where it was heated at a rate of 6.5 ^{o}C/min to 600 ^{o}C, sulfidized isothermally for 8 hrs, and then allowed to cool to room temperature naturally. The films were characterized using X-ray diffraction (XRD), confocal Raman microscopy, scanning electron microscopy (SEM), and energy dispersive X-ray spectroscopy (EDS). Specifically, XRD from sulfidized films were acquired using a Bruker D8 Discover system equipped with a Cu $K\alpha$ x-ray source, 0.8 mm beam collimator, and a Hi-Star 2D area detector. Raman spectra were collected at room temperature using a WiTec alpha300R confocal Raman microscope equipped with a UHTS300 spectrometer and a DV401 CCD detector. The films were illuminated with an Omnichrome Ar ion laser (514.5 nm, ~300 nm beam spot size) while Raman scattering was collected in backscattering geometry and dispersed with an 1800 lines/mm grating, resulting in a spectral resolution of 0.02 cm^{-1}. The morphology and spatially averaged elemental composition of the sulfidized films were examined using a JEOL 6500 SEM equipped with a Thermo-Noran Vantage EDS detector. The electron energy was set at 15 keV both for imaging and EDS measurements. At this energy the EDS probe depth is estimated to be near 2 µm, ensuring that the entire depth of the sulfidized films was examined.

3.3 Results and Discussion

3.3.1 Effects of Precursor Composition

We explored many different precursor film compositions and these starting compositions are plotted as green circles on the ternary diagram in Figure 3.1. Representation of the precursor Cu-Zn-Sn alloy film composition (no sulfur) on the ternary sulfide diagram requires a conversion. For example, the precursor Cu-Zn-Sn alloy film composition that corresponds to stoichiometric $Cu_2ZnSnS4$ is 50% Cu, 25% Zn, and

25% Sn. On Figure 3.1 this stoichiometric composition would plotted as a green circle at 33.3% Cu2S, 33.3% ZnS and 33.3% SnS2. After sulfidation, we characterized all CZTS films thoroughly and the corresponding compositions are shown as blue squares in Figure 3.1. The S content in all sulfidized films was 48% and varied only within the error of the EDS from film to film.

We find that if the precursor film is Sn rich (up to 45% of the metals), excess Sn leaves the film during sulfidation until the final Cu/Sn ratio becomes ~ 2. Moreover, when precursor films with Sn-deficient compositions (*i.e.* [Cu/Sn] > 2) are sulfidized with elemental Sn (1 mg) in the sulfidation ampoule, in addition to the S charge, the Sn can be incorporated film until the Cu/Sn ratio rises to ~ 2. Thus, the Sn content in the film is self-regulating such that the Cu/Sn ratio becomes ~2 at equilibrium as long as adequate Sn is present in the entire system. This is made visual by Figure 3.1 where scattered green circles, representing the composition of precursor films prior to sulfidation, collapse to a line of blue squares, representing the composition of sulfidized films. The Cu/Sn ratio along this line is 2.

Inclusion of Sn in the annealing system was shown by Redinger *et al.*[12] as an effective strategy to counter SnS loss from the film[10] via the reaction Cu2ZnSnS4(s) ⇔ Cu2S(s) + ZnS(s) + SnS(g) + ½ S2(g). Redinger *et al.* proposed that Sn reacts with S to form SnS vapor which than drives the decomposition reaction in the reverse reaction. Our experiments show that Sn from SnS vapor can be incorporated into the film even when the precursor films are significantly Sn poor to begin with. Moreover, including excess Sn in the precursor films is adequate to prevent detrimental Sn loss, as long as the Sn leaving the film as SnS vapor remains above the film (as in a closed system) and is not swept away by flow. Zinc and copper loss from the films was negligible and the elemental composition moved along lines of constant ZnS and Cu2S. The latter is expected because Cu vapor pressure at 600 ^{o}C is very low. Zinc vapor pressure is high and rises from 1.76 x 10^{-14} Torr at25 ^{o}C to 11.4 Torr at 600 ^{o}C. Absence of significant Zn loss from the film suggests that as the temperature increases Zn is sulfidized rapidly

before it can leave the film as Zn metal vapor.[14] This observation is consistent with that reported by Mousel *et al.* who studied selenization.[15,16]

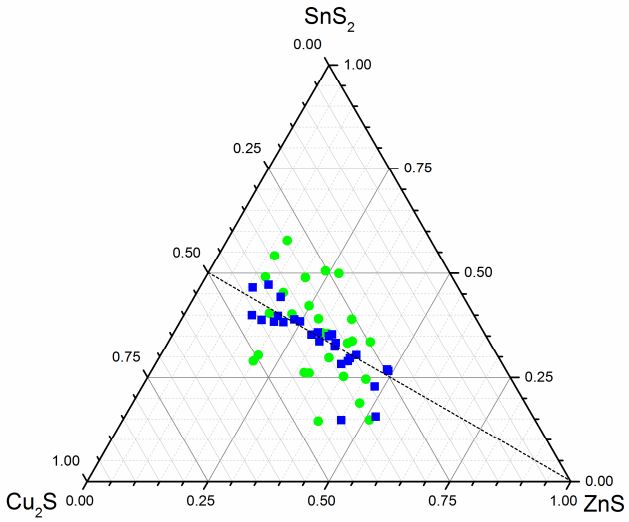

Figure 3.1 Ternary diagram showing precursor (green dots) and sulfidized (blue square) compositions. Sulfidized films have a S composition of ~ 48%. The dotted line is a line of constant [Cu/Sn] of 2.

Figures 3.2 (a)-(e) show six representative films with different compositions. Figures 3.2 (a)-(c) show SEM images of three films (labelled A, B and C) all of which were synthesized by sulfidizing initially Sn rich precursor films (i.e., [Cu/Sn] < 2). The initial and final compositions of these films are listed in Table 3.1. Prior to sulfidation, in addition to being Sn rich, Film A was Zn poor ([Cu/Zn] > 2), Film B had a stoichiometric amount of Zn ([Cu/Zn] ~ 2) and Film C was Zn rich ([Cu/Zn] < 2). These three compositions were chosen as examples to illustrate four important observations. First, during sulfidation, excess Sn in the precursor films leaves the film as SnS until the Cu/Sn ratio in the film increases to ~ 2. Second, stoichiometric CZTS can be obtained even if there is excess Sn in the precursor film as long as the Cu/Zn ratio is ~ 2. Third, when the Cu/Zn ratio is lower than 2, excess Zn precipitates as ZnS. Finally, significant material loss (*e.g.,* Sn as SnS) from the film creates voids in the film. For example, prior to sulfidation, film A was significantly Sn rich and significantly Zn poor. Upon sulfidation, the film remained Zn poor, but just the right amount of Sn left the film such that the

Cu/Sn ratio in the sulfidized film increased to ~ 2, the value expected for stoichiometric CZTS. While the precursor film was continuous, the sulfidized film (Figure 3.2(a)) is discontinuous with voids separating large grains. We attribute this morphology to significant material loss from the film (i.e., Sn as SnS vapor). Prior to sulfidation, film B was also Sn rich but the Cu/Zn ratio was nominally stoichiometric (~ 2). Upon sulfidation, a nominally stoichiometric CZTS film was obtained: the Cu/Zn ratio remained at ~ 2 while, again, just the right amount of Sn left the film as SnS such that the Cu/Sn ratio in the sulfidized film increased to ~ 2. The plan view SEM (Figure 3.2(c)) of this film showed voids between the grains indicative of material loss. Finally, prior to sulfidation, film C, was slightly Zn and Sn rich ([Cu/Zn] < 2 and [Cu/Sn] < 2). Upon sulfidation, again, Sn loss from the system increases the Cu/Sn ratio to ~ 2. However, the excess Zn precipitates as ZnS precipitates and are visible as small insulating grains in Figure 3.2(c): these grains appear brighter than the CZTS grains.

Table 3.3.1 Precursor and sulfidized film compositions as determined from EDS. The precursor composition that corresponds to stoichiometric Cu2ZnSnS4 in absence of metal loss from the film is 50% Cu, 25% Zn and 25% Sn. The stoichiometric sulfidized film composition

	Precursor			**Sulfidized**			
Film	Cu	Zn	Sn	Cu	Zn	Sn	S
A	45.78	9.61	44.61	32.02	5.81	14.23	47.94
	(29.68)	(12.46)	(57.85)	(44.41)	(16.12)	(39.47)	
B	40.57	19.18	40.25	27.25	12.41	12.96	47.38
	(25.45)	(24.06)	(50.49)	(34.94)	(31.82)	(33.24)	
C	44.09	29.56	26.35	22.99	16.30	12.18	48.53
	(28.28)	(37.92)	(33.80)	(28.76)	(40.78)	(30.47)	
D	66.15	13.53	20.32	30.15	8.02	14.36	47.47
	(49.42)	(20.22)	(30.36)	(40.25)	(21.41)	(38.34)	
E	58.26	23.30	18.44	26.03	11.12	13.42	49.43
	(41.10)	(32.88)	(26.02)	(34.66)	(29.61)	(35.73)	
F	46.22	34.91	18.87	20.58	16.93	11.69	50.79
	(30.06)	(45.40)	(24.54)	(26.45)	(43.51)	(30.04)	

Figures 3.2 (d)-(f) show SEM images of three films (labelled D, E and F) all of which were synthesized by sulfidizing initially Sn poor precursor films (i.e., [Cu/Sn] > 2, see Table 3.1). These films were sulfidized with 1 mg of Sn present in the sulfidation

ampoule. Prior to sulfidation, in addition to being Sn poor, Film D was Zn poor ([Cu/Zn] > 2), Film E had a stoichiometric amount of Zn ([Cu/Zn] ~ 2) and Film F was Zn rich ([Cu/Zn] < 2). Despite starting out Sn poor, all three films have a Cu/Sn ratio of ~ 2 after sulfidation indicating that additional Sn was incorporated into the films. It is also quite obvious from the plan view SEM images that film D is much more compact and dense than film A. This is expected because there is no material loss from the film D; in fact, there is net material addition to film D through reaction of SnS vapor to increase the Sn content in the film. This is in contrast to film A which lost Sn during sulfidation. Finally, the Zn-rich film F, like film C, exhibits small insulating domains of ZnS on its surface.

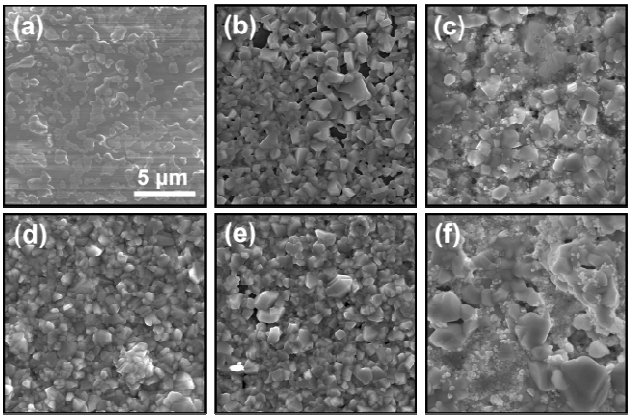

Figure 3.2 Plan view SEM images of selected films A (a), B (b), C (c), D (d), E (e), and F (f). Same scale bar applies to all images.

We identified the phases present in films A-F using XRD in conjunction with Raman scattering (Figures 3.3 and 3.4). XRD from CZTS, Cu2SnS3 and ZnS are virtually indistinguishable except for two weak diffractions at $2\theta = 36.9^{o}$ and 37.9^{o} which are unique to CZTS. XRD from film A shows that these unique CZTS diffraction peaks are absent. That the low intensity, identifying peaks for CZTS are absent indicates that a substantial fraction of the film may in fact be Cu_2SnS_3 as its diffraction pattern is nearly identical to that of CZTS. We also detect weak diffractions that can be assigned to Cu_3SnS_4. This is consistent with the Raman spectrum which shows a broad feature in the 290-305 cm^{-1} range in addition to a peak at 336 cm^{-1} and another broad feature at 355 cm^{-}

[1].[17-19] The latter two overlap with Raman scattering peaks for CZTS and ZnS but the feature at 290-305 cm^{-1} indicates the presence of Cu2SnS3. There is no indication of the formation of copper sulfides in XRD or Raman. We conclude that this film is mostly Cu_2SnS_3 with some CZTS because there is not enough Zn in the film to convert all Cu_2SnS_3 to CZTS. Raman peaks characteristic of Cu_3SnS_4 are expected at 295 cm^{-1}, 318 cm^{-1} and 248 cm^{-1}. While two of these peaks overlap with those from Cu_2SnS_3 and CZTS, the broad feature at 318 cm^{-1} in the Raman spectrum of film A (Figure 3.4) is consistent with Cu_3SnS_4. We conclude that in absence of adequate Zn to convert all Cu to CZTS, copper tin sulfide phases form and excess Sn leaves the film as SnS. Cu/Sn ratio in both CZTS and Cu_2SnS_3 is 2 while it is 3 in Cu_3SnS_4. The measured Cu/Sn ratio in film A is 2.25, close to 2, which indicates that just enough Sn has remained in the film to form mostly Cu_2SnS_3 and CZTS and the excess has evaporated as SnS. Cu/Sn ratio slightly higher than 2 is consistent with the formation of small amounts of Cu_3SnS_4.

When the Cu/Zn ratio in the Sn-rich precursor film is decreased to 2 by increasing the amount of Zn (film B) the XRD of the sulfidized film becomes consistent with that expected from phase pure CZTS: the unique CZTS diffraction peaks at $2\theta = 36.9^o$ and 37.9^o appear while the weak Cu_3SnS_4 diffractions disappear. Moreover, the Raman spectrum exhibits peaks characteristics of CZTS at 284 cm^{-1} and 333 cm^{-1}. The broad features for Cu2SnS3 (290-305 cm^{-1}) and Cu3SnS4 (318 cm^{-1}) have also disappeared. We conclude that there is now enough Zn in the precursor film to convert all Cu to CZTS. Cu/Sn ratio is 2.1, very close to 2 and up significantly from the Cu/Sn ratio of 1 in the precursor film because excess Sn has left the film as SnS. Increasing Zn in Sn-rich films further (film C) leads to the formation of ZnS which is difficult to detect by XRD, and even with Raman spectroscopy, but is most obvious in the SEMs as bright insulating Zn-rich regions (e.g., Figure 2(c)). The Cu/Sn ratio in film C is 1.9, again very close to 2 and up from the Cu/Sn ratio of 1.67 in the precursor film. In summary, the Sn-rich precursor films lose Sn such that the final Cu/Sn ratio in the films becomes ~ 2 after sulfidation. When these precursor films are Zn poor, copper tin sulfide phases form in addition to CZTS. When the precursor films are Zn rich ZnS forms in addition to CZTS.

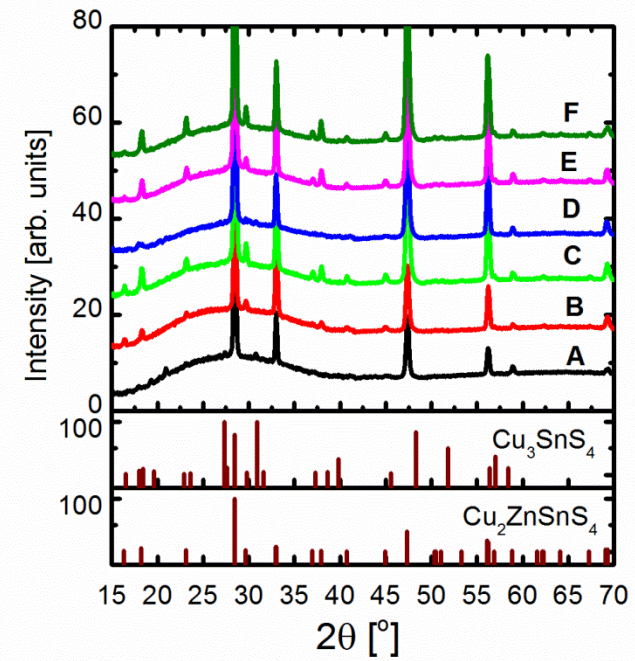

Figure 3.3 The XRD patterns collected from selected samples. The bottom panels show the expected powder diffraction patterns for Cu3SnS4 and CZTS.

If the precursor films are Sn poor, additional Sn can be incorporated into the film by including Sn in the sulfidation ampoule. The solid Sn reacts with S vapor to form SnS which can then react with the film to incorporate Sn into the film and bring the Cu/Sn ratio down to ~ 2. For example, the Cu/Sn ratio in film D decreased from 3.25 before sulfidation to 2.1 after sulfidation when Sn shots were included in the ampoule. Like film A, film D was also Zn poor. Like film A, CZTS diffraction peaks expected at $2\theta = 36.9^{o}$ and 37.9^{o} are undetectable in film D indicating that only a fraction of the film is CZTS. Like film A, the broad Raman scattering feature in the 290-305 cm^{-1} range indicate the presence of Cu2SnS3 in film D. Remarkably, even though films A and D have significantly different concentrations of Sn before sulfidation, the Cu/Sn ratio in both films is ~ 2 after sulfidation and both films are a mixture of copper tin sulfides and CZTS. Despite the fact that film D is 66% copper before sulfidation, there is no indication that the sulfidized film contains any copper sulfides. Apparently SnS can readily react with any copper sulfides that may have formed to form copper tin sulfide.

Unlike, film A, however, we do not detect any Cu_3SnS_4 diffractions perhaps suggesting that this phase forms when the precursor films are Sn rich and/or that there is no mechanism to form this phase while incorporating Sn as SnS from the vapor phase. When the amount of Zn in the precursor films is increased (films E and F) the unique CZTS diffraction peaks at $2\theta = 36.9^o$ and 37.9^o appear and the XRD indicate a phase pure CZTS. However, close examination of Film F under SEM, like film C, show ZnS grains because the precursor film is slightly Zn rich.

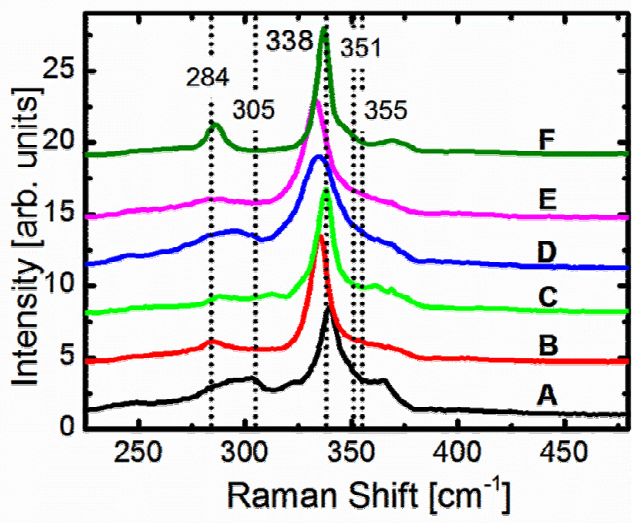

Figure 3.4 Raman spectra collected from selected films.

The simple view that emerges from our experiments is that if Cu-Zn-Sn alloys precursor films are sulfidized with excess Sn in the system, the amount of Sn in the film is self regulated such that Cu/Sn ratio in the sulfidized film is ~ 2 after sulfidation. The excess Sn can be in the alloy itself or in the sulfidation ampoule. However, care must be taken so that system is either closed or excess Sn does not leave the immediate vicinity of the film as SnS vapor. The relative amounts of Cu and Zn in the film determines secondary phases that may form. When the films are Zn deficient but there is excess Sn in the system, copper tin sulfide phases form in addition to CZTS. When the films are Zn rich, ZnS forms in addition to CZTS. The most significant difference between the films that were initially Sn rich and the films that were Sn-poor was the microstructure. Films

that underwent significant Sn loss tended to have more voids between the grains due to material loss.

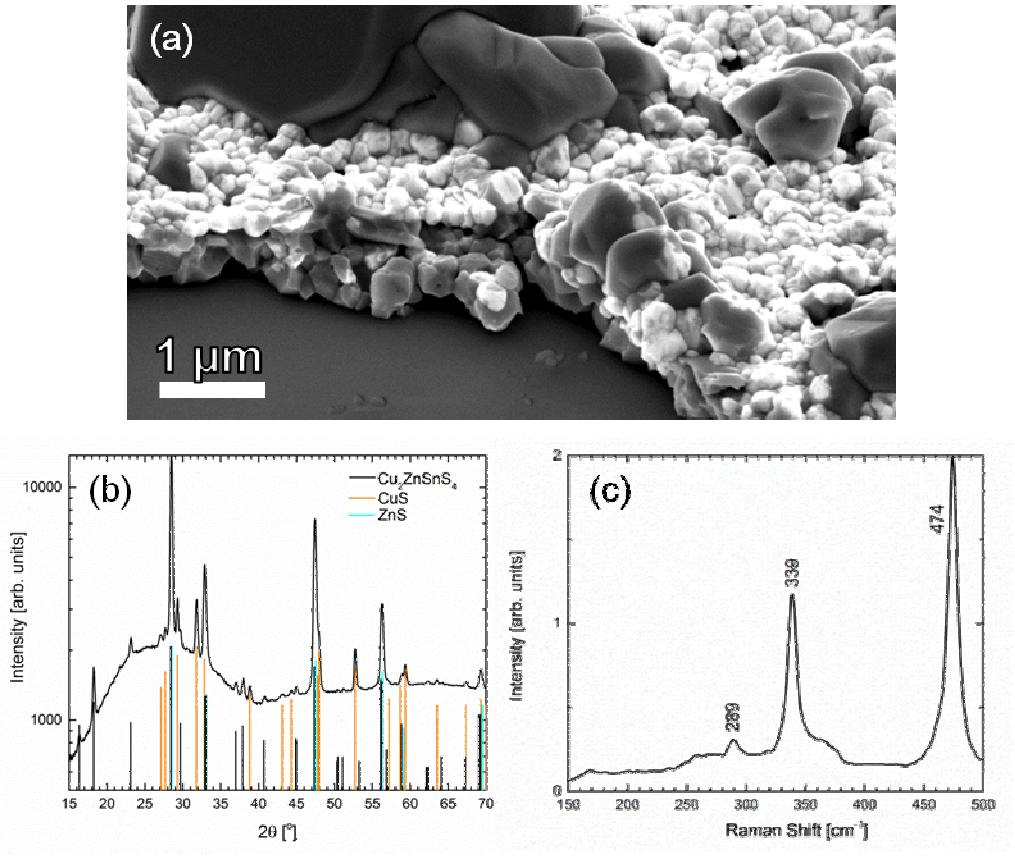

Figure 3.5 Panel (a) shows an SEM image of a sulfidized film that was initially very Sn poor (51% Cu, 38% Zn, 11% Sn) and sulfidized with Sn within the ampoule. The final atomic composition of this film was 24% Cu, 19% Zn, 6% Sn, and 51% S. The large features on on the surface of the film are domains of CuS, which sit atop a layer of ZnS, which appears much whiter in color due to ZnS's insulating nature. Below the layer of ZnS, next to the substrate and darker in color, is a layer of CZTS. The phase identification of these morphological features was performed by EDS. Structural characterization, including XRD (b) and Raman (c) confirm the presence of CZTS and CuS.

There is a limit on the Sn deficit in precursor film that can be made up by including Sn in the sulfidation ampoule. Specifically, a Sn-deficit could not be overcome completely in Zn-rich precursor films with Cu/Sn ratio greater than 3.6 (the lower right hand corner of Figure 3.1). An SEM image and XRD and Raman spectra for one of these films is shown in Figure 3.5. The sulfidized Zn-rich and very Sn poor precursor film was

comprised of CuS, ZnS, and CZTS. The film had a tri-layered structure with large (5 - 10 □m) CuS grains on a layer of ZnS, which was atop a layer of CZTS. At high temperatures, ZnS is soluble within Cu_2S,[8] and this layer on the surface of the film may have inhibited the incorporation of Sn as Sn diffusion into ZnS is very slow[20] We surmise that the Sn incorporation may have been suppressed by this film structure.

These observations suggest some strategies for synthesizing CZTS films suitable for solar cell. First, our results suggest that sulfidizing precursor films with Zn and Cu atomic composition reasonably near stoichiometric CZTS in presence of excess Sn may be an effective strategy to manipulate Cu and Zn related defects such as Cu vacancies and antisite defects. If there is excess Sn in the film, or if excess elemental Sn is included in the sulfidation ampoule in Cu/Sn ratio will approach 2 while Cu/Zn ratio will remain essentially unchanged. Second, our experiments suggest that to make dense, void free films it is better to start with a Sn-deficient precursor films and add Sn as SnS via the vapor phase. This approach eliminates a potential void formation mechanism.

3.3.2 The Mechanism of Sn Self-Regulation

The dependence of the films' phase composition on the atomic composition of the precursor films gives insight into the mechanism that regulates the Sn composition in the sulfidized films. Films where [Cu/Zn] > 2 tended to have Cu_2SnS_3 domains alongside the CZTS. Likewise to CZTS, within Cu_2SnS_3, [Cu/Sn] = 2. It has also been well documented that Cu_2SnS_3 is an intermediate phase en route to CZTS formation,[21,22] so it is also possible that any Sn not consumed by the intermediate phase Cu_2SnS_3 leaves as SnS vapor. However, it remains unclear as to if Cu_2SnS_3 forms out of the Cu-Sn alloy initially present in the precursor film, or if it forms from binary sulfides like SnS and $Cu_{2-x}S$ undergoing a solid state reaction, or if Sn leaves the film as SnS and later returns.

To elucidate the mechanism that regulates the Sn composition in sulfidized films, we studied the time dependce of the films' atomic and phase composition during sulfidation at low temperatures where reaction intermediates can be captured before full conversion. Specifically, precursor films with differing initial Sn concentrations were

sulfidized at 300 ^{o}C. Four ampoules were loaded into the furnace, and the furnace was heated to 300 ^{o}C at 6.5 ^{o}C/min. The first ampoule was removed from the furnace as soon as the temperature reached 300 ^{o}C (t=0 min). The remaining ampoules were removed 60 and 240 minutes later (t = 60 min and t = 240 min). After 480 minutes, the furnace was turned off and the last ampoule was allowed to cool to room temperature naturally.

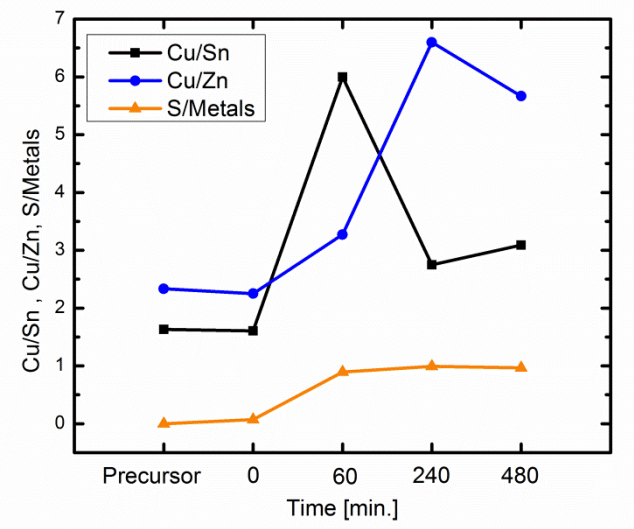

Figure 3.6 The atomic composition of copper-zinc-tin alloy films sulfidized at 300 ^{o}C as a function of sulfidation time.

Figures 3.6 and 3.7 summarize the temporal evolution of the films' atomic and the phase composition as a function of sulfidation time during these experiments. Figure 3.7 summarizes both the XRD (the colored bars) and the Raman scattering data (phases listed above the bars), The details of the analysis used to construct the phase-composition bar graph in Figure 3.7, has been described elsewhere.[16] Briefly, the fraction of each phase is determined from the the integrated intensity of a unique peak after normalizing these values by the film thickness, X-ray exposure time, and the expected relative intensity for the peak. The fraction is determined from the ratio of the normalized value for each phase with the sum for all the phases detected in the film by XRD. This gives a reasonable estimate of the phase composition, provided that the films are not textured. The

individual XRD and Raman data used to construct Figure 3.7 are shown in Figures 3.8 and 3.9, respectively.

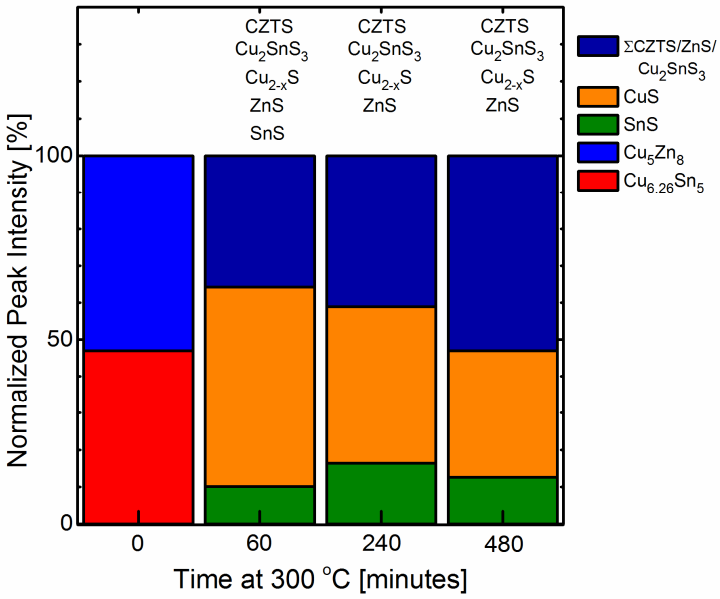

Figure 3.7 The phase composition of copper-zinc-tin alloy films sulfidized at 300 °C as a function of sulfidation time. The heights of the colored bars represent the fraction of the phases present in the film. The phases listed above each bar are those identified by Raman spectroscopy.

The precursor film is Sn rich and slightly Zn-poor such that [Cu/Sn] = 1.6 and [Cu/Zn] = 2.3. The precursor film consisted of elemental Zn, Cu, and Sn phases as well as the $Cu_{6.26}Sn_5$ phase. The phase composition of the precursor film is not plotted on Figure 3.7 because Zn and Cu diffractions overlap and the film is textured.

The atomic composition of the film removed immediately after the furnace has reached 300 °C (t=0) is nearly identical to that of the precursor film with very little S (~ 7%) incorporation. Similar to films sulfidized at 200 °C and discussed elsewhere,[16] we found by SEM and EDS, small insulating grains on the surface of the film which we attributed to the start of ZnS formation, shown in Figure 3.10; the volume fraction of these ZnS grains are below the detection limits of Raman and XRD. Based on XRD, the rest of the film appeared to be entirely alloyed and comprised of $Cu_{6.26}Sn_5$ and Cu_5Zn_8. This alloying and low sulfidation may be described via the reactions

$$5Sn_{(s)} + 6.26\ Cu_{(s)} \rightarrow Cu_{6.26}Sn_{5(s)} \qquad (3.1)$$

$$8Zn_{(s)} + 5\ Cu_{(s)} \rightarrow Cu_5Zn_{8(s)} \qquad (3.2)$$

and

$$Zn_{(s)} + S_{(g)} \rightarrow ZnS_{(s)} \qquad (3.3)$$

The film sulfidized for 60 minutes at 300 ^{o}C is nearly completely sulfidized with 47% sulfur. The cation composition has also changed dramatically: [Cu/Sn] has increased significantly to 6 and [Cu/Zn] has increased to 3.3. While nearly all the metals have been sulfidized, a small fraction, of elemental Sn and Cu_5Zn_8 remain as determined by XRD. This elemental Sn is textured, and as such has been omitted from Figure 3.7, but based on the compositional analysis we believe elemental Sn comprises a rather small amount of the film. The collected XRD also shows a small shoulder remains near $2\theta = 43.3^{o}$ which we attribute to the most intense reflection for Cu_5Zn_8. XRD shows the presence of SnS, CuS, as well as diffractions that can be assigned to CZTS, Cu_2SnS_3 or ZnS. These last three phases are indistinguishable by XRD and they are represented by the blue bar labelled $\sum$CZTS/ZnS/Cu_2SnS_3.[9] Raman scattering confirms the presence of all three, though the fraction of each phase cannot be easily quantified from the Raman spectrum. There is also some unsulfidized Cu_5Zn_8 alloy remaining in the film, though the most intense XRD peak from Cu_5Zn_8 ($2\theta = 43.30^{o}$) overlaps with a lower intensity peak ($2\theta = 43.10^{o}$; relative intensity of 6%) from CuS. If we assume this peak is due entirely to Cu_5Zn_8, and this peak was quantified and included in Figure 3.7, its contribution would be too small to see at 1.6%.

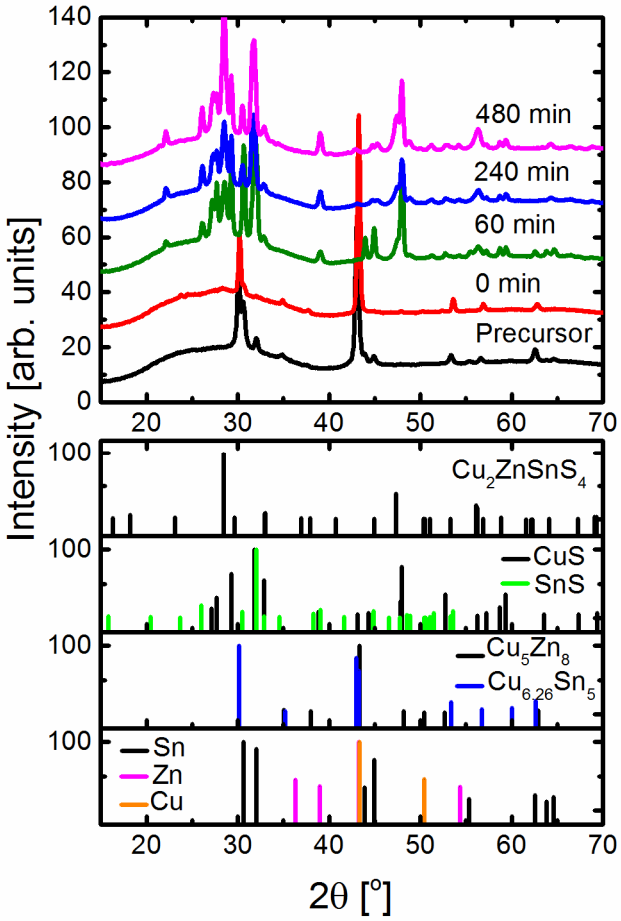

Figure 3.8 The top panel displays the collected XRD patterns for a precursor film and films subsequently sulfidized for 0, 60, 240, and 480 minutes at 300 °C. The bottom panel displays the standard powder diffraction patterns for the various phases present within the films.

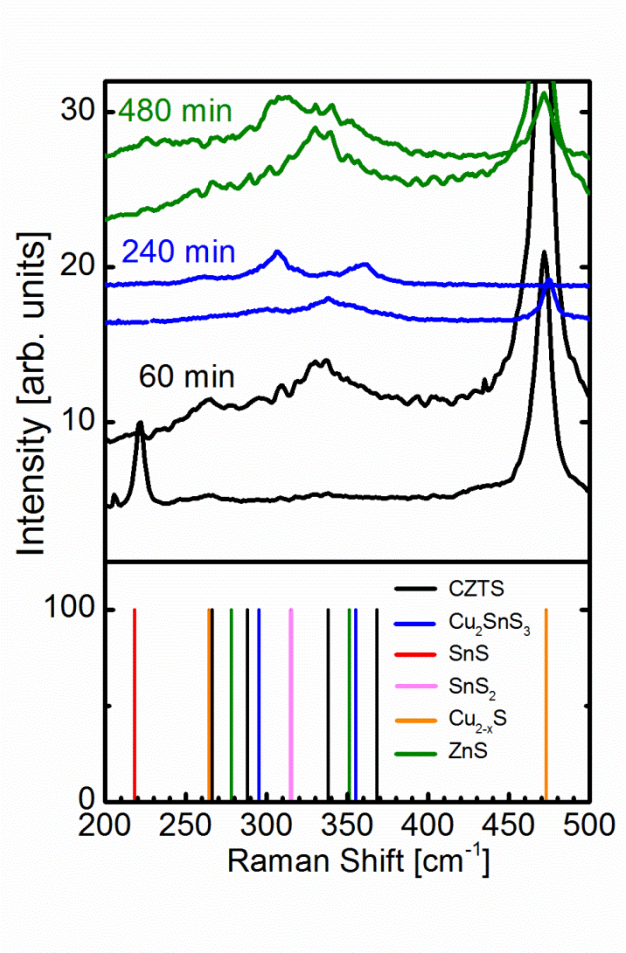

Figure 3.9 The top panel displays Raman spectra collected on films sulfidized for 60, 240 and 480 minutes at 300 ^{o}C. As a Raman microscope was used, we included two spectra representative of the phases present within the film. The bottom panel references expected peak locations for various phases for comparison.

These observations can be understood by considering the reactions that must occur to convert the metal precursor alloy film to the thermodynamically stable metal sulfides. Elemental copper, zinc and tin phases can sulfidize directly to form binary sulfides via

$$Sn_{(\ell)} + S_{(g)} \rightarrow SnS_{(s)} \rightarrow SnS_{(g)} \qquad (3.4)$$

$$Cu_{(s)} + S_{(g)} \rightarrow CuS_{(s)} \qquad (3.5)$$

and

$$Zn_{(s)} + S_{(s)} \rightarrow ZnS_{(s)} \qquad (3.3)$$

In the presence of the S vapor, the copper-zinc and copper-tin alloys segregate as the elements comprising these alloys sulfidize. For example, the $Cu_{6.26}Sn_5$ alloy readily dissociates into Cu and Sn via

$$Cu_{6.26}Sn_{5(s)} \rightarrow 6.26Cu_{(s)} + 5Sn_{(\ell)} \qquad (3.6)$$

Since Sn melts at 231 ^{o}C, it is formed as a liquid and can sulfidize via reaction 3.4. Some of the Sn remains unsulfidized and crystallizes upon cooling to form the textured elemental Sn observed in the XRD. While the reported values for $\Delta_f G_{SnS}$ are lower than that of $\Delta_f G_{CuS}$, the formation of CuS appears to be faster as we found no evidence of elemental Cu remaining alongside crystallized Sn (see Table 3.2). It should be noted that similar results have been reported elswhere.[23] This may possibly be due to diffusion limitations. Within the $Cu_{6.26.}Sn_5$ matrix, Cu diffusion is faster.[24] The Cu may diffuse to the surface of the film where it readily reacts with the S vapor, while Sn remains within the film and melts. It is widely thought that cation diffusion is much faster than S diffusion through sulfide mediums, so the formation of CuS and some ZnS on the surface may be limiting the sulfidation of Sn.

Similarly to the copper-tin alloy, the copper-zinc alloy dissociates via

$$Cu_5Zn_{8(s)} \rightarrow 5Cu_{(s)} + 8\ Zn_{(s)} \qquad (3.7)$$

and the elemental Cu and Zn are sulfidized to form CuS and ZnS. A small amount of Cu_5Zn_8 alloy remaining in the film indicates that it does not completely dissociate within the 60 minutes. The Cu_5Zn_8 alloy does have a lower $\Delta_f G$ at 300 ^{o}C compared to the $Cu_{6.26}Sn_5$ alloy, and is hence more stable. Again anion diffusion through the sulfide phases may also be limiting the dissociation and sulfidation of Cu_5Zn_8 as well.

The changes in the elemental composition of the film is consistent with Zn and SnS intermediates which have high vapor pressures and can leave the film via

$$Zn_{(s)} \rightarrow Zn_{(g)} \qquad (3.8)$$

and reaction 3.4. The vapor pressure of Zn at 300 ^{o}C is significant (~ 1.4 mTorr) and some Zn evaporates before it is converted to low vapor pressure ZnS. This evaporation is responsible for the rise in the Cu/Zn ratio. In most high temperature sulfidation (e.g., 500-600 ^{o}C) treatments, the film is heated quickly through 300 ^{o}C, the temperature at which sulfidation and evaporation appear to be in competition to determine the Zn content in the film. This observation underscores the importance of the heating rates in sulfidation treatments. If the heating rate is slow Zn may leave the film.

Table 3.2 Thermodynamic data for the formation of binary sulfides and alloys.

Reaction	ΔG_f (kJ/mol) @ 300 ^{o}C	Reference
$2Cu + S_2 (g) \rightarrow 2CuS$	-146.02	24
$2Sn + S_2 (g) \rightarrow 2SnS$	-243.04	24
$Zn + S_2(g) \rightarrow 2ZnS$	-427.88	24
$6Cu + 5Sn \rightarrow Cu_6Sn_5$	-7.42	25
$5Cu + 8Zn \rightarrow Cu_5Zn_8$	-12.34	25

After t = 240 min at 300 ^{o}C, the S concentration reaches 50%. Remarkably the Cu/Sn ratio ([Cu/Sn] = 2.75), while still higher than the precursor film, is significantly lower than the film that was sulfidized for 60 minutes. Much of the Sn that leaves the film during the first 60 minutes is reincorporated into the film. The film is comprised entirely of sulfide phases, including SnS, CuS, ZnS, Cu_2SnS_3, and CZTS. In particular, the fraction of ZnS, Cu_2SnS_3, and/or CZTS has increased. This suggests that SnS from the vapor phase reacts with CuS to form Cu_2SnS_3 via

$$2CuS_{(s)} + SnS_{(g)} \rightarrow Cu_2SnS_{3(s)} \qquad (3.9)$$

and this reaction may be in addition to the solid phase reaction

$$2CuS_{(s)} + SnS_{(s)} \rightarrow Cu_2SnS_{3(s)} \qquad (3.10)$$

The reaction in the solid phase would shift the solid-vapor equilibrium to incorporate the SnS vapor into the film. It is not clear if a heterogeneous reaction takes place, or whether SnS condenses on the surface of the film and undergoes a solid-state reaction with CuS to form Cu_2SnS_3, or possibly both. Either way, SnS lost from the film can return to the film in a closed system. The Zn loss from the film after 240 minutes at 300 ^oC is significant: the Cu/Zn ratio in the sulfidized film has risen to 6.6 indicating that Zn continued to sublime. We infer that during the 240 minutes there was still unsulfidized Zn in the film and that at 300 ^oC Zn sublimation rate is comparable to ZnS formation rate. The ZnS that does remain within the film interdiffuses with Cu_2SnS_3 to form CZTS via

$$Cu_2SnS_{3(s)} + ZnS_{(s)} \rightarrow Cu_2ZnSnS_{4(s)} \qquad (3.11)$$

Within the accuracy of the EDS, the elemental composition of the film sulfidized at 300 ^oC for t = 480 min, is similar to that of the film sulfidized for t = 240 min. The film is comprised entirely of sulfides, though the fraction of $\sum$CZTS/ZnS/Cu_2SnS_3 has increased at the expense of CuS and SnS. Increase in the $\sum$CZTS/ZnS/Cu_2SnS_3 fraction is attributable to solely the increase in the Cu_2SnS_3 phase because there is no increase in the amount of Zn within the film to make ZnS or CZTS. Hence after t = 240 min, the film is slowly converting to Cu_2SnS_3 via the reaction of CuS with SnS.

These experiments demonstrate the importance of the vapor phase composition over the film during sulfidation of copper-zinc-tin alloys to form CZTS. Favorable Gibbs energy of formation of CuS and SnS drives the dissociation $Cu_{6.26}Sn_5$ alloy and subsequent rapid sulfidation of Cu and Sn to form the binary sulfides. Moreover, there is not enough Cu within $Cu_{6.26}Sn_5$ alone to form single phase Cu_2SnS_3. Consequently, CuS and SnS remain as intermediates. The formation of significant amounts of Cu_2SnS_3 relies on the dissociation of Cu_5Zn_8 for more Cu, which appears to be a slower process. This gives ample time for a considerable amount of the SnS within the film to evaporate. Thus, before CZTS is formed, a majority of the Sn may be lost to the vapor phase. As

more CuS is formed, SnS vapor and/or solid react with CuS to form Cu_2SnS_3. This is the same mechanism in which the Sn content of an initially Sn deficient film may be increased by including elemental Sn in the sulfidation ampoule. This pathway is the reason behind the self-regulating nature of Sn: Sn concentration in the film is governed by the availability of CuS to form Cu_2SnS_3.

Previous experiments hypothesized that the Sn loss from the films occurs after CZTS formation and as a consequence of decomposition *via*

$$2Cu_2ZnSnS_4 \Leftrightarrow 2Cu_2S + 2ZnS + 2SnS + S_2$$

In contrast, our experiments show that that Sn loss as well as incorporation into the film occurs during the *formation* of CZTS. The sulfur pressure in our closed system at 600 ^oC is ~36 Torr, well above the necessary partial pressure for CZTS stability.[10] If this reaction were to take place in an open system, or a poorly controlled pseudo-open system, the film would be unable to recover from the initial Sn loss via the mechanisms described in this article.

3.4 Conclusion

During synthesis of CZTS films by *ex situ* sulfidation of Cu-Zn-Sn alloy films in closed systems, the final Sn content is self regulating. If the metal precursor film is Sn rich, the Sn concentration decreases until [Cu/Sn] becomes ~ 2. If the metal precursor film is Sn deficient, the Sn concentration can be increased by including elemental Sn in the sulfidation ampoule. Elemental Sn readily sulfidizes to generate SnS vapor which is incorporated into the film until the Cu/Sn ratio becomes ~ 2. Material loss from Sn rich precursor alloy films result in CZTS films with voids. while sulfidation of Sn-poor precursor films with Sn in the sulfidation ampoule eliminates the voids and lead to compact CZTS films. A detailed investigation of the time dependence of sulfidation at 300 ^oC showed that SnS is lost from the film during the *formation* of CZTS, not as a result of its decomposition. A significant fraction of the Sn can evaporate from the precursor film as SnS, but is reincorporated via reactions with CuS to form Cu_2SnS_3. This

mechanism is the reason why Sn can be added to Sn deficient films through the vapor phase.

3.5 References

1. Norris, D. J.; Aydil E. S. *Science* 2012, *338*, 625-626.
2. Wadia C.; Alivisatos, A. P.; Kammen, D. M. *Environ. Sci. Technol.* 2009, *43*, 2072-2077.
3. Mitzi, D. B.; Gunawan, O.; Todorov, T. K.; Wang, K.; Guha, S. *Sol. Energy Mater. Sol. Cells* 2011, 1–16.
4. Ito, K.; Nakazawa, T. *Jpn. J. Appl. Phys.* 1988.
5. Nakayama, N.; Ito, K. *Appl. Surf. Sci.* 1996, *92*, 171–175.
6. Winkler, M. T.; Wang, W.; Gunawan, O.; Hovel, H. J.; Todorov, T. K.; Mitzi, D. B. *Energy Environ. Sci.* 2014, *7*, 1029.
7. Chirilă, A.; Reinhard, P.; Pianezzi, F.; Bloesch, P.; Uhl, A. R.; Fella, C.; Kranz, L.; Keller, D.; Gretener, C.; Hagendorfer, H.; Jaeger, D.; Erni, R.; Nishiwaki, S.; Buecheler, S.; Tiwari, A. N. *Nat. Mater.* 2013, *12*, 1107–1111.
8. Katagiri, H.; Jimbo, K.; Tahara, M. *MRS Proc.* 2009, *1165*.
9. Olekseyuk, I, Dudchak, I.V., Piskach, L. V. *J. Alloys Compd.* 2004, *368*, 135–143.
10. Weber, A.; Mainz, R.; Schock, H. W. *J. Appl. Phys.* 2010, *107*, 013516.
11. Scragg, J. J.; Ericson, T.; Kubart, T.; Edoff, M.; Platzer-Björkman, C. 2011, 4625–4633.
12. Redinger, A.; Berg, D. M.; Dale, P. J.; Siebentritt, S. *J. Am. Chem. Soc.* 2011, *133*, 3320–3323.
13. Johnson, M.; Baryshev, S. V.; Thimsen, E.; Manno, M.; Zhang, X.; Veryovkin, I. V.; Leighton, C.; Aydil, E. S. *Energy Environ. Sci.* 2014, *7*, 1931-1938.
14. Johnson, M.; Manno, M.; Zhang, X..; Leighton, C.; Aydil, E. S. *submitted.*

15. Mousel, M.; Schwarz, T.; Djemour, R.; Weiss, T. P.; Sendler, J.; Malaquias, J. C.; Redinger, A.; Cojocaru-mirédin, O.; Choi, P.; Siebentritt, S. *Adv. Energy Mat.* 2014, *4*
16. Mousel, M.; Redinger, A.; Djemour, R.; Arasimowicz, M.; Valle, N.; Dale, P.; Siebentritt, S. *Thin Solid Films*. 2013, *535*, 83–87.
17. Fernandes, P. A.; Salome, P. M. P.; da Cunha, A. F. *J. Phys. D.* 2010, *43*, 215403.
18. Cheng, A.-J.; Manno, M.; Khare, A.; Leighton, C.; Campbell, S. A.; Aydil, E. S. *J. Vac. SCi. Technol. A* 2011, *29*, 051203.
19. Berg, D. M.; Djemour, R.; Gutay, L.; Siebentritt, S.; Dale, P. J.;Fotane, X.; Izquierdo-Roca, V.; Perez-Rodriguez, A. *Appl. Phys. Lett.* 2012, *100*, 192103.
20. Thimsen, E.; Baryshev, S.V.; Martinson, A. B. F.; Elam, J. W.; Veryovkin, I. V.; Pellin, M. J. *Chem. Mat.* 2013, *25*, 313-319
21. Schurr, R.; Hölzing, A.; Jost, S.; Hock, R.; Voβ, T.; Schulze, J.; Kirbs, A.; Ennaoui, A.; Lux-Steiner, M.; Weber, A. *Thin Solid Films* 2009, *517*, 2465–2468.
22. Han, J.; Shin, S. W.; Gang, M. G.; Kim, J. H.; Lee, J. Y. *Nanotechnology.* 2013, *24*, 095706.
23. Yin, X.; Tang, C.; Sung, L.; Shen, Z.; Gong, H. *Chem. Mat.*2014, *26*, 2005-2014
24. Vaughan, D.; Craig, J. *Mineral Chemistry of Metal Sulfides*; Cambridge University Press: London, UK, 1978.
25. Yu, S.; Wang, M.; Hon, M. *J. Mater. Res.* **2001**, *16*,76-82 .
26. Kumar, S.; Handwerker, C. A.; Dayananda M. A. *J. Phase Equilib. Diff.* 2011, *32*, 309-319.

Chapter 4

Alkali-metal-enhanced grain growth in Cu2ZnSnS4 thin films

This was previously published as: Johnson, M.; Baryshev, S. V.; Thimsen, E.; Manno, M.; Zhang, X.; Veryovkin, I. V.; Leighton C.; Aydil, E. S. (2014). Alkali-metal-enhanced grain growth in Cu_2ZnSnS_4 thin films. *Energy & Environmental Science*, *7*(6), 1931. doi:10.1039/c3ee44130j - Reproduced by permission of The Royal Society of Chemistry

4.1 Introduction

Copper zinc tin sulphide, copper zinc tin selenide and their alloys [$Cu_2ZnSn(S,Se)_4$ commonly abbreviated as CZTS] are sustainable alternatives to copper indium gallium selenide (CIGS) and CdTe as the light absorbing material in thin film solar cells.[1-3] The highest efficiency CZTS solar cells are almost always grown on Mo-coated soda lime glass (SLG). This substrate choice is based on three-decades of collective experience with CIGS solar cells, where it was shown that Na readily diffuses from the SLG, through the Mo back contact layer, into the CIGS, thereby increasing the power conversion efficiency.[4-9] While the precise mechanisms and fundamental origin of this efficiency enhancement are still debated, it is clear that Na somehow affects the microstructure and carrier concentrations in the CIGS films. To date, very few investigations have focused on precisely how Na influences the microstructure and electronic properties of CZTS. Prabhakar *et al.*[10] and Hliang Oo *et al.*[11] have observed that growing CZTS on SLG or treating a precursor film with an aqueous solution of Na_2S before sulfidation lead to large grains, and Li *et al.*[12] demonstrated that co-evaporating CZTS onto substrates containing Na led to higher hole concentrations, increased carrier mobilities, and improved solar cell efficiencies. In fact, SLG hosts numerous impurities in addition to Na including K, Ca, Mg, and Al. To our knowledge, the effects of each of

these impurities on the microstructure and electronic properties of CZTS films have not been studied systematically.

Perhaps one of the reasons why there has been little research into the individual effects of the impurity atoms in CZTS is that there are few convenient *and* controllable methods of delivering impurities to the film. While Li *et al.* evaporated layers of NaF onto the CZTS film to introduce additional impurities, this controllable method requires an evaporation system. The method of dipping a precursor film into an Na_2S solution, as proposed by Hliang Oo *et al.*,is an arguably convenient method, though it is not entirely controllable.

Herein we present an investigation of the effect of each of the impurities present in SLG on the microstructure of thin CZTS films synthesized through sulfidation of co-sputtered Cu-Zn-Sn alloy films. This investigation revealed that while numerous impurities in SLG can diffuse into the CZTS films, only Na and K diffusion affects the film morphology. Surprisingly, we also found that impurities can be transported through the vapor phase to CZTS films on a variety of substrates from a piece of SLG placed near the films within the sulfidation vessel. Based on this vapor transport mechanism, we developed an approach for delivering precisely controlled amounts of specific impurities into CZTS films on arbitrary substrates. We believe that this approach will assist the development of high efficiency CZTS solar cells on substrates other than SLG.

4.2 Experimental

CZTS films were synthesized *via ex situ* sulfidation of 430 nm thick Cu-Zn-Sn alloy films. The metallic precursor films were co-sputtered from Cu/Zn (35 at% Cu) and Cu/Sn (60 at% Cu) targets at 10 mTorr using Ar as the working gas with a chamber base pressure of 2×10^{-7} Torr. Precursor films were deposited on SLG, 7740 Corning glass (Pyrex), and z-cut crystalline quartz substrates. Compared to SLG and Pyrex, the quartz substrate is of very high purity and was chosen as a control substrate. The elemental compositions of the SLG and Pyrex substrates were determined using inductively coupled plasma mass spectrometry (ICP-MS) and are presented in Table 4.1. In addition

to Si and O, SLG and Pyrex host a variety of impurities. Within SLG the most prevalent impurity is Na, comprising nearly 9 at% of the glass, followed by Ca and Mg at 4.4 and 3.4 at% respectively, as well as very small amounts of K. Pyrex has a decidedly lower impurity content, with B and Na making up 3.9 at% and 2.6 at% of the glass, respectively.

Table 4.1 Typical elemental composition of SLG and Pyrex substrates as determined from ICP-MS.

Element	SLG (%)	Pyrex (%)	Element	SLG (%)	Pyrex (%)
Al	0.25	0.52	Na	9.0	2.64
B	0	3.85	P	0.002	0
Ba	0.001	$<10^{-3}$	Si	23.4	28.2
Ca	4.36	0.15	Sr	0.001	$<10^{-4}$
Fe	0.01	0.006	Ti	0.011	0.003
K	0.07	0.008	Zr	$<10^{-3}$	0.013
Mg	3.41	0.004	O	59.5	64.5
Mn	0.01	$<10^{-3}$			

Following deposition, the Cu-Zn-Sn precursor films were sealed in an evacuated quartz ampoule (base pressure of 10^{-6} Torr) with ~ 1 mg of solid S. This ampoule, containing the film and S, was placed in a box furnace and heated at a rate of 6.5 ^{o}C/min to 600 ^{o}C. The precursor films were sulfidized isothermally at 600 ^{o}C for 8 hours before cooling the ampoule back to room temperature naturally. Upon sulfidation, 430 nm thin Cu-Zn-Sn precursor films were transformed into ~2.2 µm thick CZTS films. The films were removed by breaking the ampoules and characterized using a battery of methods including x-ray diffraction (XRD), confocal Raman scattering microscopy, scanning electron microscopy (SEM), and energy dispersive x-ray spectroscopy (EDS). Specifically, XRD patterns of sulfidized films were collected using a Bruker D8 Discover

system equipped with a Cu $K\alpha$ x-ray source, 0.8 mm beam collimator, and a Hi-Star 2D area detector. Raman spectra were collected at room temperature using a WiTec alpha300R confocal Raman microscope equipped with a UHTS300 spectrometer and a DV401 CCD detector, and the films were illuminated with an Omnichrome Ar ion laser (514.5 nm, ~300 nm beam spot size). Raman scattering was collected in a backscattering geometry and dispersed with an 1800 lines/mm grating, resulting in a spectral resolution of 0.02 cm^{-1}. The morphology and spatially averaged elemental composition of the sulfidized films were examined using a JEOL 6500 SEM equipped with a Thermo-Noran Vantage EDS detector. The electron energy was set at 15 keV both for imaging and EDS measurements. At this energy the EDS probe depth is estimated to be near 2 µm, ensuring that the entire depth of the sulfidized films was examined. The average grain size of the CZTS films was determined from SEM images by averaging the number of grains along randomly chosen lines. At least 100 grains were sampled for each film.

The intentional introduction of Na, K, and Ca was performed by coating the quartz tubes with aqueous solutions of NaOH, KOH, and $Ca(OH)_2$. The NaOH solution was diluted from a purchased stock solution, while KOH and $Ca(OH)_2$ solutions were made by dissolving solid KOH and $Ca(OH)_2$ in DI water. The solutions were all of known molarity so a measured volume had a known quantity of NaOH, KOH, or $Ca(OH)_2$. Typically ~ 1 mL of solution was added to the quartz tube, and the tube was then allowed to dry vertically in a convection oven heated to 100 ^oC. Once the tube was dried, the precursor film and S were loaded and the sulfidation proceeded normally.

4.2.1 Detailed SIMS Description

Time-of-flight secondary ion mass spectrometry (TOF SIMS) depth profiling was conducted in single-beam mode in SARISA,[13, 14] a custom designed analytical instrument capable of operating as a laser post-ionization secondary neutral mass spectrometer (LPI SNMS) and as TOF SIMS. The 10 keV Ar^+ beam was used in a sequence of alternating cycles, that consisted of milling in a direct-current (dc) raster-scanned mode followed by elemental TOF SIMS analysis in a pulsed mode without raster scanning. The Ar^+ ion

beam was produced by an Atomika WF421 ion gun equipped with a Wien filter, two pairs of electrostatic deflectors for scanning, and another pair for pulsing. The ion gun was pointed at the sample at 60° from the sample surface normal. Pulse duration was set to 200 ns, the shortest duration possible with SARISA's pulsing electronics. Even though 200 ns pulse may result in decreased mass resolution in most TOF SIMS instruments, this was not the case in SARISA, which was designed to operate with long primary ion pulses (≈ 1μs, typical for LPI SNMS) and maintain high mass resolving power.[15] When performing sputter depth profiling analysis with primary ions of inert gases, a long primary ion pulse was followed with delayed extraction of secondary ions thus enabling high sensitivity to secondary ions such as O^+ and S^+. A 500×500 μm^2 surface area was ion milled in the raster-scanned mode. Elemental composition information was collected from a ≈30 μm spot in the center of the 500×500 μm^2 crater. This estimate of the analytical spot size (30 μm) corresponds to the width of the Gaussian-shaped ion beam profile close to its base. The analytical beam size (at 10 keV energy and 60 nA dc current) was found to have a symmetric Gaussian distribution with a FWHM of ~15 μm by burning dents in silicon and profiling the dents using white light interferometry (WLI).[16] Including the primary ions within the tails of the analytical beam profile averages the secondary ion intensity over a larger area and across many CZTS grains. Averaging over a 30 μm spot was necessary because CZTS grains were several microns in some films. The size of the beam was controlled *in situ* using a Schwarzschild type microscope and measured before and after depth profiling.[17] WLI was also used to measure some of the craters within the CZTS films after depth profiling to confirm both the lateral size and depth of the crater from which material was removed. All profiles were measured with a 60 nA dc current beam, a current high enough to mill through a ~2 μm thick sample in a reasonable amount of time and to have sufficient dynamic range for detecting secondary ion species within broad mass range (from ^{10}B to ^{122}Sn). The ion beam current was measured *in situ* by a custom graphite Faraday cup consisting of an internal pin (60°, 250 μm diameter inlet hole) and the external surface. This design provides coarse control over the ion beam focusing conditions by measuring internal and

external components of the ion current. The Faraday cup could be positioned accurately and reproducibly at the same location as the sample surface with respect to the ion optics of the mass spectrometer and the Atomika ion gun. Each film was depth profiled at least twice at different locations to ensure the reproducibility of the results.

4.2.2 Description of Quantification of the impurity concentrations using Saha-Eggert analysis

The Na, K and Ca SIMS intensities were converted to their respective atomic concentrations, using the Saha-Eggert approach. The Saha-Eggert method does not require calibration standards. Instead, it relies on the correlation between the secondary ion yields and the ionization potentials of elements to quantify trace amounts of low concentration species (*e.g.,* impurities) with respect to the composition of a host matrix with known stoichiometry (*e.g.,* Cu_2ZnSnS_4). It was first introduced for SIMS analysis with oxygen as the primary ions[17] and expanded later to SIMS analysis with Ar ions.[18] Central to this analysis is the Saha-Eggert ionization plot which correlates the SIMS intensity of an element *i* to its ionization potential, I_{pi}, by assuming that its secondary ion emission yield, γ_i, from a multinary solid host is given by

$$\gamma_i \propto \exp\left(-\frac{I_{pi}-\delta\varepsilon}{kT}\right) \tag{4.1}$$

where k is the Boltzmann's constant, T is the temperature and $\delta\varepsilon$ is an adjustable parameter that accounts for the work function and the lowering of energy barriers on the surface due to plasma effects. Assuming the SIMS intensity to be proportional to the secondary ion yield and the atomic concentration of species *i*, i.e.,

$$S_i \propto \gamma_i x_i, \tag{4.2}$$

a semi-logarithmic plot of the weighted SIMS intensity, S_i/x_i, vs. the ionization potential, I_{pi} should be linear. Such a line can be generated from the known stoichiometry of the host (*e.g.,* Cu, Zn, Sn and S concentrations in CZTS) and then used to infer the unknown concentrations of impurities. For example, Figure S1 shows this Saha-Eggert plot for

CZTS. Figure 4.1 was generated by plotting, the SIMS intensities of Cu, Zn, Sn and S divided by their concentrations as measured by EDS (Table 4.2) versus their respective ionization potentials. The dotted line is the best fit to the data and represents the dependence expected from equation 1. Intensity of any other impurity element lying on the dotted line would mean that its relative concentration is on the order of the four matrix elements, i.e. ≈10 at%. Thus, the atomic concentration of an impurity, *i*, can be calculated from

$$x_i = \frac{S_i}{(S/x)\big|_{Ipi}}, \qquad (43)$$

where S_i is the measured SIMS signal intensity and $(S/x)\big|_{Ipi}$ is the value of the weighted SIMS signal intensity at the ionization potential of the species *i*, on the dashed line in Figure 4.1.

To estimate the concentration levels of various impurities, we used the averaged SIMS intensities below $d/d_o \leq 0.4$. For example, Si^+ SIMS intensity of ~0.1 corresponds to ~1 at. % Si within the film, approximately the same as that obtained, independently and reproducibly, from EDS measurements. The ionization potential for Si is in the range covered by the ionization potentials of Cu, Zn, Sn and S. However, an extrapolation is necessary for K, Na and Ca. The average (between the surface and $d/d_o \leq 0.4$) atomic concentrations of Si, Na, K, and Ca in the CZTS films synthesized on various substrates were calculated and the results are listed in Table 4.3.

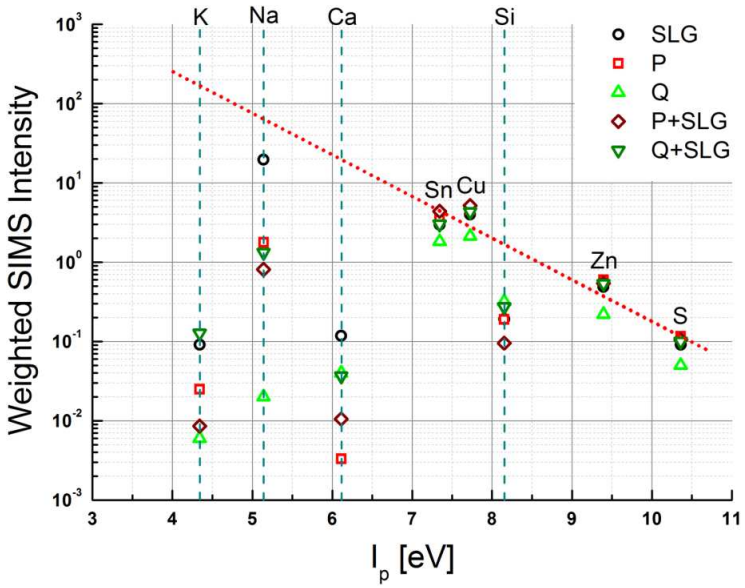

Figure 4.1The Saha-Eggert semi-log plot for the CZTS films. Red solid line is the fit to the data for Cu, Zn, Sn and S, Red dashed line is extrapolation of this line to the region of the ionization potentials for Ca, K and Na.

4.3 Results and Discussion

A detailed study of the evolution of microstructure in films deposited on different substrates revealed a significant surprise. Specifically, we found overwhelming evidence that impurities from the SLG have a remarkable effect on the final grain size. Figure 4.2 shows plan-view (top row, a, c & g) and cross-sectional (bottom row, b, d & h) SEM images of CZTS films synthesized on SLG (a & b), quartz (c & d), and Pyrex (g & h). A comparison between these SEM images reveals the striking difference in their microstructure. All these films were synthesized under identical conditions, and XRD and Raman spectroscopy indicate that they are all nominally stoichiometric CZTS (*vide infra*).

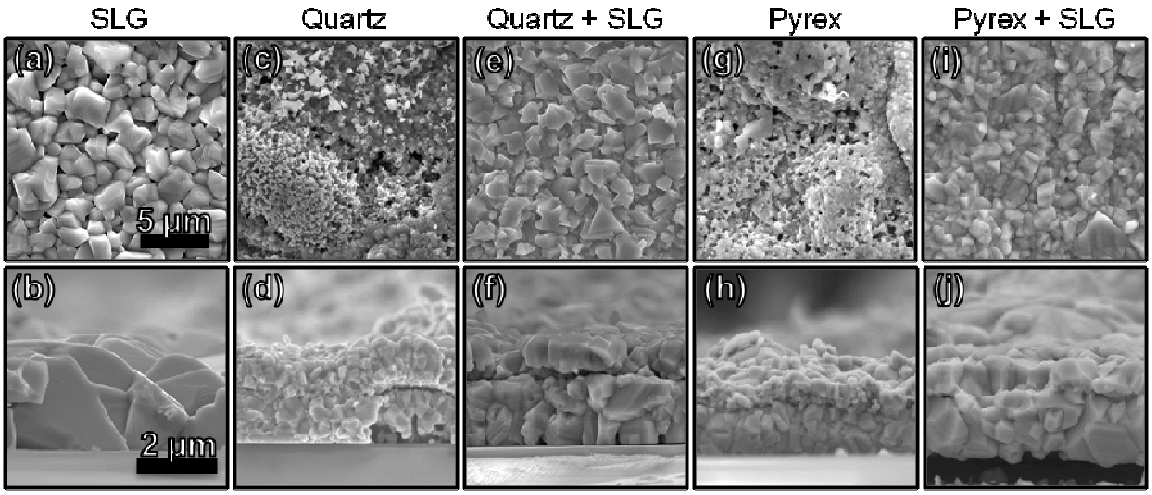

Figure 4.2 Plan-view (a, c, e, g & i) and cross-sectional view (b, d, f, h & j) SEM images of CZTS films synthesized through sulfidation at 600 ^{o}C, on SLG (a-b), quartz (c-f) and Pyrex (g-j). During the synthesis of films shown in e & f an uncoated piece of SLG was placed in the sulfidation ampoule with the Cu-Zn-Sn films on quartz. Similarly, during the synthesis of films shown in i & j an uncoated piece of SLG was placed in the sulfidation ampoule with the Cu-Zn-Sn films on Pyrex.

The CZTS film synthesized on SLG is continuous with an average grain size of 1.38 ± 0.15 μm. Essentially, this film is comprised of a monolayer of micrometer size CZTS grains, a highly desirable microstructure for solar cells. On the other hand, films synthesized on quartz and Pyrex have significantly smaller grains. In fact, when viewed from the top, individual grains are not even clearly distinguishable. Cross-sectional SEM images (Figures 4.2d and 4.2h) reveal that CZTS films on both quartz and Pyrex have a bilayer structure with grains that do not extend through the entire depth of the film: multiple layers of small grains are visible through the film thickness. In the film on Pyrex, the layer adjacent to the substrate has a larger, better defined grain structure with an average grain size of 0.47 ± 0.05 μm, while the film surface region, (i.e. away from the substrate) has an average grain size of 0.35 ± 0.03 μm. Such a difference is not obviously visible in films synthesized on quartz. The layer nearest the substrate in the film on quartz has an average grain size of 0.34 ± 0.07 μm, while the surface layer has an average grain size 0.31 ± 0.04 μm.

These differences in microstructure could be due to differences in substrate crystallinity, thermal expansion coefficients, or impurity concentrations in the various substrates. To clarify the origins of these differences, we conducted experiments on various substrates to evaluate these possibilities and have concluded categorically that the differences in microstructure and grain size are due to impurities diffusing into the CZTS from the substrate. Firstly, the microstructure of CZTS films found on single crystal quartz is similar to that grown on fused amorphous quartz, which rules out effects due to crystallinity. Secondly, Pyrex and SLG have similar thermal expansion coefficients but the microstructures of CZTS grown on Pyrex and SLG are very different. Finally, two additional experiments, the results of which are also shown in Figure 4.2, provide unambiguous evidence that impurities are responsible for the larger CZTS grains observed on SLG. In the first of these experiments, identical Cu-Zn-Sn precursor films on quartz were sulfidized with (Figure 4.2 e & f) and without (Figure 4.2 c & d) a bare piece of SLG placed in the sulfidation ampoule. The SLG was placed in close proximity to the precursor metal film but the two pieces were not in direct contact. Remarkably, the grain sizes in CZTS films sulfidized on quartz with this additional piece of SLG in the ampoule are dramatically larger (1.22 ± 0.16 μm, see Figure 4.2 e & f) than the grain sizes (~ 0.3 μm) in CZTS films sulfidized without the SLG in the ampoule (Figures 4.2 c & d). A similar result is obtained when comparing Cu-Zn-Sn films deposited on Pyrex (Figures 4.2 g & h) to CZTS films synthesized on Pyrex with SLG in the ampoule (Figure 4.2 i & j). A greater than two-fold increase in the average grain size on Pyrex was observed, from ~ 0.40 μm to 0.92 ± 0.08 μm, when a piece of SLG was present in the ampoule. Rather surprisingly, it appears that impurities are transported from the SLG substrate placed in proximity to the precursor film, through the vapor phase, to the CZTS film, where they enhance grain growth.

With the exception of the film on SLG, the CZTS films appear to be “phase-pure” within the limits of detection for XRD and Raman spectroscopy. Figure 4.3 reveals that XRD patterns collected from all the films are consistent with CZTS. The presence of the three CZTS diffraction peaks[19] at 37.0° [(202)], 37.9° [(211)], and 44.9° [(105) and

(213)], which are absent in ZnS and very weak in tetragonal Cu_2SnS_3, confirm the presence of CZTS. Interestingly, XRD pattern of CZTS synthesized on SLG also includes weak diffraction peaks at 29.0°, 26.4°, and 19.2°, matching the strongest peak locations of $Cu_{39}S_{28}$ (605), Na_2S_5 (012), and $NaCu_5S_3$ (101), respectively. These phases do not constitute a significant fraction of the sample volume however as their minor diffraction peaks are absent from the XRD pattern. Indeed, we observed infrequent but large grains (~ 10 µm in size) of impurity phases in plan-view and cross sectional SEM images. These impurity phases appeared to be limited to the surface of the CZTS films, and EDS analysis revealed they contained Na, Cu, S, and Sn, but always lacked Zn.

The Raman spectra from the films displayed in Figure 4.2 are shown in Figure 4.4. The major CZTS Raman peak [20,21] between 333 cm^{-1} and 338 cm^{-1} is present in all the spectra and is accompanied by a broad weaker scattering feature at 288 cm^{-1} that is also characteristic of CZTS films.

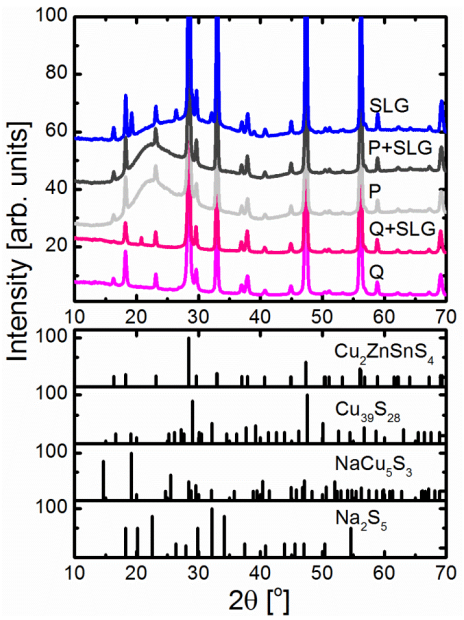

Figure 4.3 XRD from films sulfidized on SLG, Pyrex and quartz (top panel) at 600 °C. The bottom panels show the expected powder diffraction patterns from CZTS and the secondary impurity phases (Cu39S28, NaCu5S3, and Na2S5) encountered in the films for comparison. Q+SLG and P+SLG indicate the films that were synthesized on quartz and Pyrex, respectively, with a bare piece of SLG present in the sulfidation ampoule.

No other peaks were detected from films synthesized on quartz and Pyrex regardless of whether a bare piece of SLG was present or absent in the ampoule. In contrast, Raman spectra, from films synthesized on SLG, revealed regions with intense scattering at 297 cm^{-1} (Figure 4.4, spectrum labeled SLG II). These regions corresponded to the impurity phases observed with XRD, SEM and EDS. Raman scattering from $Cu_{39}S_{28}$ and Na_2S_5 are expected at 474 cm^{-1} and 446 cm^{-1}, respectively.[22,23] To our knowledge, there is no published Raman scattering data on $NaCu_5S_3$. Thus, a possible assignment for the Raman scattering at 297 cm^{-1} is $NaCu_5S_3$. The presence of the Na containing impurity phases in films synthesized on SLG is likely due to higher concentrations of Na present in SLG compared to Pyrex and quartz. It is important to note that the films here are synthesized directly on SLG, without a Mo layer. In typical solar cell fabrication, a Mo layer is deposited on SLG as an electrical back contact, which slows and mediates Na diffusion. Lower Na concentrations in films synthesized on Mo-coated SLG compared to films synthesized directly on SLG may be the reason why these impurity phases have not been detected previously.

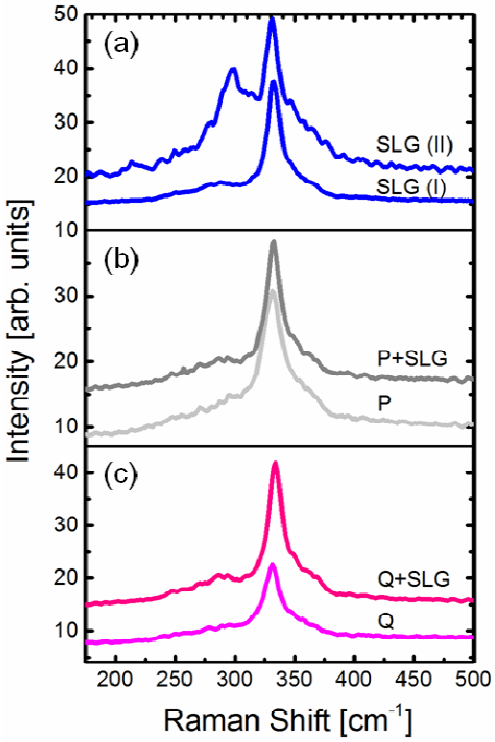

Figure 4.4 (a) Raman spectra from two different regions of the CZTS film synthesized on SLG. The spectrum labeled SLG (I) is representative of the majority of the film, while the spectrum labelled SLG (II) was collected from a location on the film where an impurity phase grain was present. Panels (b) and (c) show representative Raman spectra from CZTS films synthesized on (b) Pyrex (P) and (c) quartz (Q), with (P+SLG, Q+SLG) and without (P, Q) a bare SLG present in the sulfidation ampoule.

Table 4.2 lists the elemental compositions of the CZTS films as determined through EDS. Concentrations of impurities (*e.g.*, K, Ca, Mg, B, etc.) are too low to be accessible with EDS. Moreover, even for the highest concentration impurity, Na, close proximity of its *Kα* peak (1.041 keV) to the *Lα* peak of Zn (1.012 keV) makes compositional quantification difficult and inaccurate.

In order to monitor impurity concentrations below EDS detection limits, we used TOF-SIMS to map the impurity concentration as a function of depth in the CZTS films. During TOF-SIMS measurements, complete mass spectra were recorded at each depth revealing the presence of Na, K, Ca, Mg, B, and Si, albeit at different concentrations.

Table 4.2 The elemental composition, as determined by EDS, of CZTS films synthesized on (SLG), Pyrex (P) and Quartz (Q) with (P+SLG, Q+SLG) and without (P, Q) an additional piece of bare SLG present in the sulfidation ampoule.

Substrate	Cu(%)	Zn(%)	Sn(%)	S(%)
SLG	25	11	14	50
P	28	11	13	48
Q	27	11	14	48
P+SLG	27	11	14	48
Q+SLG	27	13	13	47

Figure 4.5 shows the profiles of Na, K, Ca, Mg, B, and Si as a function of normalized depth for all CZTS films displayed in Figure 4.2. The TOF-SIMS intensity for each element is proportional to its local concentration in the film and, hereafter, SIMS intensity and concentration are used interchangeably. We estimated the absolute Na, K, Ca and Si concentrations in the films from the SIMS intensities using the Saha-Eggert approach. Table 4.3 shows the Na, K, Ca and Si concentrations determined from the average SIMS intensities between the surface and d/d_o=0.4, where d/d_o is the normalized film depth. The film thickness, d_o, was determined from cross-sectional SEM images (i.e. Figure 4.2). The location of the CZTS-substrate interface was determined from the significant charging that takes place when the glass substrate is exposed to the sputtering beam and from the ensuing precipitous drop in SIMS intensities. This location corresponds to the normalized depth of d/d_o = 1 in Figure 4.5. The concentrations of Cu, Zn, Sn, and S, the major components of the CZTS film, were nearly identical to each other and were uniform throughout the films' depth, shown in Figure 4.6

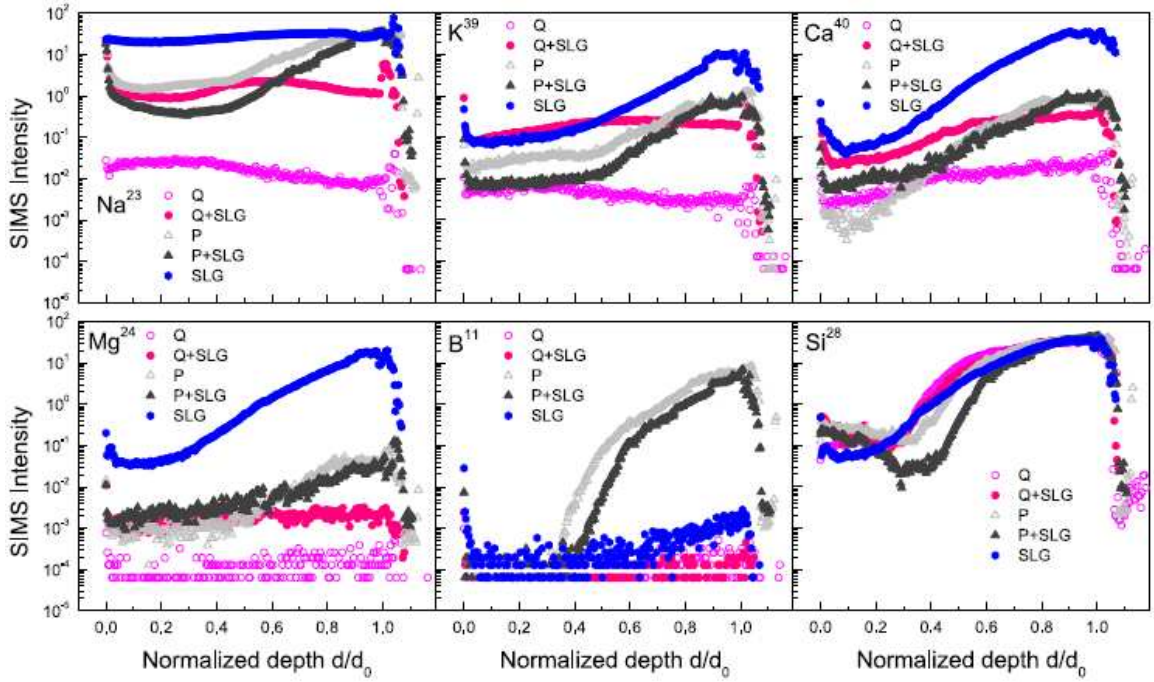

Figure 4.5The TOF-SIMS depth profiles for Na, K, Ca, Mg, B and Si in CZTS films synthesized on soda lime glass (SLG), Pyrex (P) and quartz (Q), with (P+SLG, Q+SLG) and without (P, Q) a bare SLG present in the sulfidation ampoule. The SIMS intensity is shown in per primary ion pulse.

The CZTS film synthesized on quartz acts as a control sample for TOF-SIMS characterization since quartz does not contain any of the impurities present in SLG and Pyrex. The impurity levels detected in CZTS films synthesized on quartz thus form the baseline for the TOF-SIMS data collected from films on other substrates. Indeed, for B and Mg, the TOF-SIMS intensities are at the noise level of the instrument. However, we detect Na, K and Ca even in films synthesized on quartz. These elements are ubiquitous and can be incorporated into the CZTS films during any of the steps in the synthesis process. Using the Saha-Eggert method, we calculated that Na, K, and Ca concentrations are $3x10^{-3}$, $3x10^{-4}$, and $2x10^{-3}$ at%, respectively. The Si TOF-SIMS intensity begins to increase at $d/d_o \approx 0.4$ for all films due to partial exposure of the substrate to the TOF-SIMS probing beam. This is likely due to a combination of surface roughness and voids within the film, which may be further exacerbated by ion bombardment. Moreover, during the analysis of films synthesized on Pyrex, the depth at which the Si intensity

begins to increase is identical to the depth at which the B intensity begins to rise. This is strong evidence that this rise is due to the onset of direct substrate probing by the TOF-SIMS analysis ion beam. Indeed, top view SEM images show that the substrate may be exposed through small voids between the grains.

Table 4.3The elemental composition, determined from SIMS intensities and Saha-Eggert analysis, of CZTS films synthesized on (SLG), Pyrex (P) and Quartz (Q) with (P+SLG, Q+SLG) and without (P, Q) an additional piece of bare SLG present in the sulfidation ampoule.

Substrate	Na(%)	K(%)	Ca(%)	Si(%)
SLG	>4	5×10^{-3}	6×10^{-2}	1
P	3×10^{-1}	1×10^{-3}	2×10^{-3}	1
Q	3×10^{-3}	3×10^{-4}	2×10^{-3}	2
P+SLG	1×10^{-1}	6×10^{-4}	5×10^{-3}	5×10^{-1}
Q+SLG	2×10^{-1}	8×10^{-3}	2×10^{-2}	2

The Na, K, Ca and Mg concentrations in the CZTS film synthesized on SLG were two to four orders of magnitude higher than those in films synthesized on quartz. Clearly, Na, K, Ca and Mg from SLG easily diffuse into the CZTS films, some of which are responsible for the enhanced grain growth on SLG. In fact, the relative atomic composition of Na is greater than 4 at%, while K and Ca compose $5x10^{-3}$ and $6x10^{-2}$ at% of the film respectively. The significant amount of Na is not entirely surprising since Na containing secondary phases were observed on the surface of this film by EDS and by XRD. The shape of the concentration profile is consistent with the substrate acting as a source for these impurities, with some of the concentration rise after $d/d_o \approx 0.4$ caused by the substrate becoming exposed to the probing ion beam through the voids between the grains.

The TOF-SIMS concentration profiles of Na, Ca, Mg, and K in CZTS films synthesized on Pyrex are similar to those in films synthesized on SLG, but the SIMS intensities from films on Pyrex are reduced by an amount commensurate with the lower

impurity levels found in Pyrex by ICP-MS. The relative percentage of Na, K, and Ca are $3x10^{-1}$, $1x10^{-3}$, and $2x10^{-3}$ at%, respectively. These numbers are considerably higher than those for the CZTS film on quartz. Boron is ruled out as an impurity that can affect the grain size, as the grain sizes of CZTS on Pyrex are small despite the fact that the B concentration is highest in films grown on Pyrex. Additionally, the largest grains are observed on SLG, which contains essentially no B compared to Pyrex.

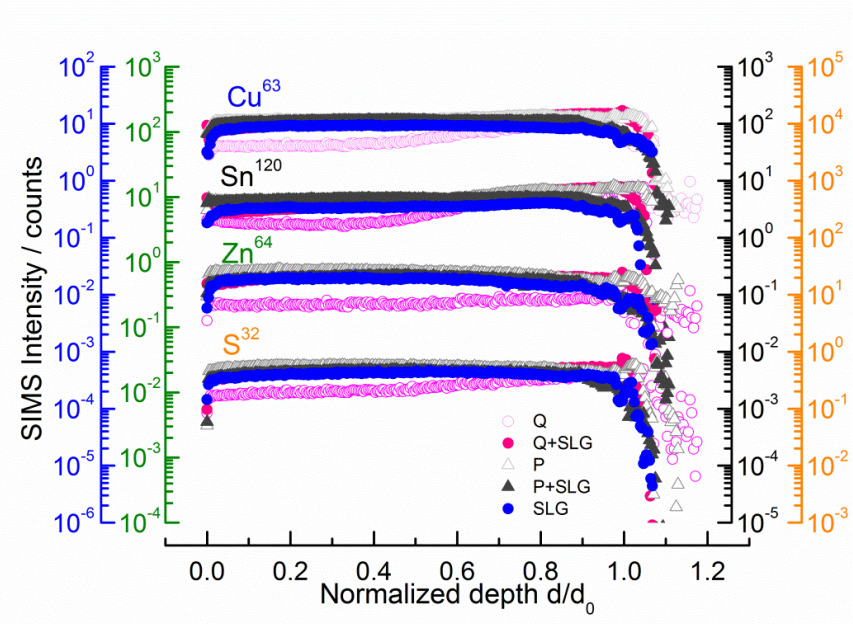

Figure 4.6 The SIMS intensity depth profiles for Cu, Zn, Sn and S in CZTS films synthesized on soda lime glass (SLG), Pyrex (P) and quartz (Q), with (P+SLG, Q+SLG) and without (P, Q) a bare SLG present in the sulfidation ampoule.

The CZTS films sulfidized on quartz with an additional piece of bare SLG in the ampoule show significantly elevated concentrations of Na, K and Ca as compared to the CZTS films sulfidized on quartz without the SLG. This remarkable observation confirms that Na, K and Ca are *transported via* the vapor phase from the SLG to the CZTS film on quartz. In fact, K and Ca concentrations in the film synthesized on quartz with the additional piece of SLG are nearly as high as those in the film synthesized directly on SLG (Table 4.3). The Na concentrations in the film synthesized on quartz with SLG in

the ampoule falls between the Na levels in films synthesized on quartz and on SLG. The Saha-Eggert analysis shows that Na, K, and Ca now make up $2x10^{-1}$, $8x10^{-3}$ and $2x10^{-3}$ at% of the film respectively. The grain size in films synthesized on quartz with SLG in the ampoule (1.22 ± 0.16 μm) is nearly as large as that in films synthesized on SLG (1.38 ± 0.15 μm) even though the Na concentration in the former is more than one order of magnitude lower than in the latter. This indicates that even very small amounts of impurities may be effective in enhancing grain growth. The concentration profiles of Na, K and Mg are also nearly flat, which is consistent with these impurities incorporating into the film uniformly from the vapor phase during sulfidation.

With the exception of a few subtle differences, the Na, K, Ca and Mg concentration profiles in the CZTS film sulfidized on Pyrex with an additional piece of bare SLG in the ampoule are very similar to those in the film sulfidized without the SLG. The subtle differences, however, give important insights. First, the Na and K concentration in the film grown on Pyrex without SLG in the ampoule is slightly larger (≈2×) than the Na and K concentration in the film grown with the SLG. This is unexpected since SLG provides an additional source of Na and K. Careful examination of Figures 4.2h and 4.2j shows that the average grain size in the film grown with SLG in the ampoule (0.92 ± 0.08 μm) is larger than the grain size in the film grown without the SLG (0.47 ± 0.05 μm). This suggests that Na and K may be in the grain boundaries, as a lower Na and K concentration would be expected in the film with the larger grains. Indeed, it is well known that Na in CIGS segregates to grain boundaries.[26-28] We also note that high levels of Na and K *within* the film do not necessarily correlate with a coarse-grained microstructure, but it is rather the concentration of Na and K that the film is exposed to during sulfidation that leads to the large grained microstructure. Indeed, the film grown with SLG in the ampoule is clearly exposed to higher impurity concentrations than the film sulfidized without SLG. The increased grain size near the substrate in films on Pyrex sulfidized without SLG also supports this conclusion, as the local concentration of impurities is highest near the substrate-film interface. Furthermore, we can rule out Mg as the impurity responsible for enhancing the grain growth. The Mg concentration in the

film synthesized on quartz with SLG in the ampoule is barely above the noise level (similar to the films grown on Pyrex with or without the additional SLG in the ampoule), and yet the average grain sizes in these films are very different.

In summary, three important conclusions emerge from the experiments discussed so far. First, Na, K, and/or Ca from SLG diffuse into CZTS films and enhance grain growth. Second, the impurities in SLG, particularly Na, K and Ca, are volatilized at 600 ^{o}C in a S atmosphere and are transported *via* the vapor phase to films placed in close proximity. Third, the *concentration* of impurities that the film is exposed to (*e.g.*, by diffusion from the substrate or from the vapor phase) determines the amount of grain growth, rather than the amount of Na or K within a film itself.

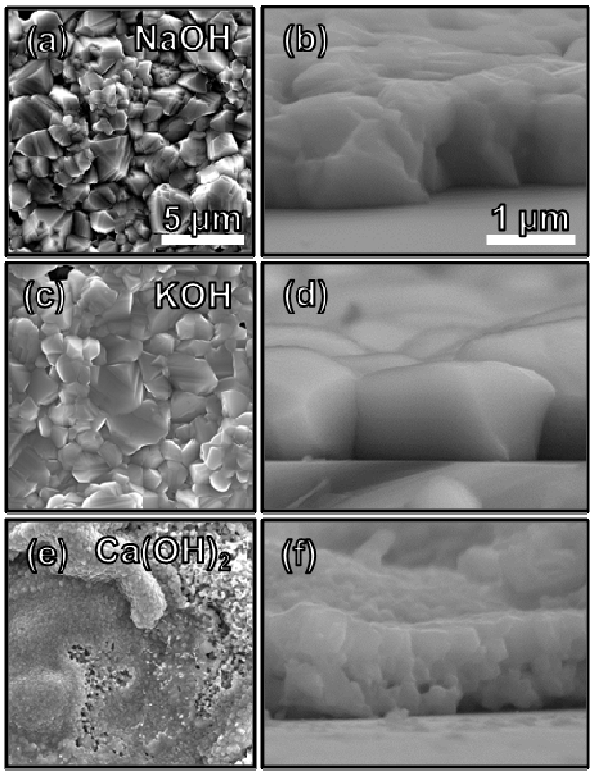

Figure 4.7 Plan view and cross sectional SEM images of CZTS films synthesized on quartz at 600 ^{o}C with (a & b) 1 µmole NaOH, (c & d) 0.1 µmol of KOH, and (e & f) 50 µmol of Ca(OH)2 charged into the sulfidation ampoule. Same scale bar applies for all plan view and cross sectional images respectively.

Inspired by the finding that alkali and alkaline earth metals in SLG can be volatilized and transported through the vapor phase, we developed a controlled method to introduce these impurities into CZTS films during sulfidation. Specifically, we introduced Na, K and Ca into CZTS films, one species at a time, by coating the inner walls of the ampoules used for sulfidation with dilute aqueous solutions of NaOH, KOH or $Ca(OH)_2$ (more details may be found in the experimental section). We varied the amounts of Na, K and Ca charged into the sulfidation ampoule over several orders of magnitude. The ranges tested included 95 μmol to 0.006 μmol of NaOH, 50 μmol to 0.003 μmol of KOH, and 50 μmol to 0.04 μmol of $Ca(OH)_2$. Using this approach, CZTS films were synthesized by sulfidizing Cu-Zn-Sn precursor films on quartz. Indeed, even when small amounts of Na and K were included in the sulfidation ampoule, the grains grew to sizes as large as those observed in films synthesized on SLG. Figures 4.7a, 4.7b, and 4.7c show the SEM images of CZTS films synthesized with 1 μmol NaOH, 0.1 μmol of KOH, and 50 μmol of $Ca(OH)_2$ charged into the sulfidation ampoule, respectively. The X-ray diffraction and Raman spectra collected from these films may be found in Figures 4.8 and 4.9 respectively.

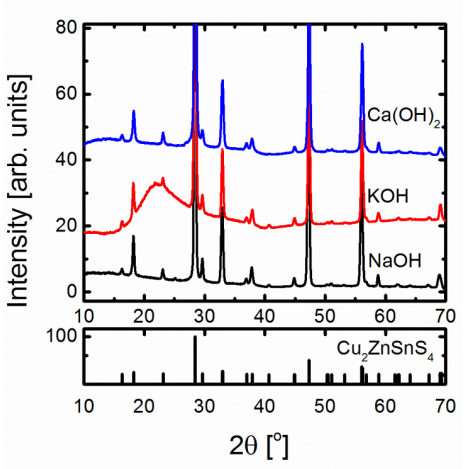

Figure 4.8 XRD from films sulfidized on quartz at 600 °C in an ampoule whose inside walls were coated with 50 μmol of Ca(OH)2, 0.1 μmol of KOH, and 1 μmol of NaOH (top panel). The bottom panel shows the expected powder diffraction patterns from CZTS. All samples were grown on quartz, however nominally impurity free quartz was used for the KOH sample. This is the cause of the amorphous background between 2θ = 20 and 30°

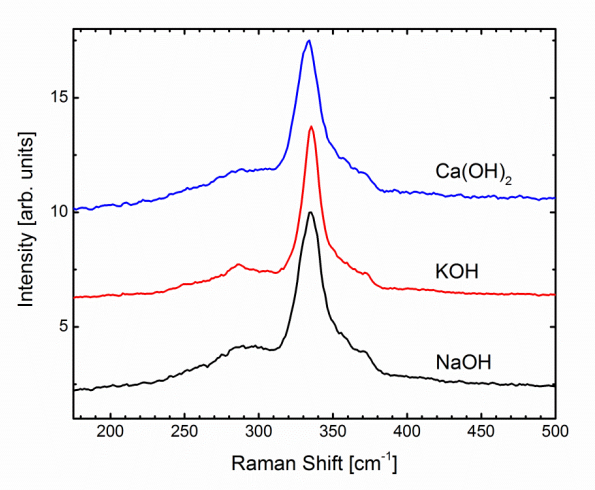

Figure 4.9 Raman spectra collected from films sulfidized on quartz at 600 oC in an ampoule whose inside walls were coated with 50 µmol of Ca(OH)2, 0.1 µmol of KOH, and 1 µmol of NaOH (top panel). The most intense peak, near 334 cm^{-1}, is consistent with CZTS.

Remarkably, the addition of 1 µmol of NaOH or 0.1 µmol of KOH in the sulfidation ampoule resulted in CZTS films with an average grain size of 1.26 ± 0.10 µm or 1.31 ± 0.18 µm, respectively. If the charge of NaOH or KOH was too high, the film was no longer continuous and Na and K containing impurity phases dominated the film, shown in Figure 4.10. Conversely, if the NaOH and KOH charges were too small, no enhanced grain growth was observed. While the volatile species that transport Na and K to the CZTS film is not known at this time, the vapor pressures of NaOH and KOH are very similar (66.5 and 84.9 mTorr, respectively, at 600 °C), and we thus do not expect this vapor pressure difference could lead to the 10 fold difference in the amounts required to achieve ≈1.3 µm grains. It appears that K is more efficient in enhancing the CZTS grain growth than Na in terms of impurity charge loading. Note that we did not observe any significant grain growth enhancement with Ca, even though we varied the amount of Ca charged into the sulfidation ampoule between 0.04 µmol and 50 µmol.

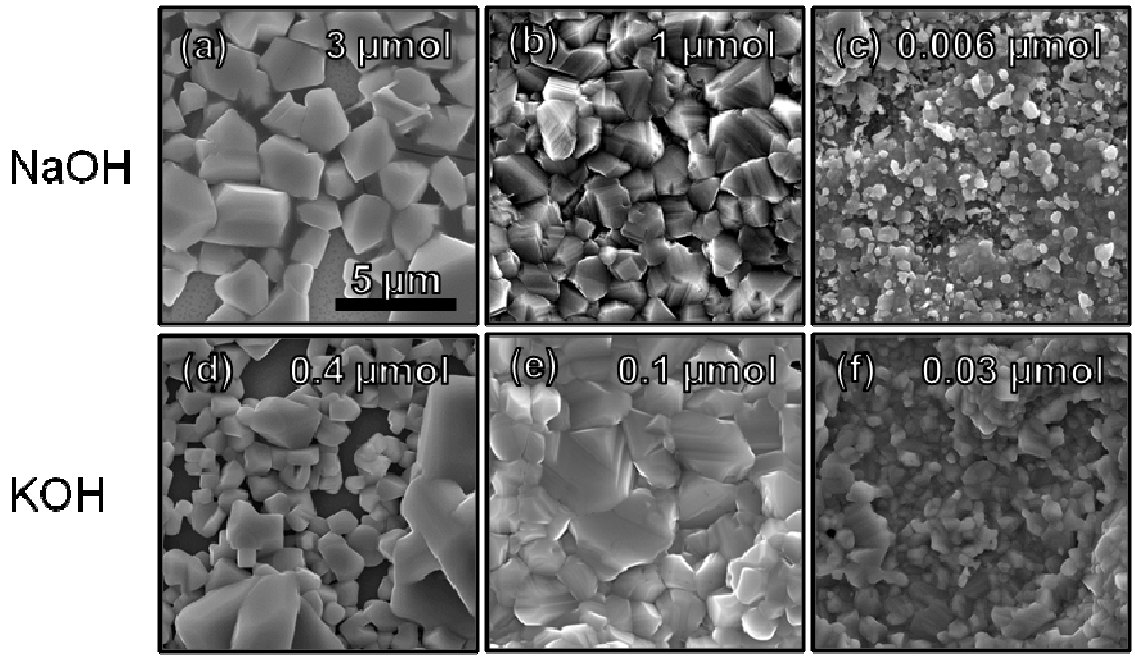

Figure 4.10 SEM images of films sulfidized on quartz at 600 ^{o}C in an ampoule whose inside walls were coated with different concentrations of NaOH and KOH. The moles of NaOH or KOH charged into the ampoule is shown in the upper right corner of each image. The films shown in (a) and (d) were comprised of many discontinuous large grains of CZTS along with large domains (10 - 20 µm) of impurity phases containing Na and K respectively.

These findings raise an obvious question: Precisely *how* do Na and K facilitate grain growth? One obvious possibility is that Na and K may segregate to grain boundaries where they act as fluxing agents that locally lower the melting point. Such lowering of the melting point at the grain boundaries could increase the mobility of the cations, and therefore accelerate grain growth. Another possibility is that Na- and K-containing impurity phases may be acting as intermediates for CZTS formation, thereby accelerating grain growth. The detection of Na- and K-containing phases when films are synthesized with high Na and K concentrations in the sulfidation ampoule suggests that such phases may exist in small amounts during sulfidation, even when the Na and K concentrations are low. These phases are expected to segregate to grain boundaries and may act as high mobility channels for transporting cations from small grains to larger ones during grain growth. Another possibility is that Na and K segregation to the grain

boundaries and surfaces alters the surface energy of the CZTS grains making grain growth significantly more energetically favorable. Ineffectiveness of Ca in grain growth enhancement, with the +2 oxidation state as compared to Na and K in the +1 oxidation state, could well be an important observation in this regard. Clearly, elucidating the mechanism of alkali-metal enhanced grain growth remains a challenge and will likely require a careful *in situ* investigation of the grain boundaries and surfaces during growth.

4.4 Conclusions

We studied the composition and microstructure of CZTS films synthesized on soda lime glass, Pyrex and quartz through sulfidation of co-sputtered Cu-Zn-Sn metal alloy precursor films. We found that Na and K diffusing from soda lime glass and Pyrex enhanced grain growth during the synthesis of CZTS films. CZTS films with large grains (>1 μm) could also be synthesized through vapor transport of Na and K from an uncoated piece of SLG placed inside the sulfidation ampoule. Inspired by this observation, we developed a method for delivering precisely controlled amounts of Na, K, and other alkali and group II metals to CZTS films during their synthesis. Using this method, we studied and delineated the effects of Na, K and Ca on the microstructure of CZTS films synthesized through sulfidation of Cu-Zn-Sn films. Even 1 μmol of Na was enough to enhance grain growth, and, remarkably, an order of magnitude less K (i.e. 0.1 μmol of K) achieved similar grain sizes.

4.5 References

1. T. K. Todorov, J. Tang, S. Bag, O. Gunawan, T. Gokmen, Y. Zhu and D. B. Mitzi, *Advanced Energy Materials*, **2013**, 3, 34–38.
2. H. Katagiri, K. Jimbo, W. S. Maw, K. Oishi, M. Yamazaki, H. Araki and A. Takeuchi, *Thin Solid Films*, **2009**, 517, 2455–2460.
3. I. Repins, C. Beall, N. Vora, C. DeHart, D. Kuciauskas, P. Dippo, B. To, J. Mann, W.-C. Hsu, A. Goodrich and R. Noufi, *Sol. Energ. Mat. Sol. C.*, **2012**, 101, 154–159.

4. M. Ruckh, D. Schmid, M. Kaiser, R. Schaffler, T. Walter and H. W. Schock, *Sol. Energ. Mat. Sol. C.*, **1996**, 41/42, 335–343.
5. T. Nakada, D. Iga, H. Ohbo and A. Kunioka, *Jpn. J. Appl. Phys.*, **1997**, 36, 732-737.
6. L. Kronik, D. Cahen and H. Schock, *Advanced Materials*, **1998**, 10, 31–36.
7. A. Rockett, Thin Solid Films, 2005, 480, 2–7.
8. D.-H. Cho, K.-S. Lee, Y.-D. Chung, J.-H. Kim, S.-J. Park and J. Kim, *Appl. Phys. Lett.*, **2012**, 101, 023901.
9. S. Ishizuka, A. Yamada, M. M. Islam, H. Shibata, P. Fons, T. Sakurai, K. Akimoto and S. Niki, S., *J. Appl. Phys*., **2009**, 106, 034908.
10. T. Prabhakar and N. Jampana, *Sol. Energ. Mat. Sol. C.*, **2011**, 95, 1001–1004.
11. W. M. Oo Hlaing, J. L. Johnson, A. Bhatia, E. A. Lund, M. M. Nowell, M. A. Scarpulla, *J. Electron. Mater.*, **2011**, 40, 2214–2221.
12. J. V. Li, D. Kuciauskas, M. R. Young and I. L. Repins, *Appl. Phys. Lett.*, **2013**, 102, 163905.
13. I.V. Veryovkin, C. E. Tripa, M. J. Pellin, *Physics Procedia,* **2008**, *1*, 379–389.
14. S. V. Baryshev, N. G. Becker, A. V. Zinovev, C. E. Tripa, I. V. Veryovkin, *Rapid Commun. Mass Sp*., **2013**, *27*, 2828-2832
15. I. V. Veryovkin, W. F. Calaway, J. F. Moore, M. J. Pellin, D. S. Burnett, *Nucl. Instrum. Meth. B*, **2004**, *219–220*, 473–479.
16. S. V. Baryshev, A. V. Zinovev, C. E. Tripa, R. A Erck, I. V. Veryovkin, *Appl. Surf. Sci.*, **2012**, *258*, 6963–6968.
17. C. A. Andersen, J. R. Hinthorne, *Anal. Chem.*, **1973,** *45* (8), 1421–1438.
18. F. Rüdenauer, W. Steiger, H. Werner, *Surf. Sci.*, **1976,** *54*, 553–560.
19. A.-J. Cheng, M. Manno, A. Khare, C. Leighton, S. Campbell and E. S. Aydil, *J. Vac. Sci. Technol. A,* **2011**, 29, 051203.
20. P. A. Fernandes, P. M. P. Salome and A. F. da Cunha, *Thin Solid Films*, **2009**, 517, 2519-2523.
21. F. Jiang, H. Shen, W. Wang and L. Zhang, *Appl. Phys. Express*, **2011**, 4, 074101.

22. P. Kumar and R. Nagarajan, *Inorg. Chem.*, **2011**, 50, 9204–9206.
23. O. El Jaroudi, E. Picquenard, N. Gobeltz, A. Demortier and J. Corset, *Inorg. Chem.*, **1999**, 38, 2917–2923.
24. C. A. Andersen and J. R. Hinthorne, *Analytical Chemistry*, **1973**, 45, 1421–1438.
25. F. Rüdenauer, W. Steiger and H. Werner, *Surface Science*, **1976**, 54, 553–560.
26. A. Rockett, J. S. Britt, T. Gillespie, C. Marshall, M. M. Al Jassim, F. Hasoon, R. Matson and B. Basol, *Thin Solid Films*, **2000**, 372, 212–217.
27. Braunger, D. Hariskos, G. Bilger, U. Rau and H. W. Schock, *Thin Solid Films*, **2000**, 362, 161–166.
28. W. Niles, M. M. Al-Jassim and K. Ramanathan, *J. Vac. Sci. Technol. A*, **1999**, 17, 291–296.

Chapter 5

The influence of stoichiometry, grain size, and Na addition on the electronic properties of Cu_2ZnSnS_4 thin films

5.1 Introduction

Copper zinc tin sulfide (Cu_2ZnSnS_4 or CZTS) is a promising candidate to be used as an inexpensive, earth abundant absorbing layer in thin-film solar cells. Power conversion efficiencies of solar cells made from CZTS have already reached 8.4 %.[1] Efficiencies of solar cells made from copper zinc tin sulfide selenide alloys ($Cu_2ZnSn[S,Se]_4$ or CZTSSe) where some of the S anions are replaced with Se are even higher and have rapidly increased to 12.6%.[2] Naturally, there is a tremendous interest in advancing our understanding of the fundamental electronic properties of CZTS and the factors that influence them. Specifically, electronic transport mechanisms and approaches to intentionally manipulate conductivities, carrier concentrations, and charge mobilities are still under investigation. Film synthesis and processing conditions have dramatic effects on the film properties such as stoichiometry, grain size, and impurity concentrations. These in turn affect the electronic transport and solar cell performance. Often, the interrelation between these properties are complex. For example, unintentional incorporation of group I metals such as Na and K through diffusion from the frequently used soda lime glass substrate into the film affects the grain size and possibly the charge carrier concentrations. Large grain size can in turn influence the charge mobility. Thus, it is often difficult to isolate the cause and effect to elucidate process-structure-property relations in making CZTS films and solar cells.

Many experimental studies have found and demonstrated that Cu-poor and Zn-rich CZTS layers result in the highest efficiency solar cells.[3–5] Theoretical studies using first principal calculations based on density functional theory have tried to rationalize this observation based on the changes in defect concentrations in the CZTS as a function of the cation composition. These calculations have shown that altering the cation

stoichiometry of the CZTS layer not only affects the phase composition (*i.e.*, leading to phase impurities such as $Cu_{2-x}S$, ZnS, SnS, Cu_2SnS_3), but also the concentrations of defects such as copper vacancies and various antisite defects.[5] For example, Chen *et. al.* studied how stoichiometry influences the presence of various defects and defect complexes that alter not only the local band edge positions of the CZTS layer, but also the charge carrier concentrations.[5] All reported CZTS films and single crystals have been *p*-type but a review of the literature, summarized in Figure 5.1, shows a wide spread in experimentally measured (through Hall effect) hole concentrations.[6–20] Films that are Cu-rich and Zn-poor tend to have the highest hole concentrations while films that are Cu-poor and Zn-rich tend to have the lowest, an observation consistent with theoretical predictions.[5] This observation is rationalized in terms of decreasing the ionized acceptor defect Cu_{Zn}^{-} concentration with decreasing Cu and increasing Zn concentrations. This defect is predicted be the dominant contributor to the hole concentration in the film and hence as the Cu concentration decreases, the overall hole density decreases. Orders of magnitude changes in carrier concentration with slight changes in stoichiometry is observed and such changes undoubtedly impact solar cell performance. While reasonably high carrier concentrations are desirable to decrease series resistances and lower the Fermi energy, a CZTS layer that has an exceptionally high carrier concentration will ultimately have a much narrower space charge region, resulting in inefficient collection of photogenerated carriers. Thus, the carrier concentration must be optimized through the Cu-to-Zn ratio. Empirical optimization so far has lead to the diffuse region in the composition parameter space shown in Figure 5.1.

Changes in the hole concentration are not the only consequence of varying CZTS stoichiometry, however, as self compensated defect clusters are also prone to form.[5] While these clusters do not contribute to carrier concentrations, they may have dramatic effects on local band fluctuations. Within the chemical potential bounds of phase pure CZTS, the three most prominent self compensated defect clusters are predicted to be $[2Cu_{Zn}^{-}+Sn_{Zn}^{2+}]$, present in high concentrations in Cu-rich Zn-poor films, and $[V_{Cu}^{-}+Zn_{Cu}^{+}]$ and $[Zn_{Sn}^{2-}+2Zn_{Cu}^{+}]$, present in high concentrations in Cu-poor Zn-rich films. In

Cu-rich Zn-poor films, the [$2Cu_{Zn}^{-}+Sn_{Zn}^{2+}$] complex decreases the conduction band edge by ~0.4 eV and increases the valance band edge by ~0.2 eV. These large local fluctuations may lead to higher carrier recombination rates in solar celles made from Cu-rich Zn-poor CZTS films. In Cu-poor Zn-rich films, the formation of [$V_{Cu}^{-}+Zn_{Cu}^{+}$] and [$Zn_{Sn}^{2-}+2Zn_{Cu}^{+}$] have a negligible effect on the local band edges. In summary, first principle calculations predict that stoichiometric inhomogeneities can affect the solar cell performance by altering both the hole concentrations and local band edges.

An unintentional consequence of building CZTS solar cells on soda lime glass is the introduction of metallic impurities, in particular group I metals such as Na and K, into the CZTS layer. These impurities in the CZTS film are expected to affect the solar cell performance. Recently, we have shown that when a soda-lime glass substrate is used, Na and K from the substrate will readily diffuse into the CZTS layer and enhance grain growth during synthesis,[21] and films grown on SLG have large grains. This grain growth enhancement can also be achieved by introducing Na and K in other ways, through vapor phase addition,[21] through NaF layers evaporated onto the substrate prior to CZTS layer formation,[22] and through aqueous Na_2S treatments.[23] As in $CuIn_xGa_{1-x}(S,Se)_2$ (CIGS),[24–26] solar cells, it appears that the addition of Na may also improve CZTS solar cell performance.[22,27] While the mechanism behind this improvement in CZTS solar cell performance is not known, in addition to grain growth enhancement, Na has been shown to passivate grain boundaries and eliminate defects.[28] In CZTS single crystals, the addition of Na has been correlated with increasing hole mobility and concentrations, as well as decreasing compensation.[29] These findings are similar to those in CIGS, where it has been shown that Na and K not only increase the grain size and improve the crystallinity of the CIGS films, but can also increase conductivity and hole concentrations.[30] Unfortunately, it has been nearly impossible to separate the affects of Na addition and increases in grain size, which may mask the role of grain boundaries in defect chemistry and transport.

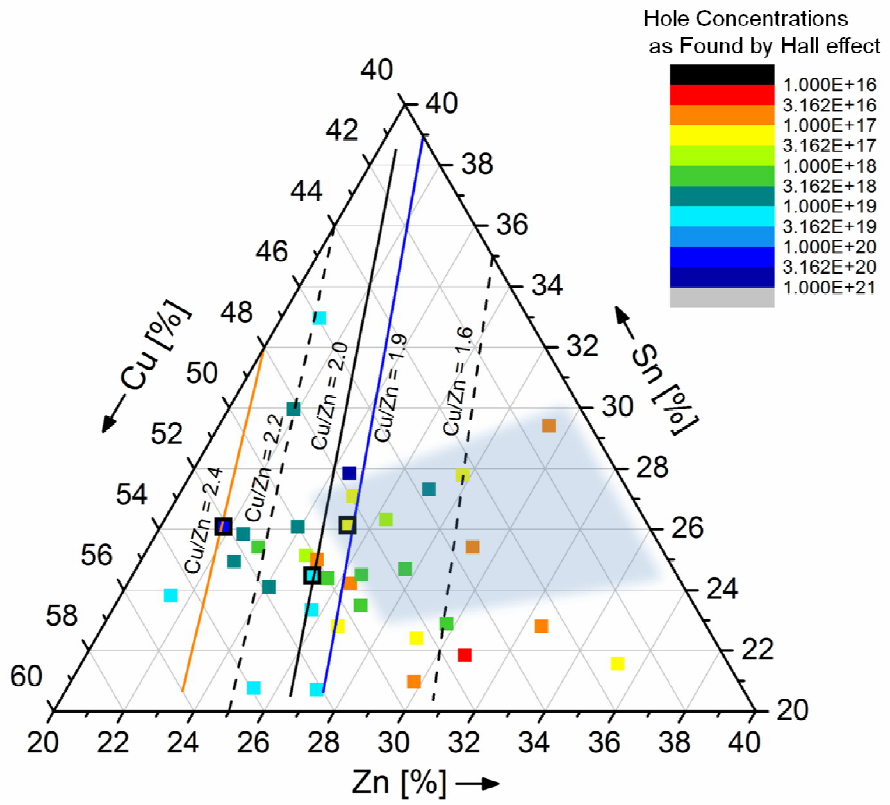

Figure 5.1 Hole concentrations, compiled from literature, as a function of CZTS cation composition.6-20 Lines of constant Cu-to-Zn ratio (Cu/Zn) are drawn and labeled. The Cu/Zn ratios used in this study were 2.4, 2.0 and 1.9. The shaded area corresponds to the composition region that yields the highest performing solar cells. The squares surrounded with thick black lines are the small-grained CZTS films studied in this work *(vide infra)*.

To understand and isolate the individual effects of Cu-to-Zn ratio, grain size, and Na incorporation on the carrier concentrations, carrier mobilities and electronic transport mechanisms in polycrystalline CZTS films, we synthesized and studied in detail a set of nine different films on impurity-free crystalline quartz substrates. All films were synthesized using *ex situ* sulfidation of co-sputtered Cu-Zn-Sn metal alloy films where the Cu-Zn ratio in the film can be controlled by adjusting the relative sputtering rates of the Cu-Zn, and Cu-Sn targets. The Cu-to-Sn ratio was kept constant at ≈ 2 for all of films and all films were sulfidized at 600 ^{o}C. Three sets of precursor films were deposited.

Each set was comprised of three films with the same Cu-to-Zn ratio: the Cu-to-Zn ratio of the films in the three sets were Cu/Zn=2.4 (Cu rich), Cu/Zn=2.0 (stoichiometric), and Cu/Zn=1.9 (Cu poor). One film from each set was sulfidized in 35 Torr of S vapor (1 mg S in the sulfidation tube): sulfidation at this pressure results in disordered small-grained films. This gave three films with nearly the same average grain size but with different Cu-to-Zn ratio. To investigate how grain size affects the properties of the films, a second film from each set with different Cu-to-Zn ratio was sulfidized at a higher sulfur vapor pressure. Specifically, films were sulfidized either at 540 Torr by including 15 mg of S in the sulfidation tube (for Cu-rich film) or 3600 Torr by including 100 mg of S (for stoichiometric and Cu-poor films). The higher S pressure during sulfidation results in much larger CZTS grain sizes.[31] Finally, a third film from each set was sulfidized under the same conditions as the first set, but prior to sulfidation the ampoule walls were coated with 0.3 µmol of NaOH, a method designed to incorporate Na into the film through the vapor phase.[21] This approach produced the matrix of nine films shown in Figure 5.2. The films in rows 1, 2 and 3 have Cu-to-Zn ratios of 1.9, 2.0 and 2.4, respectively. The films in column 1 all have small grain sizes and no Na while the films in column 2 all have much larger grains than those in column 1 but also no Na. The films in column 3 have similar grain sizes to the films in column 2 but these films also contain Na.

The electronic properties of all of the films in figure 5.2 were studied using temperature dependent resistivity and Hall effect measurements. All films were found to be *p*-type but the hole concentrations exhibited a strong dependence on the Cu-to-Zn ratio with Cu-rich films having extremely high hole densities, on the order of 10^{20} cm^{-3}. In contrast, Cu-poor films exhibited the lowest hole concentrations, as low as 2.7×10^{15} cm^{-3}. We found that in stoichiometric and Cu-poor films, increasing the grain size increased the hole mobility and decreased the hole concentration. While increasing mobility with larger grain size is expected and easy to understand in terms of reduced grain boundary scattering, the reasons for the decrease in carrier concentration are not as obivious. In this defect-doped material the decrease in hole concentration must be understood in terms of decreasing defect concentrations. If the defects that result in doping are at the grain

boundaries, larger grains and reduction in the grain boundaries may lead to reduction in the hole concentration. Alternatively, the micron-scale increase in order may be concomitant with and translate into increased small-scale local order such that defect states that lead to doping are also removed. In contrast, when the grain sizes in Cu-rich films were increased there was no reduction in the hole concentrations. We found that the addition of Na increased the carrier concentrations in the stoichiometric and Cu-poor samples by as much as four orders of magnitude. This increase in carrier concentration was accompanied by a decrease in mobility, consistent with impurity scattering. The carrier concentrations in Cu-rich films were again unaffected by incorporation of Na into the films.

All films showed insulating behavior with electronic transport dominated by variable range hopping at low temperatures but crossing over to band transport at high temperatures in all but the most resistive films. All Cu-rich films had carrier concentrations that exceeded the critical carrier density for the metal-insulator transition, yet still behaved as insulators. This suppressed transition is indicative of high degrees of compensation and fluctuating band edges, which is most apparent in Cu-rich films. This makes Cu-rich films unsuitable for solar cells.

Finally, we briefly address how the presence of CuS can lead to very high carrier concentrations and electronic transport behavior similar to that in Cu-rich films, even when Cu/Zn < 1.9 and the CuS does not form a percolated network within the film. This shows that CuS can not only act as shunting path in CZTS solar cells, but it can also dramatically change the electronic properties of the layer. We hypothesize that the presence of the metallic CuS may introduce small, isolated, metallic regions in the CZTS film, and the resultant band structure may be quite similar to the one we propose for the phase pure Cu rich films.

5.2 Experimental

CZTS films were synthesized *via ex situ* sulfidation of 430 nm thick Cu-Zn-Sn alloy films. The metallic precursor films were co-sputtered from Cu/Zn (35 at% Cu) and Cu/Sn

(60 at% Cu) targets at 15 mTorr using Ar as the working gas with a chamber base pressure of 2×10^{-7} Torr. The precursor films were deposited on impurity-free crystalline quartz. The stoichiometry of the CZTS film was controlled by altering the composition of the precursor film. This was accomplished by varying the power supplied to the Cu/Zn and Cu/Sn targets and thus changing the sputtering rates. Following deposition, the Cu-Zn-Sn precursor films were sealed in an evacuated quartz ampoule (base pressure of 10^{-6} Torr) with 1 mg to 100 mg of solid S depending on the desired sulfur vapor pressure. A 1, 15 and 100 mg S charge corresponded to S pressures of 36, 540 and 3600 Torr, respectively. Films with smallest grains were synthesized with 1 mg of S, while the Na free films with large grains were synthesized using 15 or 100 mg of S. To compensate for tin deficiencies in the precursor films where Cu/Zn = 2.0 and 1.9, ~ 1 mg of elemental Sn was included in the sulfidation ampoule. This generated SnS vapor during sulfidation, which incorporates into the film until the Cu-to-Sn ratio reaches ~ 2.0. The ampoules, containing the film and S, were placed in a box furnace and heated at a rate of 6.5 ^{o}C/min to 600 ^{o}C. All precursor films were sulfidized isothermally at 600 ^{o}C for 8 hours before cooling the ampoule back to room temperature naturally. Upon sulfidation, 430 nm thin Cu-Zn-Sn precursor films were transformed into ~2.2 µm thick CZTS films. Sodium was introduced into the films intentionally by coating the quartz tubes with a known volume and concentration of aqueous solution of NaOH. The NaOH solution was diluted from a purchased stock solution such that the final solution was of known molarity. Typically ~ 1 mL of solution was added to the quartz tube, and the tube was then allowed to dry vertically in a convection oven heated to 100 ^{o}C. Once the tube was dried, the precursor film and 1mg of S were loaded and the sulfidation was conducted as usual.

The films were removed by breaking the ampoules and were characterized using a battery of methods including X-ray diffraction (XRD), confocal Raman scattering microscopy, scanning electron microscopy (SEM), and energy dispersive X-ray spectroscopy (EDS). Specifically, XRD patterns of the Cu rich sulfidized films were collected using a Bruker D8 Discover system equipped with a Cu *Kα* X-ray source, 0.5 mm beam collimator, and a Vantec-500 2D area detector. The XRD patterns for the

stoichiometric and Cu poor films were collected on the same Bruker D8 Discover system, but with a Co *Kα* X-ray source. The patterns for these films were converted to account for the wavelength differences between the two X-ray sources and to be able to compare them directly with each other. Raman spectra were collected at room temperature using a WiTec alpha300R confocal Raman microscope equipped with a UHTS300 spectrometer and a DV401 CCD detector, and the films were illuminated with an Omnichrome Ar ion laser (514.5 nm, ~300 nm beam spot size). Raman scattering was collected in a backscattering geometry and dispersed with an 1800 lines/mm grating, resulting in a spectral resolution of 0.02 cm^{-1}. The morphology and spatially averaged elemental composition of the sulfidized films were examined using a JEOL 6500 SEM equipped with a Thermo-Noran Vantage EDS detector. The electron energy was set at 15 keV both for imaging and EDS measurements. At this energy the EDS probe depth is estimated to be near 2 µm, ensuring that the entire depth of the sulfidized films was examined. The average grain size of the CZTS films was determined from SEM images by averaging the number of grains along randomly chosen lines. At least 100 grains were sampled for each film.

5.3 Results & Discussion

The elemental compositions and grain sizes of the films in the matrix shown in Figure 5.2 are listed in Table 5.1. Figure 5.2 shows the SEM images of these films, and the differences in their grain sizes. Each of these films was also characterized using X-ray diffraction (Figure 5.3) and Raman spectroscopy (Figure 5.4) to examine their phase purity.

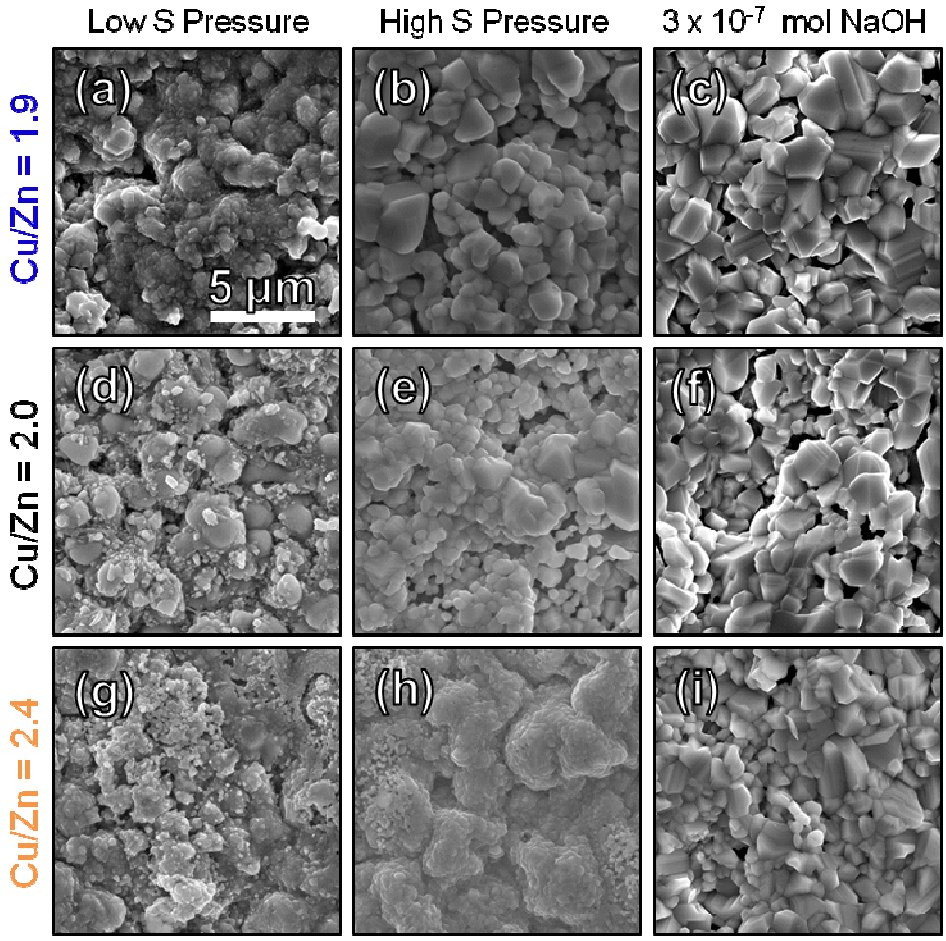

Figure 5.2 SEM images of films used in this study. Each row corresponds to a different copper-to-zinc ratio (Cu/Zn): Films in row 1 (a-c) are Cu poor with Cu/Zn=1.9, films in row 2 are nominally stoichiometric with Cu/Zn=2, and films in row 3 are Cu rich with Cu/Zn=2.4. Column 1 (a, d & g) shows films with small grains synthesized using low S vapor pressure (36 Torr) and without intentional Na addition. Column 2 (b, e & h) shows films with large grains synthesized using high S vapor pressures (540 or 3600 Torr) also without intentional Na addition. Column 3 (c, f & i) shows films synthesized under same conditions as column 1 but with $3x10^{-7}$ mol NaOH added to the sulfidation tube as described in the text. Column 3 has similar grain sizes to the films in column 2 but films in column 3 has Na incorporated in them.

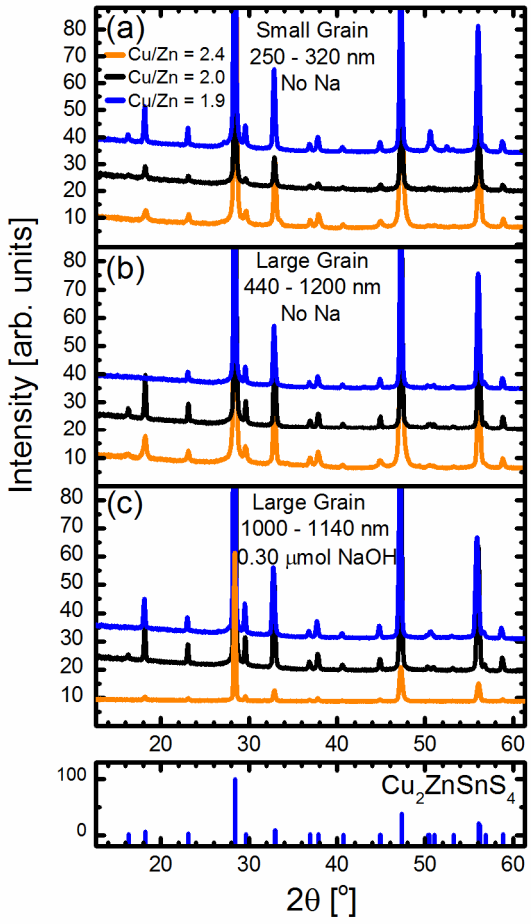

Figure 5.3 XRD from (a) CZTS films with small (250 - 320 nm) and (b) large (440 - 1200 nm) grains. (c) XRD from films synthesized with 0.3 μm of NaOH in the sulfidation ampoule. The XRD in panels (a), (b) and (c) correspond to the films in columns 1, 2 and 3 of Figure 5.2, respectively. The bottom panel displays the expected CZTS powder diffraction pattern for comparison.

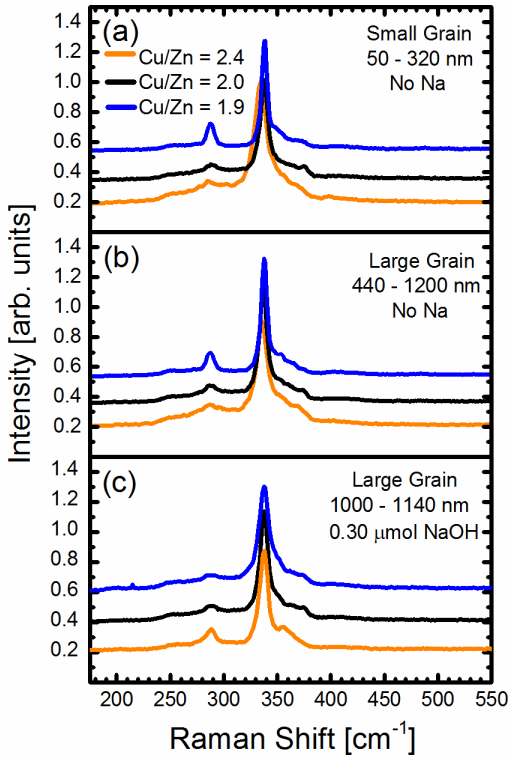

Figure 5.4 Raman spectra from (a) CZTS films with small (250 - 320 nm) and (b) large grains (440 - 1200 nm). (c) Raman spectra from films synthesized with 0.3 μm of NaOH in the sulfidation ampoule. The Raman spectra in panels (a), (b) and (c) correspond to the films in columns 1, 2 and 3 of Figure 5.2, respectively. All peaks are consistent with CZTS.

Table 5.1 Elemental compositions and average grain sizes of the films shown in the experimental matrix of Figure 5.2.

	Film	Cu	Zn	Sn	S	Cu/Zn	Grain Size (μm)
Small Grained	Cu rich	27.13	11.35	13.57	47.95	2.4	0.32 ± 0.05
	stoichiometric	26.36	13.15	12.80	47.69	2.0	0.25 ± 0.5
	Cu poor	24.84	12.96	13.37	48.83	1.9	0.31 ± 0.03
Large Grained	Cu rich	26.27	11.58	13.49	48.67	2.3	1.2 ± 0.2
	Stoichiometric	26.39	13.23	12.78	47.59	2.0	0.88 ± 0.2
	Cu poor	25.12	13.27	13.01	48.60	1.9	0.44 ± 0.06
0.3 μm NaOH Addition	Cu rich	28.06	11.20	14.38	46.36	2.5	1.14 ± 0.1
	Stoichiometric	25.15	12.62	13.37	48.86	2.0	1.13 ± 0.2
	Cu poor	23.75	12.66	13.84	49.75	1.9	1.0 ± 0.2

5.3.1 Carrier Concentrations and Mobilities as a Function of Stoichiometry, Grain size, and Na addition

Stoichiometry

Figure 5.5 shows the resistivities, carrier concentrations and mobilities at 270 K for all the films shown Figure 5.2. Focusing on the resistivities of small-grained, impurity-free films, we see striking and significant differences among the three films with different Cu-to-Zn ratios. The Cu-rich film has the lowest resistivity (~0.2 Ω cm), while the stoichiometric and Cu-poor samples have resistivities three and four orders of magnitude larger, respectively, than the Cu-rich film. To isolate and examine the effects of Cu-to-Zn ratio on carrier concentrations and mobilities, we compare the Hall-effect measurements on small-grain, impurity-free films CZTS films (i.e., column 1 in Fig. 5.2). The differences in resistivities is in large part due to the differences in carrier concentrations with the hole concentration varying widely over several orders of magnitude. The hole concentration in the Cu-rich film is 1.1×10^{20} cm^{-3}, while the stoichiometric and Cu-poor samples have significantly lower hole concentrations, 2.0×10^{19} and 1.5×10^{17} cm^{-3}, respectively. Impressively, decreasing the Cu-to-Zn ratio from 2.4 to 1.9, which manifests itself as just a few percent change in the relative atomic composition, leads to a three order of magnitude decrease in the hole concentration. These values are graphed in Figure 5.1 (squares with black outline) and compared with other values reported in the literature values. Such comparison shows that these values are consistent with the range in hole concentrations measured and reported by others. As mentioned in the introduction, this trend in carrier concentration with Cu-to-Zn ratio is predicted by first principles calculations. The hypothesis that is consistent with all measurements and calculations to date is that the concentration of the ionized acceptor Cu_{Zn}^{-} decreases quickly with a decreasing Cu-to-Zn ratio and that this defect is responsible for the very high hole concentrations in the Cu-rich films.[5]

The critical carrier concentration, n_c, at which we would expect the film to undergo a insulator-metal transition can be calculated from $a^*_B n_c^{1/3} \approx 0.25$, where a^*_B is the effective Bohr radius. Using the dielectric constant and effective mass reported in the literature,[32] we find that $a^*_B = 7.4$ Å, and $n_c = 3.9 \times 10^{19}$ cm^{-3}. The hole concentration in the Cu-rich film exceeds this value by one order of magnitude, so one would expect this film to exhibit metallic conductivity. However, as we will discuss below, this transition is suppressed, and all films, even when the carrier concentration exceeds n_c, exhibit insulating behavior.

There are significant differences in Hall mobilities as well. The Cu-rich film exhibited the highest Hall mobility at 0.25 cm^2 V^{-1} s^{-1}, while the Hall mobilities in the stoichiometric and Cu-poor films were 0.0033 and 0.071 cm^2 V^{-1} s^{-1}, respectively. The low mobilities of the stoichiometric and Cu-poor films are below values that are physically meaningful when measured by Hall effect (~ 0.1cm^2 V^{-1} s^{-1}). While we observe a real and unambiguous Hall effect (see Figure 5.6), these low mobilities are indicative of a suppressed Hall effect, consistent with hopping transport (*vide infra*).[31] A suppressed Hall effect would lead to an underestimated mobility and an overestimated carrier concentration. To elucidate the electronic transport mechanisms in these films we conducted a detailed analysis of the temperature dependent resistivity data *(vide infra).*

All the films exhibit what appears to be a very low mobility for solar cells. However, the measurement geometry used in this study gives the hole mobility in the plane of the film where the hole transport requires the crossing of many grain boundaries. In a solar cell, the relevant electronic transport is vertical through the film. This would require the crossing of much fewer grain boundaries. We attribute the low mobilities to both the disordered nature of these films and the relatively small grain sizes ranging from 250 to 320 nm (Figure 5.2).

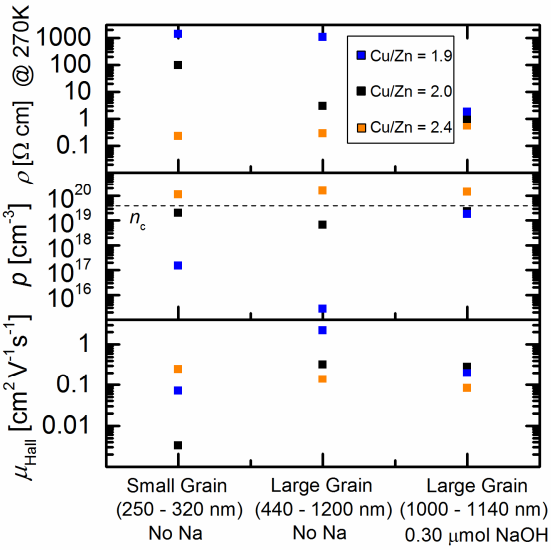

Figure 5.5 Resistivity, ρ, hole concentration, p, and hole mobility, μ_{Hall} of CZTS films in Figure 5.2 as determined from the Hall effect measurements at 270 K. The dashed line labeled n_c in the hole concentration panel corresponds to the estimated critical carrier concentration necessary for metal-insulator transition.

Grain Size

To examine the effects of grain size on the electronic properties of the CZTS films, precursor films with identical Cu-to-Zn ratio were sulfidized at low and high sulfur vapor pressures. This produced films with same Cu-to-Zn ratio but with different grain sizes. Increasing the S vapor pressure in the sulfidation ampoule increases the grain size in the CZTS films. Specifically, all small-grain films were synthesized at 36 Torr (1 mg S charged into the ampoule) while large-grain, impurity free films were synthesized at 540 Torr (15 mg S charged into the ampoule for Cu-rich film) and at 3600 Torr (100 mg of S charged into the ampoule for the stoichiometric and Cu poor films). The average grain sizes of the resulting films are summarized in Table 5.1. The small-grain films synthesized at low S pressure correspond to the films in column 1 of the matrix in Figure 5.1 while the large-grain films synthesized at high S vapor pressure are those shown in column 2. The grain sizes of the films synthesized at high S pressure are typical of the films used in solar cells. Importantly, these films were grown on a impurity-free quartz

substrate and did not have Na incorporated in them. Often, the grain sizes in CZTS films are increased by growing the film on SLG. Na from SLG has been shown to increase the grain sizes but it can also have additional effects such as doping the film or passivating the electronic defects. Increasing the grain size using the S pressure and without Na addition isolates the effect of grain size on the electronic properties without complications from the other effects of Na.

Figure 5.5 compares the resistivities, hole concentrations and mobilities of films with small and large grains and with different Cu-to-Zn ratio (*i.e.,* compare left and middle columns). Focusing on the resistivity values we see that both the Cu-poor and stoichiometric films with large grains have lower resistivities compared to their small-grained counterparts. In contrast, the resistivity of the Cu-rich film remains essentially unchanged and appears not to be strongly affected by the grain size. Consistent with its unchanged resistivity in the Cu-rich film, the Hall effect measurements (Figure 5.5) show that, there is essentially no change in the hole concentration or the mobility. The hole concentration and mobility in the Cu-rich large-grain film are 1.6×10^{20}cm^{-3} and 0.14 cm^2 V^{-1} s^{-1}, respectively, compared to 1.1×10^{20}cm^{-3} and 0.25 cm^2 V^{-1} s^{-1} for the Cu-rich small-grained film. Both of these hole concentrations are larger than the critical carrier concentration for metal-insulator transition. In contrast, the hole concentrations in the stoichiometric and Cu-poor films decrease with increasing grain size. The hole concentration in the stoichiometric and Cu-poor films with large grains are 6.5×10^{18} cm^{-3} and 2.7×10^{15} cm^{-3}, respectively. These hole concentrations are significantly lower than the corresponding values in the small-grain films, 2.0×10^{19} cm^{-3} and 1.5×10^{17} cm^{-3}, for the stoichiometric and Cu-poor films, respectively. The stoichiometric and Cu-poor films with larger grains also have higher Hall mobilities at 0.32 cm^2 V^{-1} s^{-1} and 2.21 cm^2 V^{-1} s^{-1}, respectively. These values are significantly larger than those measured in the corresponding small-grained films. The mobility of the large grained Cu-poor film in particular is now in the range that maybe suitable for solar cells.

The increase in the carrier mobility in the stoichiometric and Cu-poor films is expected because there is a significant increase in crystallinity and grain size. The

decrease in carrier concentration, however, is more surprising. We do not attribute this to a change in S concentrations in the films with the increasing S pressure. First, within the accuracy of the EDS, the S concentrations are the same for films grown under high and low sulfur pressures. Second, if there was a change in S concentration, the most likely consequence would be a decrease in the concentration of S vacancies with increasing S pressure. Sulfur vacancies are expected to be *n*-type dopants, so that if their concentration were decreased, we would expect an increase in the hole concentration with increasing S pressure.[5] This is opposite of the observed trend and does not explain the decrease in the hole concentration. The decrease in the hole concentration could be due to a decrease in disorder, which is certainly evident at the micron-level, such that the concentrations of defects or defect complexes that dope the film *p*-type are significantly lowered. It is also possible that the decreased hole concentration is tied to the decrease in grain boundary area. If the grain boundaries are defect rich and these defects dope the film *p*-type, the decrease in grain boundary area would be accompanied with a decrease in the concentrations of these defects and holes.

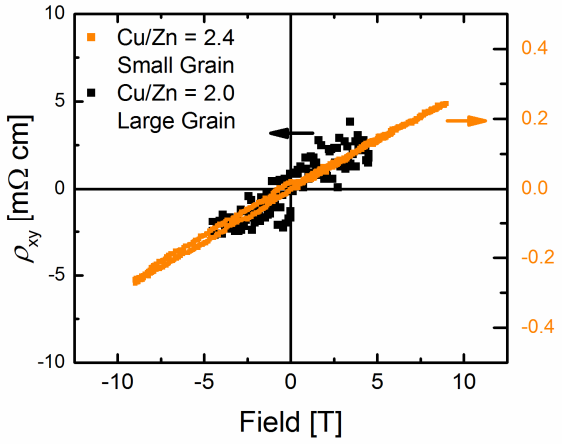

Figure 5.6 Hall-effect data collected from the small-grained Cu-rich film (orange with $p = 1.1\times10^{20}$ cm^{-3}) and from the large grained stoichiometric film (black with $p = 6.5\times10^{18}$ cm^{-3}).

Na Incorporation

The CZTS films for highest performing solar cells are synthesized on a Mo-coated SLG substrate, and it has been demonstrated that Na diffusion from the SLG substrate leads to better solar cell performance.[22,27] The presence of Na in the CZTS films may affect the structural and electronic properties of the film in several ways; it clearly boosts grain size,[21] it may passivate the grain boundaries in the film[28] or act as a dopant, increasing the carrier concentrations.[27,33] To investigate the effects of Na on the electronic properties, we introduced Na into the CZTS films through the vapor phase by coating the sulfidation ampoule with NaOH.[21] We examined only one Na concentration, 0.3 μmol NaOH loading, as this concentration gave us comparable grain sizes to those films that were sulfidized with 100 mg of S.

Na incorporation into the Cu-poor and stoichiometric CZTS films dramatically decreased their resistivities. This decrease is obvious when comparing the resistivities of the large-grain impurity-free films (the middle column in Figure 5.5) with those of large-grain films with Na (the right column in Figure 5.5). In fact, both the Cu-poor and stoichiometric films have resistivities that are comparable to the Cu-rich films. In contrast, the resistivity of the Cu-rich film did not change significantly with introduction of Na. The Hall effect measurements of the hole concentration and mobility show that changes in both contribute to the changes in the resistivities of the stoichiometric and Cu-poor films. Specifically, the hole concentration in the Cu-poor film increased dramatically from 2.7×10^{15} to 1.8×10^{19} cm^{-3} with Na incorporation, while the mobility decreased by an order of magnitude from 2.21 to 0.19 $cm^2\ V^{-1}\ s^{-1}$. Similarly, the hole concentration in the stoichiometric film increased from 6.5×10^{18} to 2.3×10^{19} cm^{-3} while the mobility only changed slightly from 0.32 without Na compared to 0.28 $cm^2\ V^{-1}\ s^{-1}$ with Na. The hole concentration in the Cu-rich film with Na was nearly the same as that in the Cu-rich film without Na 1.4×10^{20} cm^{-3} versus 1.6×10^{20} cm^{-3}, respectively. The hole mobility in the film with Na was approximately a factor of two lower, at 0.083 $cm^2\ V^{-1}\ s^{-1}$. The Cu-rich film again had a carrier concentration that exceeded the critical carrier concentration.

These measurements show that incorporation of Na into the CZTS film affects the hole concentrations. In summary, Na incorporation increased the hole concentration by four orders of magnitude in the Cu-poor film and approximately a factor of two in the stoichiometric films. The hole concentrations in the Cu-rich film, however, remained the same, most likely because the Cu-rich films already had very high carrier concentrations. This increase in hole concentrations with Na incorporation is consistent with Li *et al.* and Nagaoka *et al.* who also demonstrated that the addition of Na to CZTS results in a higher hole concentrations. [27,29] While the mechanism is not entirely understood, Nagaoka *et al.* proposed that Na inhibits the formation of the donor defect Zn_{Cu} through the creation of Na_{Cu}, thereby decreasing levels of compensation and increasing the effective hole concentration.[29] In the case of CZTSe solar cell devices, though, the introduction of excess Na in the form of NaF was accompanied by the formation of a deep acceptor level at 0.428 eV above the valence band.[27] It is also possible that Na incorporation into the film may aid the formation of the ionized acceptor states Cu_{Zn}^{-} and/or V_{Cu}^{-}. These mechanisms are even more intriguing considering the link between Zn diffusion, Na introduction, and grain growth observed by Gerhshon *et al.* where it was proposed that Na may complex with Zn and S to promote Zn incorporation.[28] We also cannot rule out the formation of Na containing phases on grain boundary surfaces that may introduce new defect levels, in effect 'doping' the CZTS layer. Clearly, more research must be conducted to improve our understanding of the role of Na in increasing the hole concentrations in the CZTS films.

Surprisingly, the Cu-poor and stoichiometric films also exhibited a large decrease in mobility when Na was incorporated into these films. This decrease appears to be inconsistent with the observations by Gershon *et al.* and Nagaoka *et al.* who showed that the carrier mobility increased with Na incorporation.[28,29] However, the mobility increase observed in these studies was likely due to the increase in the grain sizes and reduction of the grain boundary scattering. The decrease we witness in this study is most likely due to ionized impurity scattering. Indeed, a plot of all the Hall mobilities as a function of the hole concentrations (Figure 5.7) including those with Na shows that all physically

meaningful mobilities fall on the same line. Only the extremely low mobilities where the Hall effect is suppressed deviate from this line (shown in the shaded area in figure 5.7).

These results provide strategies for rational control of the resistivity, carrier mobility and hole concentrations in CZTS films. To achieve films with reasonably low hole concentrations for solar cells, films must be stoichiometric or Cu-poor. High mobilities require large grain sizes which may be achieved either through high S pressure during synthesis or post synthesis annealing or through the introduction of Na (or K). Achieving a resistivity that is suitable for solar cells requires a careful balance in mobility and carrier concentrations because the mobility degrades with increasing carrier concentrations and increasing ionized donor scattering. One could control the amount of Na added into the film or the Cu-to-Zn ratio to tune the carrier concentrations and resistivity. While control over carrier concentrations and mobilities are undoubtedly important, we must also look at how stoichiometry, grain size and Na introduction affect the transport mechanisms within the CZTS films.

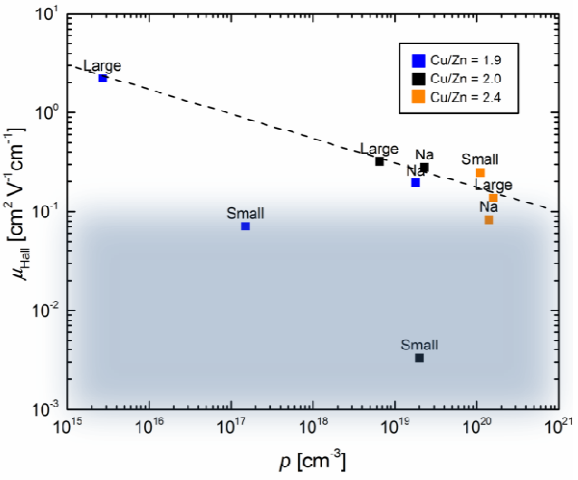

Figure 5.7 The Hall mobility of all the CZTS films plotted as a function of the hole concentration. The color denotes the stoichiometry of the film while the label on each point informs whether the film had small grains, large grains, or whether it contained Na. The dashed line is drawn to guide the eye. The shaded region indicates mobilities that are not physically meaningful with Hall effect measurements.

5.3.2 Temperature Dependent Resistivity Measurements and Transport Mechanisms

Figure 5.8 shows the temperature dependence of the resistivities of all CZTS films in this study (*i.e.*, all the films in the matrix shown in Figure 5.2). These measurements are commensurate with the Hall effect data at 270 K; Cu-poor films are the most resistive in all cases while Cu-rich films are the least resistive. Incorporation of Na into the films decreases the film resistivities and brings all the resistivity vs. temperature curves close to each other. All films, even when the carrier concentrations exceeded the predicted critical concentration, display insulating behavior. *i.e.*, exponentially rising resistivity with decreasing temperature. The temperature dependence of the resistivity follows $\rho=\rho_o \exp (T_o/T)^m$ where the value of the exponent *m*, depends on the carrier transport mechanism. The value of *m* can be found in an unbiased manner from the slope of ln(*w*) vs ln (*T*) where $w = -d(\ln\rho)/d(\ln T)$; this method is also known as the derivative plot method. These ln(*w*) vs. ln (*T*) plots for the data in Figure 5.8 are shown for all films in Figure 5.9. Figure 5.9 also shows lines with slopes *m*= -1/2, *m*= -1/4 and *m*= -1, for the lowest, middle and highest temperature ranges for comparison. The *m* values determined by fitting the data in these three temperature ranges are listed in Table 5.2. All of the ln(*w)* values are positive but are offset in the vertical direction for clarity in Figure 5.9; this does not change the value of the slope *(i.e. m)*.

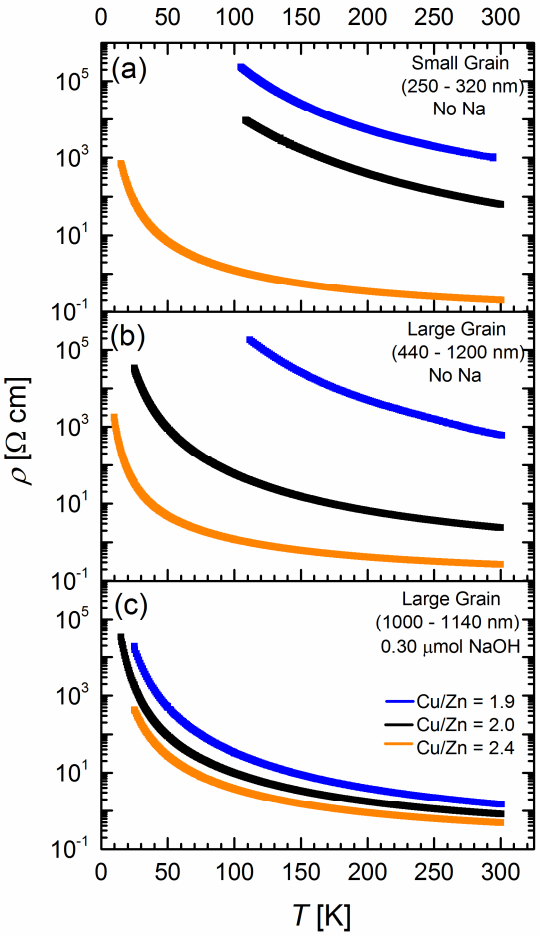

Figure 5.8 The temperature dependence of the resistivities of (a) CZTS films with small (250 - 320 nm) and (b) large grains (440 - 1200 nm). (c) Temperature dependence of the resistivities of films synthesized with 0.3 μmoles of NaOH in the sulfidation ampoule. The resistivity data in panels (a), (b) and (c) correspond to the films in columns 1, 2 and 3 of Figure 5.2, respectively

We discuss the films with small grains first (column 1 in Figure 5.2). These films were the most resistive films in this study. The stoichiometric film could be fit with $m \sim -0.25$ over the entire temperature range. This implies that the electronic transport mechanism is 3D Mott variable range hopping (M-VRH), which follows the form $\rho=\rho_{Mott}$ exp $(T_{Mott}/T)^{1/4}$, with $T_{Mott}= 18/k_B L_c^3 N(E_F)$, where L_c is the localization length and $N(E_F)$ is the density of states near the Fermi level (E_F).[34] This observation is consistent with the

three dimensional nature of our films. This hopping transport is likely responsible for the suppressed Hall effect. It is well-known that hopping transport suppresses the Hall effect, which in this case may lead to Hall mobilities that are low and physically not meaningful.

The Cu-poor film, over the entire temperature range measured, and the Cu-rich film, over the low temperature range of the Cu rich sample, exhibit temperature dependence with $m \sim -1/2$. This value may be interpreted as either Efros-Shklovskii variable range hopping (ES-VRH) or as hopping between small highly conductive regions in an insulating matrix. In ES-VRH, Coulomb interactions open up a soft gap in the density of states at E_F resulting in $\rho=\rho_{ES} \exp (T_{ES}/T)^{1/2}$. Here, $T_{ES} = 2.8e^2/\kappa k_B L_C$ where κ is the dielectric constant in the insulating limit.[35] A T dependence where $m = -1/2$ may is also observed when electronic transport occurs *via* thermally assisted tunneling between nanoscopic conductive regions embedded in a more insulating matrix. Magnetoresistance measurements are required to discern between these two mechanisms, which were not performed with this set of samples. We can, however, confirm whether ES-VRH is reasonable by further considering the value of T_{ES}, which will be discussed below. In the Cu-rich film, at high temperatures, m appears to approach -1. This is typically interpreted as either simple activated transport or thermionic emission over grain boundaries in polycrystalline films.

The maximum value for T_{ES} (T^{max}_{ES}) can be calculated by assuming that the minimum localization length is the effective Bohr radius a_B^*, which can be calculated using the published values of the dielectric constant (in the insulating limit) and the effective mass.[32] We find that $T^{max}_{ES} \approx 116{,}000$ K. The values for T_{ES}, as well as T_{Mott}, extracted from the temperature dependent resistivity data are shown in Figure 5.10 for all films. These values were extracted by plotting ln ρ versus $T^{-1/2}$ (or $T^{-1/4}$ for M-VRH), such that the slope corresponds to $T_{ES}^{1/2}$ (or $T_{Mott}^{1/4}$). The values of T_{ES} for both the Cu-rich and Cu-poor films, 1638 K and 19412 K, respectively, are significantly below the maximum value and ES-VRH is in fact a possible conduction mechanism. The value of T_{ES} for the Cu-poor film is notably larger than the Cu-rich film, which is expected given

the large difference in carrier concentrations; the values for L_C and κ diverge with increasing p. Without knowing the values of L_C and κ it is difficult to reach any other strong conclusions about the values of T_{ES}.

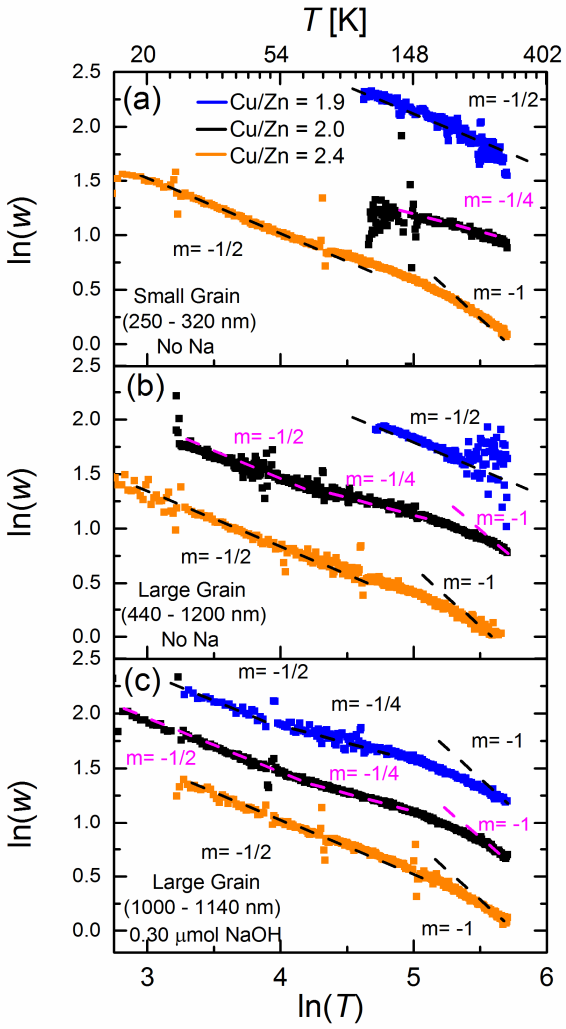

Figure 5.9 The temperature dependent resistivity data plotted as ln(w) vs. ln (T) where $w = -d(\ln\rho)/d(\ln T)$ for (a) CZTS films with small grains (250 - 320 nm) (b) for CZTS films with large grains (440 - 1200 nm) and (c) for large-grained CZTS films synthesized with 0.3 µmoles of NaOH in the sulfidation ampoule. The resistivity data in panels (a), (b) and (c) correspond to the films in columns 1, 2 and 3 of Figure 5.2, respectively. The dashed lines are not fitted, but lines with slopes of -1/2, -1/4, or -1 (labeled accordingly) to guide the eye. The fitted values for the slope, m, may be found in Table 5.2.

Next, we discuss the electronic transport in CZTS films with large grains (column 2 in Figure 5.2). The temperature dependence of the resistivity of Cu-poor and Cu-rich films are quite similar to their small grained counterparts. The exponent m is -1/2 for the Cu-poor film over the entire temperature range where measurements were possible. The exponent m is also -1/2 for the Cu-rich sample at low temperatures. The T_{ES} values for these films are all below the maximum possible value so that ES-VRH is feasible (Figure 5.10). At high temperatures, the m value for the Cu-rich film again appears to approach -1, the value expected for either activated transport or thermionic emission over grain boundaries. The large-grained stoichiometric film has a lower resistivity than the film with small grains such that a lower temperature range can now be examined in our set up. In the stoichiometric films with large grains, $m \sim -1/2$ at low temperatures, indicating ES-VRH is feasible. The extracted value of T_{ES} is certainly reasonable at 3735 K (Figure 5.10). At intermediate temperatures, $m \sim -1/4$, indicating a transition to M-VRH. The temperature at which this crossover occurs ($T_{Crossover}$) was estimated from the ln(w) vs. ln(T) plot to be ~54 K (Figures 5.9 and 5.10). The crossover temperature can also be predicted using the extracted values for T_{Mott} and T_{ES} such that $T_{Crossover} = 16T_{ES}^2/T_{Mott}$.[36] Using this method, a cross over temperature of 51 K is predicted (Figure 5.10), in very close agreement with the value estimated from the ln(w) vs. ln(T) plot. At higher temperatures, the m value for the stoichiometric film with large grains also approaches -1, and we believe this is due to activated transport. The predicted value for $T_{Crossover}$ assumes that only ES-VRH and M-VRH are present as electronic transport mechanisms. That the estimated and experimentally determined values of the crossover temperature agree well prompts us to conclude that thermionic emission is not occurring combined with VRH or activated transport.

Table 5.2 The force fit values for the slope *m* from **the derivative plot for each of the films. The lines were fit by a linear regression. The corresponding temperature range for each fit is in parenthesis below the value for *m*.**

		m @ low *T* (range)	*m* @ med. *T* (range)	*m* @ high *T* (range)
Small Grained	Cu rich	-0.45 (15 K - 145 K)		-0.74 (> 145 K)
	Stoichiometric		-0.26 (> 105 K)	
	Cu poor		-0.60 (> 75K)	
Large Grained	Cu rich	-0.48 (25 K - 135 K)		-0.68 (> 135 K)
	Stoichiometric	-0.44 (25 K - 50 K)	-0.29 (50 K - 180 K)	-0.59 (> 180 K)
	Cu poor		-0.57 (> 105 K)	
0.3 µm NaOH Addition	Cu rich	-0.46 (25 K - 165 K)		-0.75 (> 165 K)
	Stoichiometric	-0.48 (15 K - 60 K)	-0.33 (60 K - 120 K)	-0.57 (> 120 K)
	Cu poor	-0.45 (25 K - 50 K)	-0.31 (50 K - 140 K)	-0.62 (> 140 K)

Finally, we discuss the films with intentionally added Na. The resistivity curves are very close to each other (Figure 5.8), and the ln(*w*) vs. ln(*T*) plot reflects this. At low temperatures, all Na containing films show $m \sim -1/2$, with very similar T_{ES} values and all less than the maximum value for ES-VRH (Figure 5.10). Again, this means that we cannot rule out the possibility of ES-VRH or hopping between highly conductive, nanoscopic areas within the insulating CZTS matrix. At intermediate temperatures, the Cu-poor and stoichiometric films have an *m* value near -1/4, indicating a crossover to M-VRH. The empirically measured and predicted values of $T_{Crossover}$ are again in close agreement (Figure 5.10). At high temperatures ($T > 120$ K), in all films, *m* approaches -1. In Cu-poor and stoichiometric films, this is likely due to activated transport because the agreement between the predicted and the measured crossover temperatures, $T_{Crossover}$, allows us to eliminate the possibility of thermionic emission.

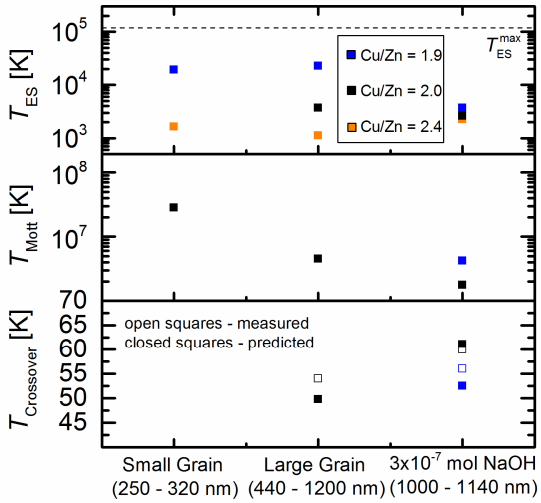

Figure 5.10 A summary of T_{ES}, T_{Mott}, and $T_{Crossover}$ extracted from the temperature dependent resistivity data in Figures 5.8 and 5.9.

We find that all of these films have remarkably similar transport mechanisms. At the lowest temperatures, when measurable, all films exhibit either ES-VRH or hopping between highly conductive regions in an insulating matrix. As temperature is increased to moderate temperature ranges, electronic transport crosses from ES-VRH to M-VRH in the stoichiometric films, and in the Na containing Cu-poor film. Finally, at high temperatures activated transport is approached.

We now address why the temperature dependence of the resistivities of Cu-rich films exhibit insulating behavior even though the carrier concentrations in these films exceeds the critical concentration for a metal-insulator transition. Suppression of the metal-insulator transition in a highly doped semiconductor is indicative of high levels of compensation and disorder within the gap. When coupled with local fluctuations in the band gap and band edges that are predicted to be prevalent in Cu rich films, a very disordered picture of the band structure, illustrated in Figure 5.11, emerges. The carrier concentration may be high enough to lower the Fermi level such that it crosses the fluctuating valence band leading to small isolated metallic regions. In this case, when the carrier concentration exceeds n_c, metallic regions do in fact form, however, due to band

fluctuations they are localized and isolated from one another: *i.e.*, they do not percolate to form continuous conductive regions. Isolated, conductive regions embedded in a more insulating matrix would result in semiconductor-like behavior and semiconductor-like dependence of the resistivity on temperature. The $m \sim -1/2$ behavior in the Cu-rich films may well be due to hopping between nanoscopic metallic regions over traditional ES-VRH. This type of band structure and inclusion of metallic regions would clearly be undesirable for solar cells because they may lead to increased electron-hole recombination rates.

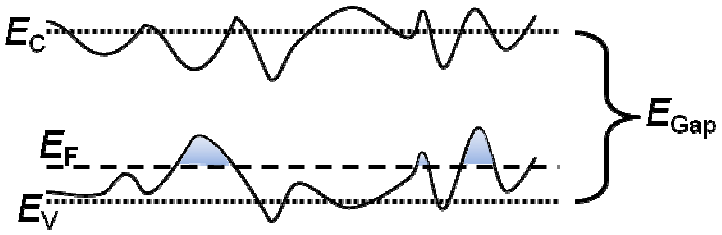

Figure 5.11 An illustration of the CZTS band structure with high degrees of compensation and local band gap fluctuations. The dotted lines mark the expected position of the valence and conduction bands, while the solid lines show the fluctuations. In high hole density conditions, the Fermi level (dashed line) may be low enough to cross the fluctuating valance band in some locations, forming local metallic regions (shaded).

5.3.3 The Influence of CuS Formation

One final issue that may also affect the electronic properties of CZTS films is the presence of $Cu_{2-x}S$. It has been reported that the presence of the metallic $Cu_{2-x}S$ or $Cu_{2-x}Se$ phases in $CuIn_xGa_{1-x}(Se,S)_2$ films results in a large increase in hole concentrations.[37] This has also been shown for CZTSe with $Cu_{2-x}Se$ precipitates present within the film.[38] Typically these phases are removed prior to solar cell fabrication by selectively etching them in KCN.[37–40] We examined the effects of the presence of $Cu_{2-x}S$ on the carrier concentration, mobility and resistivity on a film such that Cu/Zn ~ 1.8, similar to the Cu-poor film examined above. During the synthesis of this film, no elemental Sn was

included within the quartz ampoule, which resulted in a slight Sn deficiency such that Cu/Sn was ~ 2.2. This film was sulfidized with just 1 mg of S and had no impurity addition. As shown in Figure 5.12 (b), small CuS flakes are scattered over the surface of the film (circled in orange). This phase was confirmed to be CuS by EDS analysis, as well as Raman microscopy (Figure 5.12 (d)). However, the fraction of CuS is so small that it is below the detection limits of XRD, which is about ~ 1% (Figure 5.12 (c)). This demonstrates that CuS flakes do not make up a percolated network, but are interspersed at intervals much larger than their grain size over the surface of the film. No other secondary phases were detected.

Hall effect and temperature dependent resistivity measurements show that this film behaves significantly differently than the small-grained Cu-poor film discussed above. In fact, despite the low Cu/Zn ratio (~ 1.8) this film had electronic properties quite similar to the Cu-rich films. The room temperature resistivity was four orders of magnitude lower than the Cu-poor film discussed above (Figure 5.12 (a)). The hole concentration was 6.9×10^{20} cm^{-3}, a concentration even larger than the Cu rich films. The Hall mobility was 0.059 cm^2 V^{-1} s^{-1}, a value that is slightly below what is physically meaningful. A significantly reduced mobility is expected, however, due to the high hole concentration and increased impurity scattering.

Even though the carrier concentration was an order of magnitude larger than the calculated critical carrier concentration, this film still behaved like an insulator with the resistivity increasing exponentially with decreasing temperature. At low temperatures, *m* was ~ -1/2, much like the Cu-rich films. This would be consistent with either ES-VRH or hopping between nanoscopic conductive regions. T_{ES} is significantly below the theoretical maximum for ES-VRH, so we cannot rule out the possibility of ES-VRH occurring. However, considering the suppressed metal insulator transition evident in this film, we suspect that the band structure for this film is similar to that of the Cu-rich films described above and that hopping between metallic clusters is a likely possibility. At higher temperatures, *m* approaches -1, indicating a transition to either band transport or thermionic emission over grain boundaries.

It is unclear why the presence of CuS increases the hole concentration so dramatically. It is possible that this *p*-type metal injects holes into the CZTS, however the CuS is dispersed at length scales longer than the predicted accumulation region. Past results with CIGS suggest that $Cu_{2-x}S$ coats the surfaces of grains. Such a coating could fall below the detection limits of SEM or Raman spectroscopy, and we cannot rule out its presence within this film. This could ultimately create parallel conduction paths along the grain surfaces, which would be detrimental to solar cell performance as it could lead to shunting. Clearly, this phase should be avoided, either by including appropriate amounts of Sn to suppress $Cu_{2-x}S$ formation or by removing it with KCN after synthesis.

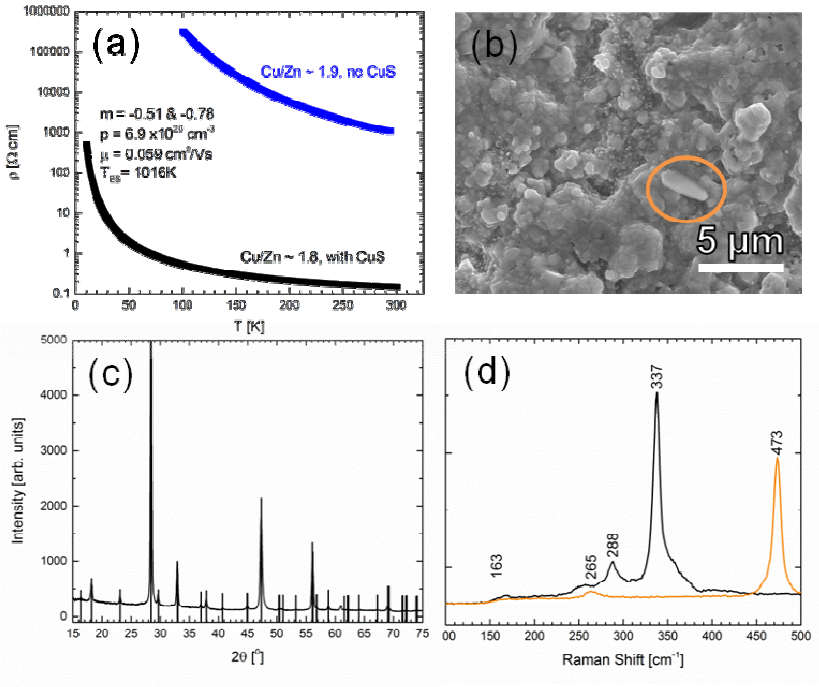

Figure 5.12 (a) Resistivity of a CZTS film containing CuS as a function of temperature. Resistivity of a Cu-poor film with no CuS precipitates is also shown for comparison. The inset parameters correspond to the CuS containing CZTS film. (b) SEM image of the film containing CuS, with a CuS flake circled in orange. (c) XRD from the CuS containing film. All peaks are assigned to CZTS and the expected powder diffraction pattern is shown as black vertical bars. (d) The Raman spectra from the CuS-containing CZTS film: panel (d) shows two spectra collected, using confocal microscopy, from isolated areas of CZTS (in black) and CuS (in orange).

5.4 Conclusions

We examined the carrier concentration, mobility, resistivity, and conduction mechanisms in CZTS films with different Cu-to-Zn ratios, grain size, and Na content. We found the Cu-to-Zn ratio to have a strong effect on the hole concentration in the films. Cu-rich films had hole concentrations in excess of the critical density for metal-insulator transition (~ 10^{20} cm^{-3}), while films that were Cu-poor had significantly lower hole concentrations (as low as ~10^{15} cm^{-3}), especially in the absence of Na addition. While we found the Hall mobility to be closely tied to the carrier density due to impurity scattering, higher mobility films are achieved in films with large grains, synthesized either with elevated S pressures or with the addition of Na. The addition of Na to the CZTS films was accompanied by a large increase in hole density in the Cu-poor and stoichiometric films, which indicates that care must be taken to control the amount of Na added to the film lest the carrier concentration increases and the mobility decreases too much.

Regardless of stoichiometry, grain size, or Na addition, all films exhibited variations of variable range hopping at lower temperatures, which transitioned to activated band transport at high temperatures, except for the most resistive films. Despite hole concentrations in excess of the critical concentration for metal-insulator transition, Cu rich films still exhibited insulator like behavior. We propose that this suppression of the metal-insulator transition is due to very high degrees of compensation, and due to the large fluctuations in the valence band edge. While localized metallic regions may in fact form they do not percolate to lead to metallic behavior.

Finally, we found, despite a film having a low Cu-to-Zn ratio, the presence of $Cu_{2-x}S$ is accompanied by significantly higher hole concentrations. These hole concentrations can be even higher than the Cu rich films described above, yet the film still exhibits temperature dependence of resistivity expected from semiconducting films. Care must be taken to mitigate the presence of $Cu_{2-x}S$, especially when making solar cells.

5.5 References

(1) Shin, B.; Gunawan, O.; Zhu, Y.; Bojarczuk, N. A.; Chey, S. J.; Supratik, G. *Prog. Photovoltaics Res. Appl.* **2013**, 72–76.

(2) Wang, W.; Winkler, M. T.; Gunawan, O.; Gokmen, T.; Todorov, T. K.; Zhu, Y.; Mitzi, D. B. *Adv. Energy Mater.* **2014**, *4*.

(3) Mitzi, D. B.; Gunawan, O.; Todorov, T. K.; Wang, K.; Guha, S. *Sol. Energy Mater. Sol. Cells* **2011**, *95*, 1421–1436.

(4) Katagiri, H.; Jimbo, K.; Tahara, M. *MRS Proc.* **2009**, *1165*.

(5) Chen, S.; Walsh, A.; Gong, X.-G.; Wei, S. *Adv. Mater.* **2013**, *25*, 1522–1539.

(6) Liu, F.; Li, Y.; Zhang, K.; Wang, B.; Yan, C.; Lai, Y.; Zhang, Z.; Li, J.; Liu, Y. *Sol. Energy Mater. Sol. Cells* **2010**, *94*, 2431–2434.

(7) Su, Z.; Yan, C.; Sun, K.; Han, Z.; Liu, F.; Liu, J.; Lai, Y.; Li, J.; Liu, Y. *Appl. Surf. Sci.* **2012**, *258*, 7678–7682.

(8) González, J. C.; Ribeiro, G. M.; Viana, E. R.; Fernandes, P. a; Salomé, P. M. P.; Gutiérrez, K.; Abelenda, a; Matinaga, F. M.; Leitão, J. P.; da Cunha, a F. *J. Phys. D. Appl. Phys.* **2013**, *46*, 155107.

(9) González, J. C. C.; Fernandes, P. a. A.; Ribeiro, G. M. M.; Abelenda, a.; Viana, E. R. R.; Salomé, P. M. P.; da Cunha, a. F. *Sol. Energy Mater. Sol. Cells* **2014**, *123*, 58–64.

(10) Nagaoka, A.; Miyake, H.; Taniyama, T.; Kakimoto, K.; Yoshino, K. *Appl. Phys. Lett.* **2013**, *103*, 112107.

(11) Seo, D.; Lim, S. *J. Mater. Sci. Mater. Electron.* **2013**, *24*, 3756–3763.

(12) Dhakal, T. P.; Peng, C.; Reid Tobias, R.; Dasharathy, R.; Westgate, C. R. *Sol. Energy* **2014**, *100*, 23–30.

(13) Tanaka, T.; Nagatomo, T.; Kawasaki, D.; Nishio, M.; Guo, Q.; Wakahara, A.; Yoshida, A.; Ogawa, H. *J. Phys. Chem. Solids* **2005**, *66*, 1978–1981.

(14) Shin, S. W.; Pawar, S. M.; Park, C. Y.; Yun, J. H.; Moon, J.-H.; Kim, J. H.; Lee, J. Y. *Sol. Energy Mater. Sol. Cells* **2011**, *95*, 3202–3206.

(15) Rajeshmon, V. G.; Kartha, C. S.; Vijayakumar, K. P.; Sanjeeviraja, C.; Abe, T.; Kashiwaba, Y. *Sol. Energy* **2011**, *85*, 249–255.

(16) Wu, X.; Liu, W.; Cheng, S.; Lai, Y.; Jia, H. *J. Semicond.* **2012**, *33*, 022002.

(17) Shi, C.; Shi, G.; Chen, Z.; Yang, P.; Yao, M. *Mater. Lett.* **2012**, *73*, 89–91.

(18) Amal, M. I.; Kim, K. H. *J. Mater. Sci. Mater. Electron.* **2012**, *24*, 559–566.

(19) Zhou, S.; Tan, R.; Jiang, X.; Shen, X.; Xu, W.; Song, W. *J. Mater. Sci. Mater. Electron.* **2013**, *24*, 4958–4963.

(20) Ruan, C.-H.; Huang, C.-C.; Lin, Y.-J.; He, G.-R.; Chang, H.-C.; Chen, Y.-H. *Thin Solid Films* **2014**, *550*, 525–529.

(21) Johnson, M.; Baryshev, S. V.; Thimsen, E.; Manno, M.; Zhang, X.; Veryovkin, I. V.; Leighton, C.; Aydil, E. S. *Energy Environ. Sci.* **2014**, *7*, 1931.

(22) Sutter-Fella, C. M.; Stukelberger, J. A.; Hagendorfer, H.; Mattina, F. La; Kranz, L.; Nishiwaki, S.; Uhl, A. R.; Romanyuk, Y. E.; Tiwari, A. N. *Chem. Mater.* **2014**, *26*, 1420–1425.

(23) HLAING Oo, W. M.; Johnson, J. L.; Bhatia, A.; Lund, E. A.; Nowell, M. M.; Scarpulla, M. A. *J. Electron. Mater.* **2011**, *40*, 2214–2221.

(24) Kronik, L.; Cahen, D.; Schock, H. *Adv. Mater.* **1998**, *10*, 31–36.

(25) Rockett, A. *Thin Solid Films* **2005**, *480-481*, 2–7.

(26) Wei, S.-H.; Zhang, S. B.; Zunger, A. *J. Appl. Phys.* **1999**, *85*, 7214.

(27) Li, J. V.; Kuciauskas, D.; Young, M. R.; Repins, I. L. *Appl. Phys. Lett.* **2013**, *102*, 163905.

(28) Gershon, T.; Shin, B.; Bojarczuk, N.; Hopstaken, M.; Mitzi, D. B.; Guha, S. *Adv. Energy Mater.* **2014**, 1400849.

(29) Nagaoka, A.; Miyake, H.; Taniyama, T.; Kakimoto, K.; Nose, Y.; Scarpulla, M. A.; Yoshino, K. *Appl. Phys. Lett.* **2014**, *104*, 152101.

(30) Contreras, M. A.; Egaas, B.; Dippo, P.; Webb, J.; Granata, J.; Ramanathan, K.; Asher, S.; Swartzlander, A.; Noufi, R. … *Rec.* … **1997**.

(31) Chernomordik, B. D.; Béland, A. E.; Deng, D. D.; Francis, L. F.; Aydil, E. S. *Chem. Mater.* **2014**, *26*, 3191–3201.

(32) Persson, C. *J. Appl. Phys.* **2010**, *107*, 053710.

(33) Prabhakar, T.; Jampana, N. *Sol. Energy Mater. Sol. Cells* **2011**, *95*, 1001–1004.

(34) Mott, N. *Metal-Insulator Transitions*; 2nd ed.; Taylor & Francis, 1990.

(35) Shklovskii, B. I.; Efros, A. L. Springer Verlag, 1984.

(36) Castner, T. G. In *Hopping Transport in Solids*; Pollack, M.; Shklovskii, B. I., Eds.; Elsevier: North-Holland, 1990.

(37) Ogawa, Y.; Jäger-Waldau, A.; Hua, T. H.; Hashimoto, Y.; Ito, K. *Appl. Surf. Sci.* **1996**, *92*, 232–236.

(38) Tanaka, T.; Sueishi, T.; Saito, K.; Guo, Q.; Nishio, M.; Yu, K. M.; Walukiewicz, W. *J. Appl. Phys.* **2012**, *111*, 053522.

(39) Mousel, M.; Schwarz, T.; Djemour, R.; Weiss, T. P.; Sendler, J.; Malaquias, J. C.; Redinger, A.; Cojocaru-Mirédin, O.; Choi, P.-P.; Siebentritt, S. *Adv. Energy Mater.* **2014**, *4*

(40) Walter, T.; Content, A.; Velthaus, K. O.; Schock, H.-W. *Sol. Energy Mater. Sol. Cells* **1992**, *26*, 357–368.

Compiled Bibliography

Chapter 1

1. *International Energy Outlook 2013*; 2013.

2. O'Rourke, S. No Title http://www.slideshare.net/gwsolar/pv-status-and-pathways-stephen-orourke .

3. Norris, D. J.; Aydil, E. S. *Science* **2012**, *338*, 625–626.

4. *Technology Roadmap: Solar Photovoltaic Energy*; IEA Technology Roadmaps; OECD Publishing, 2014.

5. Wadia, C.; Alivisatos, a P.; Kammen, D. M. *Environ. Sci. Technol.* **2009**, *43*, 2072–2077.

6. Wolden, C. A.; Kurtin, J.; Baxter, J. B.; Repins, I.; Shaheen, S. E.; Torvik, J. T.; Rockett, A. A.; Fthenakis, V. M.; Aydil, E. S. *J. Vac. Sci. Technol. A Vacuum, Surfaces, Film.* **2011**, *29*, 030801.

7. Zhao, J.; Wang, A.; Yun, F.; Zhang, D.; Roche, D. M.; Wenham, S. R.; Green, M. A. *Prog. Photovoltaics Res. Appl.* **1997**, *5*, 269–276.

8. No Title http://cleantechnica.com/2013/11/07/first-solar-reports-largest-quarterly-decline-cdte-module-cost-per-watt-since-2007/.

9. No Title http://investor.firstsolar.com/releasedetail.cfm?ReleaseID=864426.

10. Jackson, P.; Hariskos, D.; Wuerz, R.; Wischmann, W.; Powalla, M. *Phys. Status Solidi - Rapid Res. Lett.* **2014**, *8*, 219–222.

11. Wang, W.; Winkler, M. T.; Gunawan, O.; Gokmen, T.; Todorov, T. K.; Zhu, Y.; Mitzi, D. B. *Adv. Energy Mater.* **2014**, *4*.

12. Katagiri, H.; Jimbo, K.; Yamada, S.; Kamimura, T.; Maw, W. S.; Fukano, T.; Ito, T.; Motohiro, T. *Appl. Phys. Express* **2008**, *1*, 041201.

13. Guo, Q.; Ford, G. M.; Yang, W.-C.; Walker, B. C.; Stach, E. a; Hillhouse, H. W.; Agrawal, R. *J. Am. Chem. Soc.* **2010**, *132*, 17384–17386.

14. Guo, Q.; Hillhouse, H.; Agrawal, R. *J. Am. Chem. Soc.* **2009**, 11672–11673.

15. Khare, A.; Wills, A. W.; Ammerman, L. M.; Norris, D. J.; Aydil, E. S. *Chem. Commun.* **2011**, *47*, 11721–11723.

16. Todorov, T. K.; Reuter, K. B.; Mitzi, D. B. *Adv. Mater.* **2010**, *22*, E156–9.

17. Repins, I.; Beall, C.; Vora, N.; DeHart, C.; Kuciauskas, D.; Dippo, P.; To, B.; Mann, J.; Hsu, W.-C.; Goodrich, A.; Noufi, R. *Sol. Energy Mater. Sol. Cells* **2012**, *101*, 154–159.

18. Shin, B.; Gunawan, O.; Zhu, Y.; Bojarczuk, N. A.; Chey, S. J.; Supratik, G. *Prog. Photovoltaics Res. Appl.* **2013**, 72–76.

19. Ericson, T.; Kubart, T.; Scragg, J. J.; Platzer-Björkman, C. *Thin Solid Films* **2012**, *520*, 7093–7099.

20. Katagiri, H.; Ishigaki, N.; Ishida, T.; Saito, K. *Jpn. J. Appl. Phys.* **2001**, *40*, 500–504.

21. Cheng, A.-J.; Manno, M.; Khare, A.; Leighton, C.; Campbell, S. A.; Aydil, E. S. *J. Vac. Sci. Technol. A Vacuum, Surfaces, Film.* **2011**, *29*, 051203.

22. Katagiri, H.; Jimbo, K.; Maw, W. S.; Oishi, K.; Yamazaki, M.; Araki, H.; Takeuchi, A. *Thin Solid Films* **2009**, *517*, 2455–2460.

23. Fernandes, P. A.; Salomé, P. M. P.; da Cunha, A. F.; Schubert, B.-A. *Thin Solid Films* **2011**, *519*, 7382–7385.

24. Scragg, J.; Berg, D.; Dale, P. *J. Electroanal. Chem.* **2010**, *646*, 52–59.

25. Schurr, R.; Hölzing, A.; Jost, S.; Hock, R.; Voβ, T.; Schulze, J.; Kirbs, A.; Ennaoui, A.; Lux-Steiner, M.; Weber, A.; Kötschau, I.; Schock, H.-W. *Thin Solid Films* **2009**, *517*, 2465–2468.

26. Vaughan, D.; Craig, J. *Mineral chemistry of metal sulfides*; Cambridge University Press: London, UK, 1978.

27. Fairbrother, A.; Fontané, X.; Izquierdo-Roca, V.; Espíndola-Rodríguez, M.; López-Marino, S.; Placidi, M.; Calvo-Barrio, L.; Pérez-Rodríguez, A.; Saucedo, E. *Sol. Energy Mater. Sol. Cells* **2013**, *112*, 97–105.

28. Han, J.; Shin, S. W.; Gang, M. G.; Kim, J. H.; Lee, J. Y. *Nanotechnology* **2013**, *24*, 095706.

29. Weber, A.; Mainz, R.; Schock, H. W. *J. Appl. Phys.* **2010**, *107*, 013516.

30. Olekseyuk, I. D.; Dudchak, I. V.; Piskach, L. V. *J. Alloys Compd.* **2004**, *368*, 135–143.

31. Chen, S.; Gong, X. G.; Walsh, A.; Wei, S.-H. *Appl. Phys. Lett.* **2010**, *96*, 021902.

32. Mitzi, D. B.; Gunawan, O.; Todorov, T. K.; Wang, K.; Guha, S. *Sol. Energy Mater. Sol. Cells* **2011**, *95*, 1421–1436.

33. Katagiri, H.; Jimbo, K.; Tahara, M. *MRS Proc.* **2009**, *1165*.

34. Chen, S.; Walsh, A.; Gong, X.-G.; Wei, S. *Adv. Mater.* **2013**, *25*, 1522–1539.

35. Scragg, J. J.; Ericson, T.; Kubart, T.; Edo, M.; Platzer-Björkman, C. *Chem. Mater.* **2011**, 4625–4633.

36. Redinger, A.; Berg, D. M.; Dale, P. J.; Siebentritt, S. *J. Am. Chem. Soc.* **2011**, *133*, 3320–3323.

37. Ruckh, M.; Schmid, D.; Kaiser, M.; Schaffler, T.; Walter, T.; Schock, H. W. *Sol. Energy Mater. Sol. Cells* **1996**, *41/42*, 335–343.

38. Nakada, T.; Iga, D.; Ohbo, H.; Kunioka, A. *Jpn. J. Appl. Phys.* **1997**, *73236*, 732–737.

39. Kronik, L.; Cahen, D.; Schock, H. *Adv. Mater.* **1998**, *10*, 31–36.

40. Rockett, A. *Thin Solid Films* **2005**, *480-481*, 2–7.

41. Cho, D.-H.; Lee, K.-S.; Chung, Y.-D.; Kim, J.-H.; Park, S.-J.; Kim, J. *Appl. Phys. Lett.* **2012**, *101*, 023901.

42. Ishizuka, S.; Yamada, A.; Islam, M. M.; Shibata, H.; Fons, P.; Sakurai, T.; Akimoto, K.; Niki, S. *J. Appl. Phys.* **2009**, *106*.

43. HLAING Oo, W. M.; Johnson, J. L.; Bhatia, A.; Lund, E. A.; Nowell, M. M.; Scarpulla, M. A. *J. Electron. Mater.* **2011**, *40*, 2214–2221.

44. Sutter-Fella, C. M.; Stukelberger, J. A.; Hagendorfer, H.; Mattina, F. La; Kranz, L.; Nishiwaki, S.; Uhl, A. R.; Romanyuk, Y. E.; Tiwari, A. N. *Chem. Mater.* **2014**, *26*, 1420–1425.

45. Chernomordik, B. D.; Béland, A. E.; Deng, D. D.; Francis, L. F.; Aydil, E. S. *Chem. Mater.* **2014**, *26*, 3191–3201.

46. Johnson, M.; Baryshev, S. V.; Thimsen, E.; Manno, M.; Zhang, X.; Veryovkin, I. V.; Leighton, C.; Aydil, E. S. *Energy Environ. Sci.* **2014**, *7*, 1931.

47. Nagaoka, A.; Miyake, H.; Taniyama, T.; Kakimoto, K.; Yoshino, K. *Appl. Phys. Lett.* **2013**, *103*, 112107.

48. Tanaka, T.; Sueishi, T.; Saito, K.; Guo, Q.; Nishio, M.; Yu, K. M.; Walukiewicz, W. *J. Appl. Phys.* **2012**, *111*, 053522.

49. Ruan, C.-H.; Huang, C.-C.; Lin, Y.-J.; He, G.-R.; Chang, H.-C.; Chen, Y.-H. *Thin Solid Films* **2014**, *550*, 525–529.

50. Romero, M. J.; Du, H.; Teeter, G.; Yan, Y.; Al-Jassim, M. M. *Phys. Rev. B* **2011**, *84*, 165324.

51. Li, J. V.; Kuciauskas, D.; Young, M. R.; Repins, I. L. *Appl. Phys. Lett.* **2013**, *102*, 163905.

52. Nagaoka, A.; Miyake, H.; Taniyama, T.; Kakimoto, K.; Nose, Y.; Scarpulla, M. A.; Yoshino, K. *Appl. Phys. Lett.* **2014**, *104*, 152101.

53. Gershon, T.; Shin, B.; Bojarczuk, N.; Hopstaken, M.; Mitzi, D. B.; Guha, S. *Adv. Energy Mater.* **2014**, 1400849.

Chapter 2

1. D. B. Mitzi, O. Gunawan, T. K. Todorov, K. Wang and S. Guha, Sol. Energ. Mat. Sol. C. **95**, 1421 (2011).
2. H. Katagiri, N. Sasaguchi, S. Hando, S. Hoshino, J. Ohashi and T. Yokota, Sol. Energ. Mat. Sol. C. **49**, 407 (1997).
3. H. Katagiri, Thin Solid Films **480-481**, 426 (2005).
4. T. Todorov, O. Gunawan, S. J. Chey, T. Goislard de Monsabert, A. Prabhakar and D. B. Mitzi, Thin Solid Films **519**, 7378 (2011).

5. N. Vora, J. Blackburn, I. repins, C. Beall, B. To, J. Pankow, G. Teeter, M. Young and R. Noufi, J. Vac. Sci. Technol. A **30**, 051201 (2012).
6. C. A. Wolden, J. Kurtin, J. B. Baxter, I. Repins, S. E. Shaheen, J. T. Torvik, A. A. Rockett, V. M. Fthenakis and E. S. Aydil, J. Vac. Sci. Technol. A **29**, 030801 (2011).
7. K. Ito and T. Nakazawa, Jpn. J. Appl. Phys. **27**, 2094 (1988).
8. N. Nakayama and K. Ito, Appl. Surf. Sci. **92**, 171 (1996).
9. M. T. Winkler, W. Wang, O. Gunawan, H. Hovel, T. Todorov and D. B. Mitzi, Energ. Environ. Sci. **7**, 1029 (2014).
10. B. Shin, O. Gunawan, Y. Zhu, N. A. Bojarczuk, S. J. Chey and S. Guha, S. Prog. Photovoltaics **21**, 72 (2013).
11. A. Chirilă, P. Reinhard, F. Pianezzi, P. Bloesch, A. R. Uhl, C. Fella, L. Kranz, D. Keller, C. Gretener, H. Hagendorfer, D. Jaeger, R. Erni, S. Nishiwaki, S. Buecheler and A. N. Tiwari, Nat. Mater. **12**, 1107 (2013).
12. Q. Guo, H. W. Hillhouse and R. Agarwal, J. Am. Chem. Soc. **131**, 11672 (2009).
13. Q. Guo, G. M. Ford, W.-C Yang, B. C. Walker, E. A. Stach, H.W. Hillhouse and R. Agrawal, J. Am. Chem. Soc. **132**, 17384 (2010).
14. C. Steinhagen, M. G. Panthani, V. Akhavan, B. Goodfellow, B. Koo and B. A. Korgel, J. Am. Chem. Soc. **131**, 12554 (2009).
15. S. C. Riha, B. A. Parkinson and A. L. Prieto, J. Am. Chem. Soc. **131**, 1254 (2009).
16. A. Khare, A. W. Wills, L. M. Ammerman, D. J. Norris and E. S. Aydil, Chem. Commun. **47**, 11721 (2011).
17. B. D. Chernomordik, A. E. Béland, D. D. Deng, L. F. Francis, and E. S. Aydil, Chem Mater. **26**, 3191 (2014).
18. B. D. Chernomordik, A. E. Béland, N. Trejo, A. Gunawan, D. D. Deng, K. A. Mkhoyan and E. S. Aydil, J. Mater. Chem. A **2,** 10389 (2014).
19. T. K. Todorov, K. B. Reuter and D. B. Mitzi, Adv. Mater. **22**, 157 (2010).

20. T. R. Knutson, P. J. Hanson, E. S. Aydil and R. L. Penn, Chem. Comm. **50**, 5902 (2014).
21. I. Repins, C. Beall, N. Vora, C. DeHart, D. Kuciauskas, P. Dippo, B. To, J. Mann, W.-C Hsu, A. Goodrich and R. Noufi, Sol. Energ. Mat. Sol. C. **101**, 154 (2012).
22. T. Ericson, J. J. Scragg, T. Kubart, T. Törndahl and C. Platzer-Björkman, Thin Solid Films **520**, 7093 (2012).
23. H. Katagiri, N. Ishigaki, T. Ishida and K. Saito, Jpn. J. Appl. Phys. **40**, 500 (2001).
24. A.-J. Cheng, M. Manno, A. Khare, C. Leighton, S. Campbell and E. S. Aydil, J. Vac. Sci. Technol. A **29**, 051203 (2011).
25. H. Katagiri, K. Jimbo, W. S. Maw, K. Oishi, M. Yamazaki, H. Araki and A. Takeuchi, Thin Solid Films **517**, 2455 (2009).
26. P. A. Fernandes, P. M. P. Salomé, A. F. da Cunha, and B.-A. Schubert, Thin Solid Films **519**, 7382 (2011).
27. J. J. Scragg, D. M. Berg and P. J. Dale, J. Electroanal. Chem. **646**, 52 (2010).
28. R. Schurr, A. Hölzing, S. Jost, R. Hock, T. Voss, J. Schulze, A. Kirbs, A. Ennaoui, M. Lux-Steiner, A. Weber, I. Kötschau and H. W. Schock, Thin Solid Films **517**, 2465 (2009).
29. A. Fairbrother, X. Fontané, V. Izquierdo-Roca, M. Espíndola-Rodríguez, S. López-Marino, M. Placidi, L. Calvo-Barrio, A. Pérez-Rodríguez and E. Saucedo, Sol. Energ. Mater. Sol. C. **112**, 97 (2013).
30. J. Han, S.W. Shin, M. G. Gang, J. H. Kim and J. Y. Lee, Nanotechnology **24**, 095706 (2013).
31. A. Weber, R. Mainz and H. W. Schock, J. Appl. Phys. **107**, 013516 (2010).
32. A. Redinger, D. M. Berg, P. J. Dale and S. Siebentritt, J. Am. Chem. Soc. **133**, 3320 (2011).
33. J. J. Scragg, T. Ericson, T. Kubart, M. Edoff and C. Platzer-Björkman, Chem. Mater. **23**, 4625 (2011).

34. C. Platzer-Björkman, J. J. Scragg, H. Flammersberger, T. Kubart and M. Edoff, Sol. Energ. Mater. Sol. C. **98**, 110 (2012).
35. W. M. Oo Hliang J. L. Johnson, A. Bhatia, E. A. Lund, M. M. Nowell and M. A. Scarpulla, J. Electron. Mater. **40**, 2214 (2011).
36. M. Johnson, S. V. Baryshev, E. Thimsen, M. Manno, I. V. Veryovkin, C. Leighton and E. S. Aydil, Energ. Environ. Sci. **7**, 1931 (2014).
37. C. M. Sutter-Fella, J. A. Stueckelberger, H. Hagendorfer, F. La Mattina, L. Kranz, S. Nishiwaki, R. Alexander, Y. E. Romanyuk and A. N. Tiwari, Chem. Mater. **26**, 1420 (2014).
38. P. A. Fernandes, P. M. P. Salomé and A. F. A. da Cunha, A. F. A. Thin Solid Films **517**, 2519 (2009).
39. H. Yoo and J. H. Kim, Thin Solid Films **518**, 6567 (2010).
40. K. Wang, O. Gunawan, T. Todorov, B. Shin, S. J. Chey, N. A. Bojarczuk, D. B. and S. Guha, Appl. Phys. Lett. **97**, 143508 (2010).
41. P. A. Fernandes, P. M. P. Salomé and A. F. A. da Cunha, J. Phys. D Appl. Phys **43**, 215403 (2010).
42. Y. C. Cheng, C. Q. Jin, F. Gao, X. L. Wu, W. Zhong, S. H. Li and P. K. Chu, J. Appl. Phys. **106**, 123505 (2009).
43. C. Wang, K. Tang, Q. Yang Y. Qian, Chem. Phys. Lett. **357**, 371 (2002).
44. C. G. Munce, G. K. Parker, S. A. Holt and G. A. Hope, G. A. Colloid Surface A. **295**, 152 (2007).
45. I. D. Olekseyuk, I. V. Dudchak, L. V. Piskach, J. Alloys Compd. **368**, 135 (2004).
46. A. Khare, B. Himmetoglu, M. Johnson, D. J. Norris, M. Cococcioni and E. S. Aydil, J. Appl. Phys. **111**, 083707 (2012).
47. E. Thimsen, S. V. Baryshev, A. B. F. Martinson, J. W. Elam, I. V. Veryovkin and M. J. Pellin, Chem. Mater. **25**, 3113 (2013).
48. J. Ge, W. Yu, H. Cao, J. Jiang, J. Ma, L. Yang, P. Yang Z. Hu and J. Chu, Phys. Status. Solidi A **209**, 1493 (2012).

49. A. Nagaoka, H. Miyake, T. Taniyama, K. Kakimoto, Y. Nose, M. A. Scarpulla and K. Yoshino, Appl. Phys. Lett. **104**, 152101 (2014).

Chapter 3

1. Norris, D. J.; Aydil E. S. *Science* 2012, *338*, 625-626.
2. Wadia C.; Alivisatos, A. P.; Kammen, D. M. *Environ. Sci. Technol.* 2009, *43*, 2072-2077.
3. Mitzi, D. B.; Gunawan, O.; Todorov, T. K.; Wang, K.; Guha, S. *Sol. Energy Mater. Sol. Cells* 2011, 1–16.
4. Ito, K.; Nakazawa, T. *Jpn. J. Appl. Phys.* 1988.
5. Nakayama, N.; Ito, K. *Appl. Surf. Sci.* 1996, *92*, 171–175.
6. Winkler, M. T.; Wang, W.; Gunawan, O.; Hovel, H. J.; Todorov, T. K.; Mitzi, D. B. *Energy Environ. Sci.* 2014, *7*, 1029.
7. Chirilă, A.; Reinhard, P.; Pianezzi, F.; Bloesch, P.; Uhl, A. R.; Fella, C.; Kranz, L.; Keller, D.; Gretener, C.; Hagendorfer, H.; Jaeger, D.; Erni, R.; Nishiwaki, S.; Buecheler, S.; Tiwari, A. N. *Nat. Mater.* 2013, *12*, 1107–1111.
8. Katagiri, H.; Jimbo, K.; Tahara, M. *MRS Proc.* 2009, *1165*.
9. Olekseyuk, I, Dudchak, I.V., Piskach, L. V. *J. Alloys Compd.* 2004, *368*, 135–143.
10. Weber, A.; Mainz, R.; Schock, H. W. *J. Appl. Phys.* 2010, *107*, 013516.
11. Scragg, J. J.; Ericson, T.; Kubart, T.; Edoff, M.; Platzer-Björkman, C. 2011, 4625–4633.
12. Redinger, A.; Berg, D. M.; Dale, P. J.; Siebentritt, S. *J. Am. Chem. Soc.* 2011, *133*, 3320–3323.
13. Johnson, M.; Baryshev, S. V.; Thimsen, E.; Manno, M.; Zhang, X.; Veryovkin, I. V.; Leighton, C.; Aydil, E. S. *Energy Environ. Sci.* 2014, *7*, 1931-1938.
14. Johnson, M.; Manno, M.; Zhang, X..; Leighton, C.; Aydil, E. S. *submitted.*

15. Mousel, M.; Schwarz, T.; Djemour, R.; Weiss, T. P.; Sendler, J.; Malaquias, J. C.; Redinger, A.; Cojocaru-mirédin, O.; Choi, P.; Siebentritt, S. *Adv. Energy Mat.* 2014, *4*
16. Mousel, M.; Redinger, A.; Djemour, R.; Arasimowicz, M.; Valle, N.; Dale, P.; Siebentritt, S. *Thin Solid Films*. 2013, *535*, 83–87.
17. Fernandes, P. A.; Salome, P. M. P.; da Cunha, A. F. *J. Phys. D.* 2010, *43*, 215403.
18. Cheng, A.-J.; Manno, M.; Khare, A.; Leighton, C.; Campbell, S. A.; Aydil, E. S. *J. Vac. SCi. Technol. A* 2011, *29*, 051203.
19. Berg, D. M.; Djemour, R.; Gutay, L.; Siebentritt, S.; Dale, P. J.;Fotane, X.; Izquierdo-Roca, V.; Perez-Rodriguez, A. *Appl. Phys. Lett.* 2012, *100*, 192103.
20. Thimsen, E.; Baryshev, S.V.; Martinson, A. B. F.; Elam, J. W.; Veryovkin, I. V.; Pellin, M. J. *Chem. Mat.* 2013, *25*, 313-319
21. Schurr, R.; Hölzing, A.; Jost, S.; Hock, R.; Voβ, T.; Schulze, J.; Kirbs, A.; Ennaoui, A.; Lux-Steiner, M.; Weber, A. *Thin Solid Films* 2009, *517*, 2465–2468.
22. Han, J.; Shin, S. W.; Gang, M. G.; Kim, J. H.; Lee, J. Y. *Nanotechnology.* 2013, *24*, 095706.
23. Yin, X.; Tang, C.; Sung, L.; Shen, Z.; Gong, H. *Chem. Mat.*2014, *26*, 2005-2014
24. Vaughan, D.; Craig, J. *Mineral Chemistry of Metal Sulfides*; Cambridge University Press: London, UK, 1978.
25. Yu, S.; Wang, M.; Hon, M. *J. Mater. Res.* **2001**, *16*,76-82 .
26. Kumar, S.; Handwerker, C. A.; Dayananda M. A. *J. Phase Equilib. Diff.* 2011, *32*, 309-319.

Chapter 4

1. T. K. Todorov, J. Tang, S. Bag, O. Gunawan, T. Gokmen, Y. Zhu and D. B. Mitzi, *Advanced Energy Materials*, **2013**, 3, 34–38.

2. H. Katagiri, K. Jimbo, W. S. Maw, K. Oishi, M. Yamazaki, H. Araki and A. Takeuchi, *Thin Solid Films*, **2009**, 517, 2455–2460.
3. I. Repins, C. Beall, N. Vora, C. DeHart, D. Kuciauskas, P. Dippo, B. To, J. Mann, W.-C. Hsu, A. Goodrich and R. Noufi, *Sol. Energ. Mat. Sol. C.*, **2012**, 101, 154–159.
4. M. Ruckh, D. Schmid, M. Kaiser, R. Schaffler, T. Walter and H. W. Schock, *Sol. Energ. Mat. Sol. C.*, **1996**, 41/42, 335–343.
5. T. Nakada, D. Iga, H. Ohbo and A. Kunioka, *Jpn. J. Appl. Phys.*, **1997**, 36, 732-737.
6. L. Kronik, D. Cahen and H. Schock, *Advanced Materials*, **1998**, 10, 31–36.
7. A. Rockett, Thin Solid Films, 2005, 480, 2–7.
8. D.-H. Cho, K.-S. Lee, Y.-D. Chung, J.-H. Kim, S.-J. Park and J. Kim, *Appl. Phys. Lett.*, **2012**, 101, 023901.
9. S. Ishizuka, A. Yamada, M. M. Islam, H. Shibata, P. Fons, T. Sakurai, K. Akimoto and S. Niki, S., *J. Appl. Phys*., **2009**, 106, 034908.
10. T. Prabhakar and N. Jampana, *Sol. Energ. Mat. Sol. C.*, **2011**, 95, 1001–1004.
11. W. M. Oo Hlaing, J. L. Johnson, A. Bhatia, E. A. Lund, M. M. Nowell, M. A. Scarpulla, *J. Electron. Mater.*, **2011**, 40, 2214–2221.
12. J. V. Li, D. Kuciauskas, M. R. Young and I. L. Repins, *Appl. Phys. Lett.*, **2013**, 102, 163905.
13. I.V. Veryovkin, C. E. Tripa, M. J. Pellin, *Physics Procedia*, **2008**, *1*, 379–389.
14. S. V. Baryshev, N. G. Becker, A. V. Zinovev, C. E. Tripa, I. V. Veryovkin, *Rapid Commun. Mass Sp*., **2013**, *27*, 2828-2832
15. I. V. Veryovkin, W. F. Calaway, J. F. Moore, M. J. Pellin, D. S. Burnett, *Nucl. Instrum. Meth. B*, **2004**, *219–220*, 473–479.
16. S. V. Baryshev, A. V. Zinovev, C. E. Tripa, R. A Erck, I. V. Veryovkin, *Appl. Surf. Sci.*, **2012**, *258*, 6963–6968.
17. C. A. Andersen, J. R. Hinthorne, *Anal. Chem.*, **1973,** *45* (8), 1421–1438.
18. F. Rüdenauer, W. Steiger, H. Werner, *Surf. Sci.*, **1976,** *54*, 553–560.

19. A.-J. Cheng, M. Manno, A. Khare, C. Leighton, S. Campbell and E. S. Aydil, *J. Vac. Sci. Technol. A*, **2011**, 29, 051203.
20. P. A. Fernandes, P. M. P. Salome and A. F. da Cunha, *Thin Solid Films*, **2009**, 517, 2519-2523.
21. F. Jiang, H. Shen, W. Wang and L. Zhang, *Appl. Phys. Express*, **2011**, 4, 074101.
22. P. Kumar and R. Nagarajan, *Inorg. Chem.*, **2011**, 50, 9204–9206.
23. O. El Jaroudi, E. Picquenard, N. Gobeltz, A. Demortier and J. Corset, *Inorg. Chem.*, **1999**, 38, 2917–2923.
24. C. A. Andersen and J. R. Hinthorne, *Analytical Chemistry*, **1973**, 45, 1421–1438.
25. F. Rüdenauer, W. Steiger and H. Werner, *Surface Science*, **1976**, 54, 553–560.
26. A. Rockett, J. S. Britt, T. Gillespie, C. Marshall, M. M. Al Jassim, F. Hasoon, R. Matson and B. Basol, *Thin Solid Films*, **2000**, 372, 212–217.
27. Braunger, D. Hariskos, G. Bilger, U. Rau and H. W. Schock, *Thin Solid Films*, **2000**, 362, 161–166.
28. W. Niles, M. M. Al-Jassim and K. Ramanathan, *J. Vac. Sci. Technol. A*, **1999**, 17, 291–296.

Chapter 5

1. Shin, B.; Gunawan, O.; Zhu, Y.; Bojarczuk, N. A.; Chey, S. J.; Supratik, G. *Prog. Photovoltaics Res. Appl.* **2013**, 72–76.

2. Wang, W.; Winkler, M. T.; Gunawan, O.; Gokmen, T.; Todorov, T. K.; Zhu, Y.; Mitzi, D. B. *Adv. Energy Mater.* **2014**, *4*.

3. Mitzi, D. B.; Gunawan, O.; Todorov, T. K.; Wang, K.; Guha, S. *Sol. Energy Mater. Sol. Cells* **2011**, *95*, 1421–1436.

4. Katagiri, H.; Jimbo, K.; Tahara, M. *MRS Proc.* **2009**, *1165*.

5. Chen, S.; Walsh, A.; Gong, X.-G.; Wei, S. *Adv. Mater.* **2013**, *25*, 1522–1539.

6. Liu, F.; Li, Y.; Zhang, K.; Wang, B.; Yan, C.; Lai, Y.; Zhang, Z.; Li, J.; Liu, Y. *Sol. Energy Mater. Sol. Cells* **2010**, *94*, 2431–2434.

7. Su, Z.; Yan, C.; Sun, K.; Han, Z.; Liu, F.; Liu, J.; Lai, Y.; Li, J.; Liu, Y. *Appl. Surf. Sci.* **2012**, *258*, 7678–7682.

8. González, J. C.; Ribeiro, G. M.; Viana, E. R.; Fernandes, P. a; Salomé, P. M. P.; Gutiérrez, K.; Abelenda, a; Matinaga, F. M.; Leitão, J. P.; da Cunha, a F. *J. Phys. D. Appl. Phys.* **2013**, *46*, 155107.

9. González, J. C. C.; Fernandes, P. a. A.; Ribeiro, G. M. M.; Abelenda, a.; Viana, E. R. R.; Salomé, P. M. P.; da Cunha, a. F. *Sol. Energy Mater. Sol. Cells* **2014**, *123*, 58–64.

10. Nagaoka, A.; Miyake, H.; Taniyama, T.; Kakimoto, K.; Yoshino, K. *Appl. Phys. Lett.* **2013**, *103*, 112107.

11. Seo, D.; Lim, S. *J. Mater. Sci. Mater. Electron.* **2013**, *24*, 3756–3763.

12. Dhakal, T. P.; Peng, C.; Reid Tobias, R.; Dasharathy, R.; Westgate, C. R. *Sol. Energy* **2014**, *100*, 23–30.

13. Tanaka, T.; Nagatomo, T.; Kawasaki, D.; Nishio, M.; Guo, Q.; Wakahara, A.; Yoshida, A.; Ogawa, H. *J. Phys. Chem. Solids* **2005**, *66*, 1978–1981.

14. Shin, S. W.; Pawar, S. M.; Park, C. Y.; Yun, J. H.; Moon, J.-H.; Kim, J. H.; Lee, J. Y. *Sol. Energy Mater. Sol. Cells* **2011**, *95*, 3202–3206.

15. Rajeshmon, V. G.; Kartha, C. S.; Vijayakumar, K. P.; Sanjeeviraja, C.; Abe, T.; Kashiwaba, Y. *Sol. Energy* **2011**, *85*, 249–255.

16. Wu, X.; Liu, W.; Cheng, S.; Lai, Y.; Jia, H. *J. Semicond.* **2012**, *33*, 022002.

17. Shi, C.; Shi, G.; Chen, Z.; Yang, P.; Yao, M. *Mater. Lett.* **2012**, *73*, 89–91.

18. Amal, M. I.; Kim, K. H. *J. Mater. Sci. Mater. Electron.* **2012**, *24*, 559–566.

19. Zhou, S.; Tan, R.; Jiang, X.; Shen, X.; Xu, W.; Song, W. *J. Mater. Sci. Mater. Electron.* **2013**, *24*, 4958–4963.

20. Ruan, C.-H.; Huang, C.-C.; Lin, Y.-J.; He, G.-R.; Chang, H.-C.; Chen, Y.-H. *Thin Solid Films* **2014**, *550*, 525–529.

21. Johnson, M.; Baryshev, S. V.; Thimsen, E.; Manno, M.; Zhang, X.; Veryovkin, I. V.; Leighton, C.; Aydil, E. S. *Energy Environ. Sci.* **2014**, *7*, 1931.

22. Sutter-Fella, C. M.; Stukelberger, J. A.; Hagendorfer, H.; Mattina, F. La; Kranz, L.; Nishiwaki, S.; Uhl, A. R.; Romanyuk, Y. E.; Tiwari, A. N. *Chem. Mater.* **2014**, *26*, 1420–1425.

23. HLAING Oo, W. M.; Johnson, J. L.; Bhatia, A.; Lund, E. A.; Nowell, M. M.; Scarpulla, M. A. *J. Electron. Mater.* **2011**, *40*, 2214–2221.

24. Kronik, L.; Cahen, D.; Schock, H. *Adv. Mater.* **1998**, *10*, 31–36.

25. Rockett, A. *Thin Solid Films* **2005**, *480-481*, 2–7.

26. Wei, S.-H.; Zhang, S. B.; Zunger, A. *J. Appl. Phys.* **1999**, *85*, 7214.

27. Li, J. V.; Kuciauskas, D.; Young, M. R.; Repins, I. L. *Appl. Phys. Lett.* **2013**, *102*, 163905.

28. Gershon, T.; Shin, B.; Bojarczuk, N.; Hopstaken, M.; Mitzi, D. B.; Guha, S. *Adv. Energy Mater.* **2014**, 1400849.

29. Nagaoka, A.; Miyake, H.; Taniyama, T.; Kakimoto, K.; Nose, Y.; Scarpulla, M. A.; Yoshino, K. *Appl. Phys. Lett.* **2014**, *104*, 152101.

30. Contreras, M. A.; Egaas, B.; Dippo, P.; Webb, J.; Granata, J.; Ramanathan, K.; Asher, S.; Swartzlander, A.; Noufi, R. … *Rec.* … **1997**.

31. Chernomordik, B. D.; Béland, A. E.; Deng, D. D.; Francis, L. F.; Aydil, E. S. *Chem. Mater.* **2014**, *26*, 3191–3201.

32. Persson, C. *J. Appl. Phys.* **2010**, *107*, 053710.

33. Prabhakar, T.; Jampana, N. *Sol. Energy Mater. Sol. Cells* **2011**, *95*, 1001–1004.

34. Mott, N. *Metal-Insulator Transitions*; 2nd ed.; Taylor & Francis, 1990.

35. Shklovskii, B. I.; Efros, A. L. Springer Verlag, 1984.

36. Castner, T. G. In *Hopping Transport in Solids*; Pollack, M.; Shklovskii, B. I., Eds.; Elsevier: North-Holland, 1990.

37. Ogawa, Y.; Jäger-Waldau, A.; Hua, T. H.; Hashimoto, Y.; Ito, K. *Appl. Surf. Sci.* **1996**, *92*, 232–236.

38. Tanaka, T.; Sueishi, T.; Saito, K.; Guo, Q.; Nishio, M.; Yu, K. M.; Walukiewicz, W. *J. Appl. Phys.* **2012**, *111*, 053522.

39. Mousel, M.; Schwarz, T.; Djemour, R.; Weiss, T. P.; Sendler, J.; Malaquias, J. C.; Redinger, A.; Cojocaru-Mirédin, O.; Choi, P.-P.; Siebentritt, S. *Adv. Energy Mater.* **2014**, *4*

40. Walter, T.; Content, A.; Velthaus, K. O.; Schock, H.-W. *Sol. Energy Mater. Sol. Cells* **1992**, *26*, 357–368.